Numerical Modeling of Tidal Turbines: Methodology Development and Potential Physical Environmental Effects

Amir Teymour Javaherchi Mozafari

A thesis submitted in partial fulfillment
of the requirements for the degree of

Master of Science in Mechanical Engineering

University of Washington

2010

Program Authorized to Offer Degree: Mechanical Engineering

University of Washington
Graduate School

This is to certify that I have examined this copy of a master's thesis by

Amir Teymour Javaherchi Mozafari

and have found that it is complete and satisfactory in all respects,
and that any and all revisions required by the final
examining committee have been made.

Committee Members:

_____
Alberto Aliseda

_____
Phil Malte

_____
Brian Polagye

_____
Jim Riley

Date: _____

In presenting this thesis in partial fulfillment of the requirements for a master's degree at the University of Washington, I agree that the Library shall make its copies freely available for inspection. I further agree that extensive copying of this thesis is allowable only for scholarly purposes, consistent with "fair use" as prescribed in the U.S. Copyright Law. Any other reproduction for any purpose or by any means shall not be allowed without my written permission.

Signature_____

Date_____

University of Washington

Abstract

Numerical Modeling of Tidal Turbines: Methodology Development and Potential Physical Environmental Effects

Amir Teymour Javaherchi Mozafari

:

Tidal energy and power extraction using Marine Hydrokinetic (MHK) turbines has recently attracted scientists and engineers attention as a highly predictable source of renewable energy. Currently this technology is at its early stage of research and development. Therefore many studies and investigations need to be done a prior to large scale deployment of MHK devices into proposed tidal sites.

In this thesis, first a general numerical methodology consisting of 3 numerical models, Single Reference Frame (SRF) model, Virtual Blade Model (VBM) and Actuator Disk Model (ADM), will be introduced. These three models have different levels of fidelity and adequacy in capturing and simulating fluid mechanics of a flow going through a horizontal axis MHK turbine. In the next step, these numerical models will be validated by simulating flow flieds around a well characterized two bladed wind turbine and comparing the obtained numerical results from them against the publicly available experimental data for that specific turbine. After the validation process of our numerical methodology, it will be applied to study a MHK turbine with realistic boundary conditions by paying particular attention to the important constraints of MHK turbines such as tip vortex cavitation. Having a successful application of this methodology to study a MHK turbine gives the opportunity of using the converged solution of the simulated flow field around the MHK turbine to address and investigate the potential environmental impacts of the MHK turbines. The influence of the

turbulent wake behind the turbine on enhancement and reduction of sedimentation of suspended particles in the tidal channel and also the effect of the sudden pressure fluctuation across the device on marine species are two samples of the potential environmental impacts of MHK turbines.

Due to restrictions on publicly available data and specifications of MHK turbines we are not modeling an actual MHK turbine design, it should be noted out that the presented results in this thesis can not be applied for making any solid conclusions either about technical issues or environmental friendliness of a MHK turbine. However, the methodology and the study procedure presented here is general and not a function of specific geometry or design. Therefore, it can be applied to any horizontal axis MHK turbine to evaluate both technical as well as environmental issues of that device before its deployment.

TABLE OF CONTENTS

LIST OF FIGURES

Figure Number Page

LIST OF TABLES

ACKNOWLEDGMENTS

I am heartily thankful to my adviser, professor Alberto Aliseda, whose encouragement, supervision and support from the preliminary to the concluding level helped me in developing and understanding of this subject. I would also like to thank National Northwest Marine Renewable Energy Center (NNMREC) and its faculty members at University of Washington for supporting this thesis both financially and scientifically. Last but not the least, I want to thank my parents, brother, family and friends for their never ending moral support.

Dedication:

To my mother who is my soul

To my father who is my body

To my grandfathers, who are watching me all the times from heaven.

Chapter 1

INTRODUCTION

1.1 Background

"Renewable Energy" is a term that automatically directs a scientist's or engineer's mind towards natural resources, such as sunlight, wind, tides, wave and geothermal heat. The main idea behind renewable energy is to take advantage of these available energy resources in nature and convert them to the desired form of energy such as electricity. The generation of electricity from renewable energy resources while minimizing any possible environmental effects is a positive alternative to mitigate the currently extraordinary use of fossil fuels. The dependency of current economic progress on fossil fuels represents a major challenge for our society, particularly in the context of fast consumption increases associated with the explosive growth of developing countries and diminishing rates of existing reserves. From a purely economic, purely environmental, purely strategic point of view, or any combination of them, decreasing the use of fossil fuels in stationary electricity generation is a winning proposition and represents one of the major engineering challenges for the 21^{st} century.

In recent decades, the United States of America (USA) and the European Union (EU) have set specific goals for producing energy from renewable sources, increasing energy efficiency and reducing greenhouse gas (GHG) emissions. For example, in January 2007 the European Commission put forward an integrated energy/climate change proposal that addressed the issues of energy supply, climate change and industrial development. Two months later, European Heads of State endorsed the plan and

agreed to an Energy Policy for Europe [2]. One of the targets of this plan was to have a 20% share of renewables in overall EU energy consumption by 2020. Similarly, the US Department of Defense has committed to using renewable energy sources for 25% of their energy needs by 2025. In the state of Washington, initiative 937 (I-937), passed by popular referendum in 2006, requires utilities to generate 15% of all electricity consumed in the state from renewable energy resources such as solar, wind, tidal and upgraded existing conventional hydropowerplants, but excluding new hydroelectric facilities in the state of Washington, by 2020 [3].

Parallel to political initiatives and protocols, researchers, scientists and engineers are either working on maximizing the efficiency of existing technologies for converting renewable energy resources to electricity and other required forms of energy or they are performing research on alternative forms of renewable energy sources to supply the ever-increasing demand for electricity and other forms of energy such as thermal or mechanical energy.

The available technologies for harvesting different renewable energy resources have various historical backgrounds. Some of these resources have been producing electricity for decades. For example, solar energy is being harvested by solar-thermal or photovoltaic panels to generate thermal and electrical energy respectively. They are being used widely now in European countries such as Spain, Germany and some states such as California in US. Harvesting the kinetic energy of wind via wind turbines is another example of a well-known and developed renewable energy technology, which generates electrical energy from the available kinetic energy of wind in countries such as Denmark, Germany and some states in the US in large commercial scales. On the other side of the spectrum, some of these renewable energy resources are fairly new and still in the phase of research and development. Therefore, they are not yet available for widespread deployment and commercial use. One example of these resources

is Tidal Energy. Recently, however, the increasing demand for electricity in regions with tidal resources like Puget Sound in the state of Washington has led to significant interest in capturing energy from tidal currents. The idea is to extract the potential energy of tides when it becomes available in the form of kinetic energy in high speed tidal current in channels and estuaries. Tidal turbines operate in a very similar way to wind turbines in high wind areas. The specifics of this renewable resource, the proposed technologies to harvest it, and the issues associated with them, are discussed in the following section of this chapter.

1.2 Tidal Energy, a new renewable energy resource.

Tides are formed due to the gravitational forces between the sun, moon and earth. Based on Newton's law of gravitation, two different masses, m_1 and m_2, with a distance r between them, attract each other with a force pointing along the line intersecting the masses. This force is directly proportional to two masses and inversely proportional to the square of the distance between them:

$$F_{12} = F_{21} = G\frac{m_1 m_2}{r^2} \tag{1.1}$$

where F_{12} and F_{21} are the attraction forces and G is the universal gravitational constant, equal to $6.6743 \times 10^{-11}[N(\frac{m}{kg})^2]$. Therefore, the exerted attraction force by the sun and moon on the earth changes the height of the sea and ocean water level as the orientation and location of the earth and moon changes with respect to the sun [4]. Since the distance between earth and moon is smaller than the distance between sun and earth, the moon is responsible, on average, for about 70% of the tide strength, while sun causes about 30% of the effect on tides.

The strongest and weakest tides are called *spring* and *neap* tides, respectively. As shown in figure 1.1, spring tides form when the sun and moon are in line with earth and gravitational forces are in a direction that are added together to form the strongest

tide. Neap tides form when the sun and moon are in opposite positions with respect to earth, as shown in figure 1.1. As a result of this orientation, the gravitational forces work against each other and form neap tides.

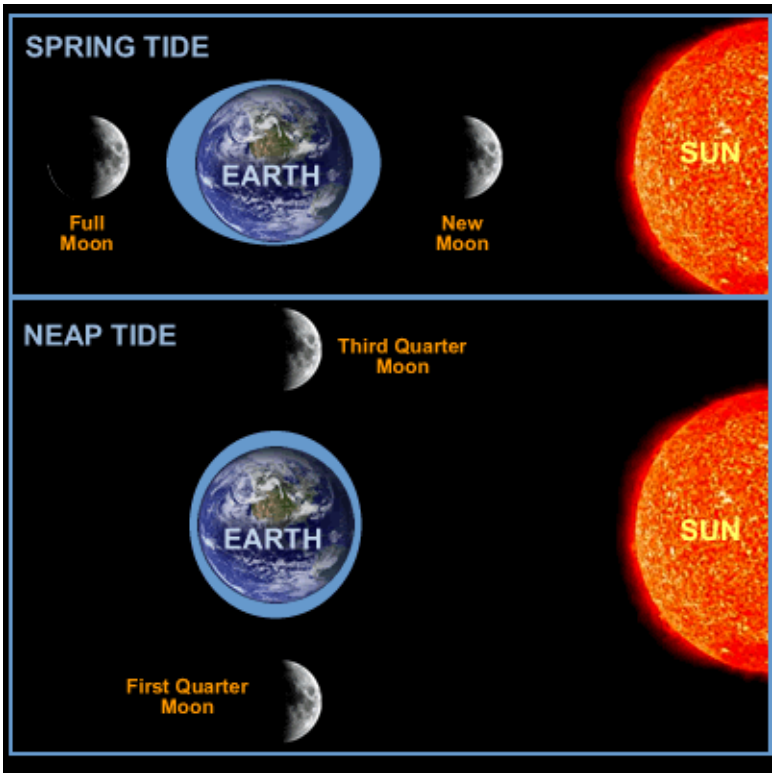

Figure 1.1: Schematic of Spring and Neap tides formation based on the sun, moon and earth orientation. (from windows2universe website)

The tides generated from the gravitational forces between the sun, moon and earth will result in strong tidal currents in regions where the water elevation drives high flows through narrow passages carrying a significant amount of kinetic energy. The specific flux of kinetic energy in these tidally current flows is defined as follows:

$$P = \frac{1}{2}\rho A V^3 \tag{1.2}$$

where ρ is the density of the fluid (i.e. sea water), A is the cross sectional area that the current goes through and V is the velocity of the flowing fluid (i.e. tidal current). An interesting point is that, although the average velocity of tides (2 to 3 $[\frac{m}{s}]$) is smaller than the average wind velocity (12 $[\frac{m}{s}]$), water is 850 times denser than air and therefore tidal currents have significant energy conversion potential even for relatively slow velocities. As long as extracting the available power from wind via wind turbines was a successful process, harvesting the tidal energy seems to be promising as well. The idea of harvesting the available energy of tidal current via tidal turbines is very similar to harvesting the kinetic energy of wind. Although energy generation from tidal currents has many similarities to wind, the balance between kinetic and potential energy is a key element in tidal channels that invalidates "Betz's" limit at high blockage ratios. Cavitation is another concern regarding harvesting the tidal energy that differentiates the design of Marine Hydrokinetic (MHK) turbines from wind turbines. These similarities and differences of tidal and wind energy made this area of research interesting and has attracted significant attention to develop and commercialize tidal energy from both industrial and economical point of view as well as meeting the long term goals of generating energy from renewable energy sources.

Since tidal energy technology is on its early stages of research and development, different shapes and types of turbines are being offered from different companies. There are many different proposed designs such as the ring configuration from Open Hydro or the cross flow horizontal axis configuration from Ocean Renewable Power Company (ORPC) turbine (figure 1.2). In this thesis, however, we have chosen to study a traditional horizontal axis turbine with axial flow, similar to the predominant design in the wind energy industry. There are multiple proposed designs that follow

this configuration, such as Verdant Power's designs.

In the early stages of development in the wind industry, similarly different shapes and designs were proposed for wind turbines and, after a long process of optimization and redesigns, the horizontal axis, three-bladed turbine has emerged as the leading commercial-scale offering for electricity generation from wind. It is possible that the MHK industry will follow a similar process. But it is not our intention to choose winners or predict the future. Simply, we have studied the Horizontal Axis Tidal Turbine (HATT) concept to build on the wealth of methods and existing information on the aerodynamics of this design from thirty years of wind turbine development. We intend to apply our methodology to other flow configurations in an effort to optimize the performance, minimize their potential environmental effects and compare them on a fair and balanced basis. One of the benefits of starting this research with HATTs is that previous studies on Horizontal Axis Wind Turbines (HAWTs) can be used for validation and comparison purposes. In this way, the accuracy of the simulation methods can be evaluated with experimental results that are not available for MHK turbines in the open literature. Once the methodology has been certified under these conditions, it can be applied to the study of MHK where the conditions are not widely different (slightly higher Reynolds number and typically lower Tip Speed Ratios). The influence of the free surface is a new effect that can be implemented, but needs to be validated specifically for MHK turbines since there is no parallel in wind energy.

In this thesis, a general methodology for the modeling and study of horizontal axis turbines is introduced first. Then, the methodology will be validated with the help of experimental and numerical studies on a well-characterized two bladed wind turbine: NREL Phase VI. The validated methodology will be applied toward studying the fluid mechanics and potential environmental effects of a horizontal axis MHK turbine.

(a) Verdant tidal turbine

(b) ORPC tidal turbine

(c) Openhydro tidal turbine

Figure 1.2: Different tidal turbine designs. (From companies website)

1.2.1 Literature Review, Research Overview and Motivations

Previous studies on energy extraction from tidal resources show that scientists, engineers and device developers are interested in building methodologies for characterization of available tidal resources as well as devices. In one of their publications, Couch et al. [5] pointed out two main procedures for understanding and developing the energy extraction technology from tidal energy sources. The first procedure was specifying a methodology for characterization of the resource available at the proposed tidal sites and the second one was developing a methodology for device performance characterization. They also mentioned the potential environmental effects of this power extraction in single or commercial scales is a knowledge gap that should be filled, while the two above-mentioned procedures are being followed by scientist and researchers. Couch and Bryden [6] addressed and investigate the large scale physical response of tidal system to energy extraction and its effects on environment in order to provide a first look at the potential response of the system in 2007.

On the area of device performance characterization, Bahaj and Batten team performed research and different type of studies on development and validation of a numerical methodology for characterization of horizontal axis tidal marine hydrokinetic (MHK) turbines. First Bahaj et al. built and ran a set of experiments on an 800 [mm] diameter device that is a model of a possible 16 [m] diameter MHK turbine in a 2.4 [m] by 1.2 [m] cavitation tunnel and 60 [m] towing tank [7]. In this study they produced a consistent set of experimental data, which provided them useful design information in their own right and suitable for validation process of theoretical and numerical methods in future. Later, Batten et al. [8] used the above-mentioned developed experimental data to validate a numerical scheme for modeling MHK turbines. This numerical model was based on blade-element momentum (BEM) theory and a model for wind turbine design developed by Barnsley and Wellicome [9]. However,

the code developed has major enhancements specifically established to deal with the operation in water. This model integrates the effect of rotating blades, by having the geometrical (i.e. pitch angle and chord length) and physical variables (i.e lift and drag coefficients) for the predefined elements along the span of the blades as inputs. In this study the geometrical specifications were known from the blade design step for the experimental setup. However, the physical variables were calculated with the 2D panel code XFoil, which is a linear vorticity stream function panel method [10]. Batten et al. [11] validated the numerical results such as calculated power and thrust coefficients, against the experimental results from previous studies and observed very good agreements between two sets of results and mentioned that this validated numerical method can now be used as a tool for designing and optimizing energy output with tidal data.

The core idea of this thesis is to develop a numerical methodology that can be validated with experimental results from the wind energy industry and, when they become available, with experiments from Marine Hydrokinetic turbines. As its will be explained shortly in detail, we developed a numerical methodology and validated the most accurate and complicated model in our proposed methodology by modeling a well characterized wind turbine and comparing the numerical results against the publicly available experimental data on modeled device. Then, we compared the numerical results from a less complicated and computationally intensive numerical model, which was also based on BEM theory with the previously validated results and observed a very good agreement between them. Finally, we applied the methodology to study the flow field around and in the wake of a MHK turbine by matching the Reynolds number and tip speed ratio (TSR) for this turbine design. However, the concentration and long term goals of this thesis is looking at the flow field around the blades and also physics of the turbulent wake downstream of the MHK turbine and its potential

environmental effect on the ecosystem. These type of studies and investigations are not been covered by other research groups. The main goal of their previous studies was more on technical characterization of the tidal turbines and matching the turbine design on the tidal flow for understanding the relations between geometry criteria with the amount of extracted power from the flow.

As a conclusion of the literature review, we find out that similar to previously developed renewable energy technologies, such as solar and wind, extensive research, theoretical, experimental, and numerical modeling needs to be done in the area of tidal energy. Furthermore, all the issues and concerns regarding this technology from both technical and environmental point of view should be addressed and investigated. The goal is maximizing the efficiency and minimizing potential environmental effects of this technology a priori, before large scale device deployment and commercialization.

In chapter 2 of this thesis, a numerical methodology for the study of horizontal axis tidal turbines, consisting of three different numerical models with different computational cost and fidelity to the underlying physics, is introduced. Single Reference Frame (SRF) model is the most complex one that simulates the fluid mechanics of the flow around the actual geometry of the blade with the idea of rendering an unsteady problem in the stationary reference frame to a steady one in the rotating reference frame [12][13][14]. The Virtual Blade Model (VBM) is the second tool from computational cost and fidelity point of view in this methodology. VBM models the time-averaged effects of the rotating blades, without the need for creating and meshing the actual geometry of blades using fundamentals of Blade Element Method (BEM) [15][16]. This model simulates the blade effects using a momentum source term placed inside a rotor disk fluid zone that depends on the chord length, angle of attack, and lift and drag coefficients for different sections along the turbine blade

[17][18]. The least complex numerical model in this methodology is the Actuator Disk Model (ADM). In this model, the effect of rotating blades is represented by a pressure discontinuity over an infinitely thin disk with an area equal to the swept area of the rotor. In this work, the implementation of ADM in ANSYS FLUENT by combining the actuator disk theory and procedure of modeling porous media is introduced [19][20].

After the methodology development, in order to be applied to modeling a Marine Hydrokinetic (MHK) turbine, we verified our numerical results with an available experimental data. Therefore, as it will be explained in chapter 3, the NREL Phase VI, a well characterized two bladed wind turbine was simulated using the above mentioned numerical models. The results from this effort were validated against data from experiments done on this turbine in the NASA-Ames wind tunnel by NREL [21]. The detailed report published by NREL with the experimental results of this wind turbine was a revolution in the world of numerical modeling of horizontal axis wind turbine. After it became available, many researchers and scientist modeled this turbine with different numerical models and validated their models against these results [22] [23].

As the next step, when the developed numerical methodology had been validated against a set of experimental and several other high fidelity numerical studies, it was applied to the study of Marine Hydrokinetic (MHK) turbines. As it is discussed in chapter 4, the transition between wind and MHK turbines was done step by step by modifying the working fluid, regenerating the mesh and using new boundary conditions on the previous computational domain. The change of the working fluid from air to water implied an increase in the Reynolds number that required the modification of the mesh of the computational domain [24] to maintain the spatial resolution necessary to model the boundary layer on the turbine blades. The time step was

adapted to the new mesh resolution accordingly. Similarly, new boundary conditions needed to be set based on previous MHK studies and field measurements [1][25][26]. The transition between modeling a wind turbine to modeling a MHK turbine was successful. Having a converged simulation of the flow around a MHK turbine leads us to study the potential environmental effect of MHK turbines, which is the focus of chapter 5. One example of these potential environmental effects is the interaction of the turbulent wake of the device with suspended sediment in the flow. The possible effect of the momentum deficit in the turbine wake on the sedimentation process on the bottom of the tidal channel was studied based on the flow field obtained from the simulation. Another environmental process studied is the presence of sudden pressure fluctuation across the turbine blades with potential effects on marine species like juvenile fish.

Suspended particles slightly denser than water were modeled and studied based on fundamentals of particle laden turbulent flows [27]. Juvenile fish were modeled as slightly buoyant particles and the pressure history along their trajectory studied statistically with particular attention to the high magnitude of the pressure fluctuation occurring over short periods of time. These high impulse conditions were correlated with damage thresholds obtained from laboratory experiments in the literature [28][29].

Chapter 2

NUMERICAL METHODOLOGY DEVELOPMENT

In this chapter the details of three different numerical models used to simulate the dynamics of flow around horizontal axis tidal turbines (HATT): Single Rotating Reference Frame (SRF), Virtual Blade Model (VBM), and Actuator Disk Model (ADM), will be explained. The details on the background and theory for each one of the models are given in the first three sections of this chapter. In the last section, the strengths and weaknesses of each model and their adequacy to study specific problems related to flow around and in the wake of the turbines will also be addressed.

2.1 Single Reference Frame (SRF)

2.1.1 Background

Fluid flow equations are usually solved in a stationary reference frame. There are, however many problems where these equations can be solved in a moving reference frame. One example of a problem that can be simplified by studying it in a rotating reference frame is flow around the blades of a turbine. This type of problems are unsteady in the stationary reference frame and therefore computationally expensive to solve numerically. The main idea behind the Rotating Reference Frame model is to render this unsteady problem in a stationary frame, steady with respect to the moving reference frame. To achieve this, the reference frame rotates with the angular velocity of the turbine. This change of reference frames requires the addition of two extra acceleration terms, Coriolis and Centripetal acceleration, in the momentum

equation and also the definition of a relation between absolute and relative velocity of fluid elements that is used in the governing equations.

2.1.2 Theory

To start the explanation for the theory of this model, consider the rotating reference frame, xyz, rotating with a constant angular velocity $\vec{\omega}$ relative to the stationary reference frame, XYZ, as shown in figure 2.1. The computational domain (CFD domain) is defined with respect to the rotating frame and the location of any arbitrary point in this domain is defined by a position vector $\vec{r}$ from the origin of the rotating frame. Based on this configuration, the fluid element velocity can be transformed from the stationary frame to the rotating frame with the following equation:

$$\vec{v_r} = \vec{v} - \vec{u_r}, \tag{2.1}$$

where $\vec{v_r}$ is velocity relative to the rotating reference frame, $\vec{v}$ is the absolute velocity and $\vec{u_r}$ is the velocity at each point due to the rotation of the reference frame and is defined as follows:

$$\vec{u_r} = \vec{\omega} \times \vec{r}. \tag{2.2}$$

According to the above explanation, equations for conservation of mass, momentum and energy can be written and solved numerically in two different forms, "relative" or "absolute" velocity formulation. In relative velocity formulation, this component of the velocity is the dependent variable and governing equations for this formulation are as follows:

Conservation of mass

$$\frac{\partial \rho}{\partial t} + \nabla \cdot \rho \vec{v_r} = 0, \tag{2.3}$$

Conservation of momentum

$$\frac{\partial}{\partial t}(\rho \vec{v_r}) + \nabla \cdot (\rho \vec{v_r} \vec{v_r}) + \rho(2\vec{\omega} \times \vec{v_r} + \vec{\omega} \times \vec{\omega} \times \vec{r}) = -\nabla p + \nabla \cdot \bar{\bar{\tau}}_r + \vec{F}, \tag{2.4}$$

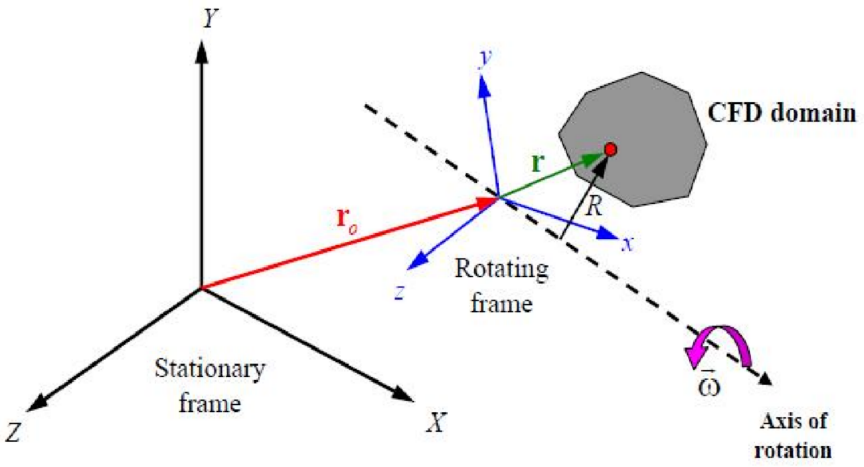

Figure 2.1: Computational domain, stationary and rotating reference frames[14].

Conservation of energy

$$\frac{\partial}{\partial t}(\rho E_r) + \nabla \cdot (\rho \vec{v}_r H_r) = \nabla \cdot (k\nabla T + \overline{\overline{\tau}}_r \cdot \vec{v}_r) + S_h. \tag{2.5}$$

In this formulation, Coriolis acceleration ($2\vec{\omega}\times\vec{v}_r$) and centripetal acceleration ($\vec{\omega}\times\vec{\omega}\times\vec{r}$) are two extra added acceleration terms in the conservation of momentum equation as a result of change in reference frame. Conservation of energy is also written in terms of the relative internal energy (E_r) and the relative total enthalpy (H_r), which are defined as follows:

$$E_r = h - \frac{p}{\rho} + \frac{1}{2}({v_r}^2 - {u_r}^2), \tag{2.6}$$

$$H_r = E_r + \frac{p}{\rho}. \tag{2.7}$$

In the alternative form, the absolute velocity formulation, this velocity component is the dependent variable in the momentum equation, therefore the governing equation is as follows:

Conservation of mass

$$\frac{\partial \rho}{\partial t} + \nabla \cdot \rho \vec{v}_r = 0, \tag{2.8}$$

Conservation of momentum

$$\frac{\partial}{\partial t}\rho\vec{v} + \nabla \cdot (\rho \vec{v}_r \vec{v}) + \rho(\vec{\omega} \times \vec{v}) = -\nabla p + \nabla \cdot \overline{\overline{\tau}} + \vec{F}, \tag{2.9}$$

Conservation of energy

$$\frac{\partial}{\partial t}\rho E + \nabla \cdot (\rho \vec{v}_r H + p\vec{u}_r) = \nabla \cdot (k\nabla T + \overline{\overline{\tau}} \cdot \vec{v}) + S_h. \tag{2.10}$$

When the entire domain is studied as one rotating frame, the simulation uses the Single Reference Frame (SRF) model. This is in contrast with simulations where a subdomain near the rotating object (i.e. turbomachinery) is studied using a moving reference frame, but the rest of the domain is divided into several subdomains (inlet, outlet, ...) and studied in the stationary reference frame, referred to as Multiple Reference Frame (MRF) model. In this case, the above conservation equations for either formulation will be solved in all fluid zones and suitable boundary conditions should be prescribed. In particular, the wall boundaries that are moving with respect to the stationary reference frame (i.e. turbine blades surfaces) are described by a no-slip condition so that the relative velocity with respect to the rotating reference frame is zero. Walls that are not moving with respect to the stationary coordinate system (i.e. most outer walls of the domain that surrounds the turbine blade. For example cylindrical wind tunnel walls surrounding a rotating turbine blade) need to be surfaces of revolution about the axis of rotation and should have a slip condition, so that there is no shedding of vorticity from the walls as they move relative to the rotating reference frame. Another type of boundary condition that might be used in SRF are rotationally periodic boundaries, which must be periodic about the axis of rotation. For example, it is common to model flow through turbine blades assuming the flow is

rotationally periodic and using a periodic domain about a single blade. This permits good resolution of the flow around the blade without the expense of modeling the full 360°domain. However, the need for axisymmetric periodic boundary conditions is an important restrictions of SRF model for studying some specific problems, as will be discussed in later sections.

2.2 Virtual Blade Model (VBM)

2.2.1 Background

One of our long term goals is to study the flow field resulting from the interaction of multiple turbines and the interaction of turbine blades with the wake of other devices. This goal and the observation that the turbulent wake becomes axisymmetric at distances of only a few radii downstream of the turbine in Single Reference Frame (SRF) model results, which will be discussed in the next chapter, directed us to search for and develop less computationally intensive numerical models. The new model is expected to decrease the computational cost (computational requirements and run time), but still model the velocity deficit and the turbulent wake downstream of the turbine with acceptable approximation. After some research, Virtual Blade Model (VBM) seems to be a promising candidate. This model is an implementation of the Blade Element Method (BEM) within ANSYS FLUENT, based on a paper by Zori and Rajagopalan [15]. It was originally conceived to model the aerodynamics of rotating blades (originally propellers and helicopter rotors) and fills the gap between the simpler Actuator Disk Model (ADM) and the more realistic Single Reference Frame (SRF) model. VBM models the time-averaged aerodynamic effects of the rotating blades, without the need for creating and meshing the actual geometry of blades. This model simulates the blade aerodynamic effects using a momentum source term placed inside a rotor disk fluid zone that depends on the chord length, angle of

attack, and lift and drag coefficients for different sections along the turbine blade.

2.2.2 Theory

The Virtual Blade Model simulates the effect of the rotating blades on the fluid through a body force in the x, y and z direction, which acts inside a disk of fluid with an area equal to the swept area of the turbine. The value of the body force is time-averaged over a cycle from the forces calculated by the Blade Element Method (BEM). In BEM, the blade is divided into small sections from root to tip. The lift and drag forces on each section are computed from 2D aerodynamics based on the angle of attack, chord length, airfoil type, and lift and drag coefficient of each segment. The free stream velocity at the inlet boundary is used as an initial value to calculate the local angle of attack (AOA), Mach and Reynolds number for each segment along the blade. Then, based on the calculated values of AOA, lift and drag coefficients are interpolated from a look-up table, which contains values of these variables as a function of AOA, Re and Mach. With this information, lift and drag force of each blade segment can be calculated by

$$f_{L,D} = c_{L,D}(\alpha, \mathrm{Ma}, \mathrm{Re}).c(r/R).\frac{\rho.V_{tot}^2}{2}, \tag{2.11}$$

where in this equation $c_{L,D}$ is lift or drag coefficient, $c(r/R)$ is the chord length of the segment, ρ is the fluid density and V_{tot} is the velocity of the fluid relative to the blade. In equation 2.11, $c_{L,D}$ and $c(r/R)$ are two required inputs for the VBM, that are provided by the modeler. $c_{L,D}$ is either obtained by means of experiment or simulating a 2D segment of the airfoil or 3D modeling of the blade span under the same operating conditions using high fidelity numerical models. $c(r/R)$ is the physical variable that depends on shape and design of the blade and will be provided by the manufacturer. The lift and drag forces are averaged over a full turbine revolution to

calculate the source term at each cell in the numerical discretization by

$$F_{L,D_{cell}} = N_b.\frac{dr.d\theta}{2\pi}.f_{L,D}, \tag{2.12}$$

$$\vec{S}_{cell} = -\frac{\vec{F}_{cell}}{V_{cell}}, \tag{2.13}$$

where N_b is the number of blades, r is the radial position of the blade section from the center of the turbine, θ is the azimuthal coordinate and V_{cell} is the volume of the grid cell. The flow is updated with these forces and this process is repeated until a converged solution is attained.

2.3 Actuator Disk Model (ADM)

2.3.1 Background

Actuator Disk Model (ADM) is the FLUENT implementation of Actuator Disk Theory also referred to as Linear Momentum Theory. In this model the aerodynamic effect of rotating blades is represented by a pressure discontinuity over an infinitely thin disk with an area equal to the swept area of the rotor.

In ADM, the thin disk is modeled as a porous media that supports a pressure difference, but not a velocity difference. That is, the pressure in front of the disk is greater than in the back, but the velocity evolves continuously across the disk.

As shown in figure 2.2, the flow going through the disk is represented by a streamtube. In the following subsection 2.3.2, the relation between velocity components at each section of the streamtube (i.e. inlet, location of the turbine and outlet) and the power extracted by the turbine from the flow is derived from control volume analysis of the equations of conservation of mass, momentum and energy. Combination of these equations with a model of flow in a porous media, are used in the implementation of the Actuator Disk Model for simulation of the flow around a horizontal axis turbine. As will be discussed below, it should be noted that the ADM parameterization must

be either informed by higher fidelity models (i.e., SRF or VBM) or an estimate of the device operating condition and efficiency.

2.3.2 Theory

In order to derive the governing equations for physics of the flow through the turbine and also relations between different variables in the flow field, we assume one dimensional, steady state, incompressible flow through the turbine. We consider a control volume consist of a streamtube around the turbine, starting upstream of the device and ending a large distance downstream of the device, where the velocity is supposed to be uniform and unidirectional in the streamwise direction. Figure 2.2 shows a schematic of these assumptions.

Three important locations along the streamlines are considered in the analysis. Section one is the free stream condition upstream of the turbine, section two located at the turbine plane and section three is at the outlet, far downstream of the turbine, where the pressure recovers to ambient value. Based on these assumptions, and performing a control volume analysis, we can derive the governing equation and final relationship*.

For conservation of mass in a fixed, nondeforming control volume, the equation is

$$\frac{\partial}{\partial t}\int_{cv} \rho \, d\forall + \int_{cs} \rho V \cdot \vec{n} \, dA = 0. \tag{2.14}$$

Based on the steady state flow assumption the first term on the left hand side of the equation 2.14 will be equal to zero. Since the boundaries of the control volume is the streamtube and no mass can enter or leave these boundaries, the final form of equation 2.14 will be

$$u_1 A_1 = u_2 A_2 = u_3 A_3, \tag{2.15}$$

*The general form of the governing equations are obtained from "Fundamentals of Fluid Mechanics", 6th edition by Munson

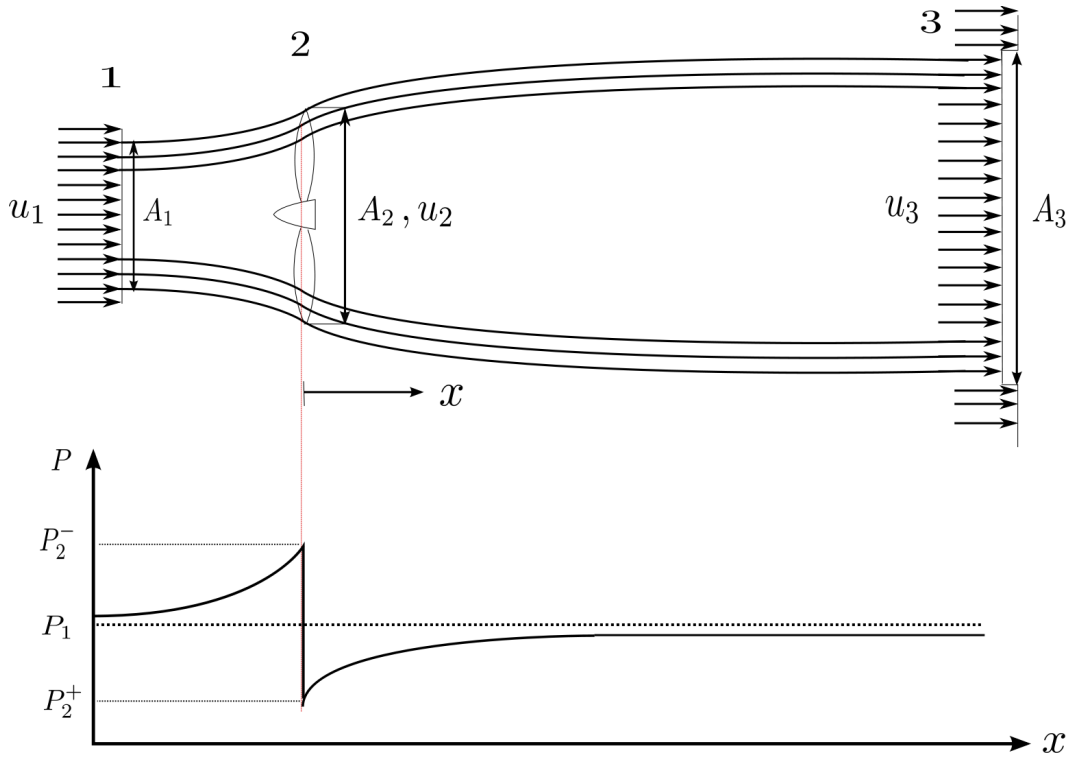

Figure 2.2: Schematic of the flow going over turbine blades modeled as an actuator disk. Note the pressure difference across the disk.

where u and A are the streamwise velocity component and area at each cross section. Similarly, the general form of linear momentum equation for a fixed, inertial and nondeforming control volume will be

$$\frac{\partial}{\partial t}\int_{cv} V\,\rho\,d\forall + \int_{cs} V\,\rho\,V\,\cdot\,\vec{n}\,dA = \Sigma F_{cv}. \tag{2.16}$$

Analogous to the applied assumptions for equation of conservation of mass, steady flow and no flow across the streamtube boundaries, the first term on the left hand side of the equation 2.16 will be equal to zero and the equation 2.16 reduces to

$$\rho {u_3}^2 A_3 - \rho {u_1}^2 A_1 = F_A, \tag{2.17}$$

where F_A is the force that the turbine exerts on the flow.

The general form of conservation of energy is

$$\frac{\partial}{\partial t}\int_{cv} e\,\rho\,d\forall + \int_{cs}(\,\breve{u} + \frac{p}{\rho} + \frac{V^2}{2} + gz\,)\,\rho V\,.\,\vec{n}\,dA = \dot{Q}_{net} + \dot{W}_{net}, \tag{2.18}$$

where e is the total energy per unit mass for each particle in the system and $\breve{u}$ is the internal energy per unit mass. Now neglecting heat transfer on the boundaries and considering control volume from the inlet to a point just before the turbine and from a point just after the turbine to the outlet, so that no work is done within the control volume, the right hand side of equation 2.18 will be equal to zero. Furthermore, having steady state flow, and neglecting changes of internal energy and elevation, equation 2.18 will be simplified to the following form:

$$p_i + \frac{1}{2}\rho {u_i}^2 = constant. \tag{2.19}$$

The above equation is a simplified form of conservation of energy, known as Bernoulli's equation. With the above-mentioned assumptions, this equation can be applied along a streamline between two points. We apply it from the inlet (1) to a point just before the actuator disk (2^-) and between a point just after the actuator disk (2^+) and the outlet (3).

$$p_1 + \frac{1}{2}\rho {u_1}^2 = {p^+}_2 + \frac{1}{2}\rho {u_2}^2 \tag{2.20}$$

$$p_3 + \frac{1}{2}\rho {u_3}^2 = {p^-}_2 + \frac{1}{2}\rho {u_2}^2 \tag{2.21}$$

Subtracting equation 2.20 from 2.21 multiplying both sides by A_2 gives

$$\frac{1}{2}\rho A_2 {u_1}^2[1 - (\frac{u_3}{u_1})^2] = A_2({p^+}_2 - {p^-}_2) = F_A. \tag{2.22}$$

Comparing equation 2.22 with equations 2.17 and 2.15, we will have

$$u_2 = \frac{1}{2}(u_1 + u_3). \tag{2.23}$$

Equation 2.23 shows that fluid velocity at the location of the turbine will be less than the free stream velocity. This is due to the power extraction by the device from the flow because of the pressure difference between the front and the back of the turbine. The ratio of this velocity reduction to the free stream velocity is the new variable called *Axial Induction Factor* defined as

$$a = \frac{u_1 - u_2}{u_1}. \tag{2.24}$$

Using the above equations 2.23 and 2.24, the relation between velocities at different cross sections of control volume as a function of axial induction factor will be as

$$\frac{u_2}{u_1} = 1 - a, \tag{2.25}$$

$$\frac{u_3}{u_1} = 1 - 2a. \tag{2.26}$$

Therefore, the final expression for the power extracted from the turbine and the efficiency of the device will have the form of

$$P = F_A u_2 = \frac{1}{2}\rho {u_1}^3 A_2[4a(1-a)^2], \tag{2.27}$$

$$\eta = 4a(1-a)^2. \tag{2.28}$$

At this stage, the derived governing equations and relations between different velocity components along the streamtube and the efficiency of the turbine in the flow is combined with the implementation of a porous media in ANSYS FLUENT. This is done by equating the modeled pressure difference across the porous media in ANSYS FLUENT and the pressure difference across the device based on the actuator disk theory. This will provide the opportunity to model a horizontal axis turbine with ADM.

Porous media conditions in ANSYS FLUENT models a thin membrane that has a known velocity or characteristic pressure drop associated with it. Usually the porous

media has a thickness over which the pressure change is defined as a combination Darcy's law and an additional inertial loss term.

$$\Delta p = (\frac{\mu}{\alpha} v + C_2 \frac{1}{2} \rho v^2) \Delta m. \tag{2.29}$$

In equation 2.29, μ is the fluid viscosity, α is the face permeability of the media, C_2 is the pressure jump coefficient, v is the velocity normal to the porous face and Δm is the thickness of the media. In this equation α and C_2 are the only unknown coefficients that need to be evaluated to estimate the pressure drop across the porous media. To find the values for these coefficients, a second order polynomial of the pressure as a function of velocity at the plane of the turbine (u_2) should be derived from Actuator Disk Theory. In order to do this, a range of free stream velocity at the inlet (u_1) is considered. A rough estimate of the device efficiency form either higher fidelity numerical models (i.e. SRF or VBM) or from experimental tests of the device is needed to calculate the axial induction factor using equation 2.28. The values of a and u_1 provide us with a range for u_2 and ΔP using equation 2.25 and equations 2.23, and 2.22 respectively. With these two ranges, a second order polynomial is defined and fitted to equation 2.29 to calculate the values for α and C_2.

With the appropriate values of α and C_2, the flow behavior going through the horizontal axis turbine can be modeled as an actuator disk. In section 3.3 of chapter 3 the validation of this model is discussed with results from the NREL Phase VI wind turbine.

2.4 Fidelity and Adequacy of the Numerical Models

According to the discussed theory behind each of the available numerical models in our methodology, SRF is the most realistic model for simulating the flow around and in the near wake of a horizontal axis turbine. Since in SRF the actual geometry of the blade is created and the rotation is modeled via the prescribed periodic boundary conditions, it captures the detail of the flow right before and after the blade. The main concern about SRF model is its high computational cost and also the restrictions that it has regarding the applied boundary conditions for other study purposes. For example, the bottom effect of the channel on the flow field or effect of a shear velocity profile at the inlet on the extracted power by turbine can not be simulated using the SRF model. These limitations are due to the restrictions on modeling the full channel and the need to have an axisymmetric domain for the SRF model. As it will be explained later in chapter 5, the pressure history of small neutrally buoyant particles as they flow through the turbine, representing juvenile fish swimming near the turbine blades, is calculated using the SRF model. The instantaneous pressure-velocity fluctuations in the flow in the proximity of the turbine is accurately simulated by SRF and therefore this model is adequate to simulate physical effects that depend on instantaneous and point-wise values of the flow variables, and not on integrated effects over long spatial or temporal scales.

VBM is a simpler model in comparison with SRF. Although in this model the actual geometry of the blade is not represented, the wake of the turbine can be modeled using the detail specifications of the blade, such as pitch and twist angles, chord length and lift and drag coefficients. This model has lower computational costs in comparison with SRF but, because the effect of the blades on the flow is temporally averaged over the course of an entire rotation cycle, and applied along the entire disk, it is not capable of capturing the instantaneous details of the flow around the blade. The

resulting flow is steady and axisymmetric and can not be used to study phenomena that occurs in the near wake (up to about 3 radii downstream of the turbine). It is ideal, however, to study physical effects that take place over the entire length of the wake, such as sedimentation due to the velocity deficit created by the power extraction at the turbine. Very long channel and multiple turbines in an array can be simulated in relatively short computational times, allowing for parametric studies of these complex problems. Realistic boundary conditions can also be applied, such as a bottom boundary layer or sheared velocity profiles at the inlet, since the restriction to axisymmetric boundary conditions of the SRF model does not apply to VBM.

ADM is the cheapest and fastest model among the ones studied in this methodology. A sink of momentum in the flow is applied as a porous media to model the effect of drag and power extraction of the turbine. It should be noted that for this model, parallel to decreasing the computational costs, the accuracy of the simulated flow field will be decreased too. Therefore, ADM will not be able to model the physics of the flow in the near wake region and the simulated velocity deficit in the far wake region will be different than the one modeled via either SRF or VBM. This is one of the fundamental limitations of the ADM. However, as it will be discussed in chapters 3 and 4 when the boundary conditions are changed from idealized one to more realistic one (i.e. the value of turbulent intensity at the inlet of the channel) ADM shows a better results which are closer to the SRF and VBM results in the far wake region. Acceptable accuracy for the simulated flow at the far wake and minimum computational time requirement make ADM a perfect model for flow field simulation in very large arrays of turbines and study the role of the turbulent wake and momentum deficit created by upstream turbines on the efficiency of the downstream turbines. Beside the minimum computational costs requirement for ADM in compare to SRF and VBM, the simple physics and governing equations behind this model, make it

very easy to be implemented from scratch in any other computational softwares in comparison with the complicated physics and governing equation of VBM.

In the next three chapters, the validation of these three numerical models and their application to modeling a Marine Hydrokinetic (MHK) turbine, the strengths and weaknesses of the three models are described in more detail and the results show the range of applicability and their limitations.

Chapter 3

VALIDATION OF THE DEVELOPED NUMERICAL METHODOLOGY WITH MODELING NREL PHASE VI WIND TURBINE

In Chapter 2 the numerical methodology for modeling a horizontal axis turbine was explained in detail. Three different numerical models, Single Reference Frame (SRF), Virtual Blade Model (VBM) and Actuator Disk Model (ADM) were introduced, their theory, fidelity and adequacy to study specific problems related to the flow around and in the wake of a turbine were addressed.

In this chapter, the validation of this methodology is presented by modeling a well-characterized two bladed, horizontal axis wind turbine, the NREL phase VI turbine. The previously discussed features of these three models are investigated. Then, we explain how the results from these models have been validated by comparison with the NREL experimental results [21] and inter-comparison of the relevant variables between the different numerical models. Each section of this chapter describes the specifics of the computational domain and numerical settings for one of the models. In the end, the results are presented, compared and discussed in detail.

Numerical simulation of the NREL Phase VI wind turbine via the SRF model and validation of this part of our methodology was done by Mr. Sylvain Antheaume. He was a visiting Ph.D. student from INPG in France, who worked on the setup of this problem at NNMREC-UW during 2009. He started the device modeling process by validating 2D simulation results of the airfoil section. After finding the best mesh structure around the blade section and be confident that the fine resolution mesh

is capable of capturing the complex turbulent flow around the blade and therefore model the rest of the flow accurately, he created the full 3D domain and simulated the flow field around and in the wake of the turbine. I then started comparing the results from VBM and ADM model to his results from SRF in order to complete the validation of the methodology. The cited data, information, figures and sketches in this chapter regarding the SRF model are from Mr. Antheaume's unpublished report [30].

3.1 Rotating Reference Frame Model

3.1.1 Computational Domain

The computational domain for the Single Reference Frame (SRF) model was created based on the dimensions and operating conditions of NREL Phase VI experiments at the NASA AMES wind tunnel [21]. This provides the possibility of validation of the final results against NREL results. Since the SRF model requires an axisymmetric domain and boundary conditions and in order to keep the blockage ratio constant, the rectangular cross section of the NASA AMES wind tunnel, where the NREL turbine was tested, was replaced by an equivalent domain with a semi-circular cross section with 16$[m]$ radius. Figure 3.1 shows the full view of the SRF domain.

This computational domain consist of three main blocks. The first block (right hand side of the figure) is the area upstream of the turbine and is 9 radii long. The second one is the middle block that includes the turbine blade and a number of auxiliary blocks to create the structured C-mesh around the blade. The third block (left hand side of the figure) is an area 13.5 radii downstream of the turbine. The boundary conditions at the channel's inlet and outlet are velocity-inlet and pressure-outlet respectively. Cyclic periodic boundaries were prescribed on the bottom of the domain and tunnel walls were modeled with a slip wall (no stress in the tangential directions and no flow-through in the normal direction) boundary condition.

Due to the high density of cells in the middle block, it is hard to see details in figure 3.1, therefore a close up of this section is shown in figure 3.2.

Figure 3.2 shows the blade and auxiliary blocks around it. The blade surface is modeled as a no-slip wall boundary condition and periodic boundaries are prescribed at the bottom of this section. Due to the complexity of the hub geometry and the boundary condition restrictions in the SRF model (section 2.1.2), the blade geometry

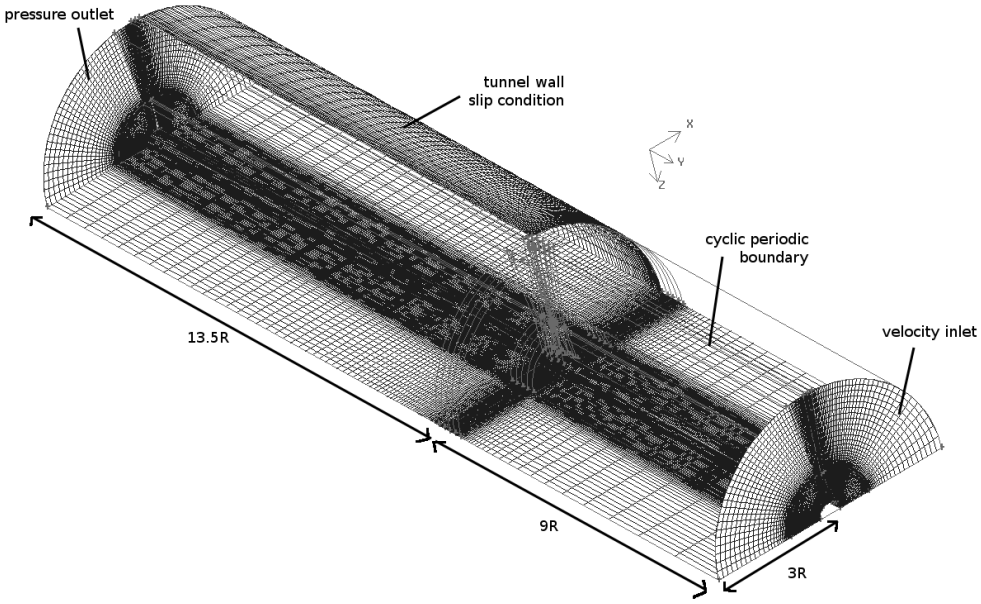

Figure 3.1: SRF computational domain and boundary conditions.[30]

starts at the point where its cross-section takes the shape of the S809 airfoil and the hub of the turbine is modeled as a hollow cylinder starting from the inlet to the outlet of the channel. The C-mesh around the blade section has 110 cells. 48 cells were created on the perpendicular lines to the chord (see figure 3.2) with higher resolution near to the edge of the blade to capture the complex turbulent flow in this region. 73 cells are distributed along the blade span from root to the tip and the mesh is refined at the tip to capture potential vortex shedding. At the tip, an unstructured mesh block was added, with 1200 pave quadrilateral cells over the tip surface and 40 elements along the span, from tip of the blade to the top of the channel. In order to avoid highly skewed elements at the tip of the blade, the trailing edge had to be

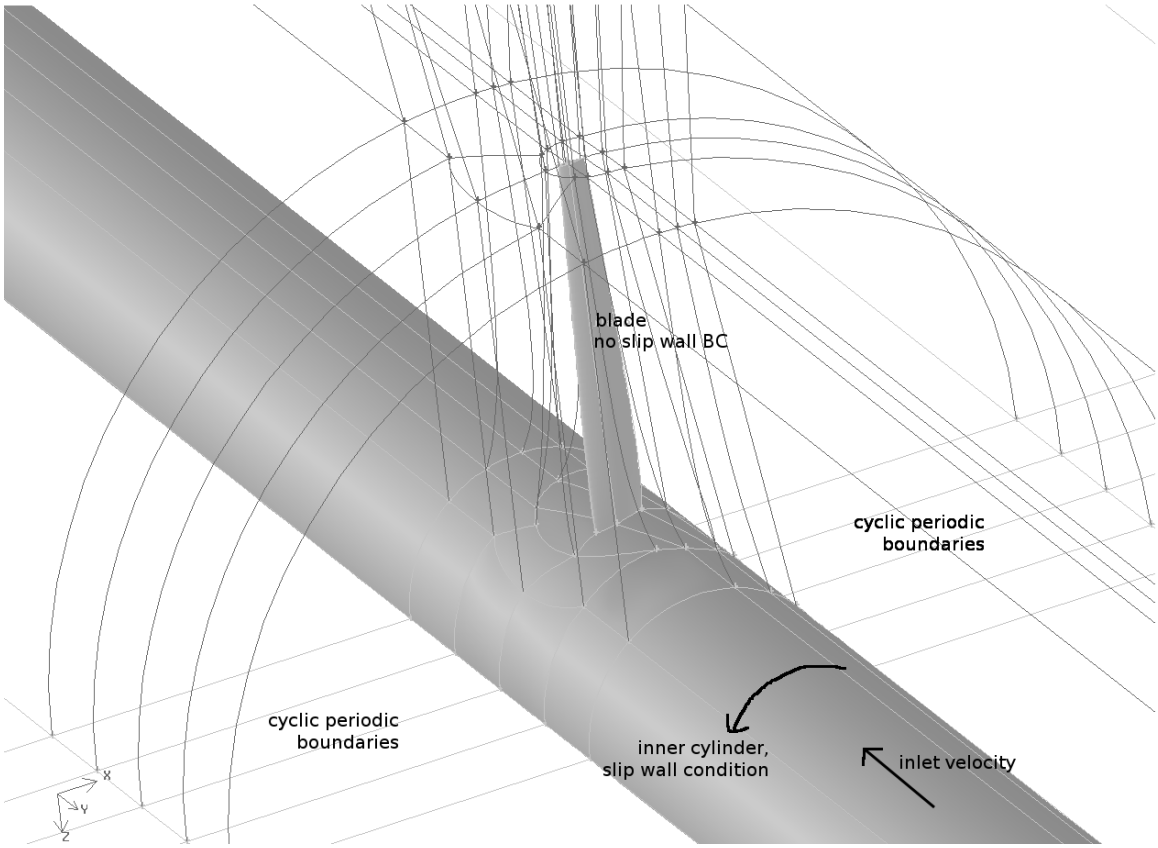

Figure 3.2: Zoomed-in middle block in SRF domain.[30]

modified [30].

3.1.2 Numerical Modeling Settings

The most important settings and solution methods for the validation of the results from the numerical simulations against the experimental data of the NREL Phase VI wind turbine test are presented in table 3.1. In order to have a stable and converged solution at the desired operating conditions with SRF, we had to gradually increase the rotational speed of the turbine. In this way, the rotation of the reference frame

and the motion induced by the boundary conditions will not lead to large complex forces in the flow as the angular velocity increases. On the other side of the spectrum, the dependency of the angle of attack (AOA) on the free stream and blade angular velocities also requires gradual increase of the free stream velocity, since having very large angle of attacks will result in flow separation along the blade and non-physical results.

Table 3.1: SRF model settings and solution methods

Solver Type	Pressure-Based
Velocity Formulation	Absolute
Turbulent Models	Spallart-Allmaras or k-ω
Pressure-Velocity Scheme	SIMPLE
Discretization of Gradient	Green-Gauss Node Based
Discretization of Pressure	Second Order
Discretization of Momentum	QUICK
Discretization of Turbulent Viscosity	Second Order Upwind
Pressure Under-relaxation Factor	0.2
Momentum Under-relaxation Factor	0.6
Modified Turbulent Viscosity Under-relaxation Factor	0.6

3.2 Virtual Blade Model (VBM)

3.2.1 Computational Domain

The VBM computational domain is created based on the dimensions of the SRF domain. This gives the opportunity to have reasonable comparisons between VBM results and the validated results from SRF. Figure 3.3 shows the VBM computational domain.

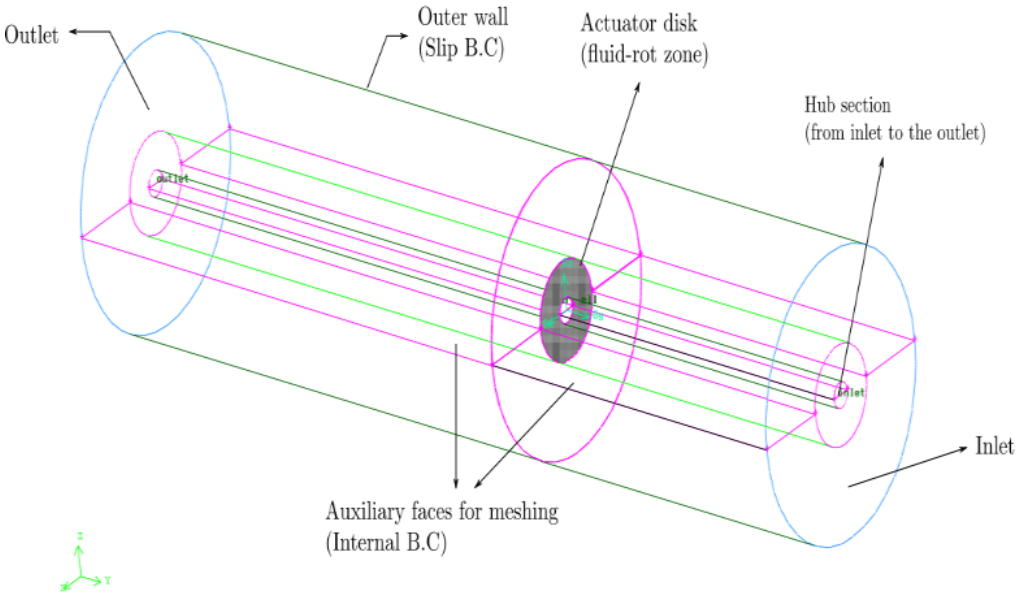

Figure 3.3: VBM domain and its boundary conditions.

The highlighted thin disk in the middle of the channel is the rotor disk mentioned in the VBM theory section (subsection 2.2.2). Momentum sources in x, y and z direction will be placed inside of this disk to model the effect of the rotating blades with the help of additional inputs (i.e. lift and drag coefficients, airfoil radial position, chord length, pitch and twist angle of segments along the blade) without the inclusion of the

actual geometry of the blades. In order to compare the results from this simulation with the SRF data, the turbine hub is not modeled here and is replaced by a hollow cylindrical volume from inlet to outlet of the channel.

Boundary conditions in this domain are similar to those in the SRF. Velocity-inlet and pressure-outlet conditions are considered for the channel inlet and outlet respectively. Slip condition is set for the outer wall and the hub section. It should be noted out that the horizontal planes in the middle of the domain are auxiliary faces used to define the internal VBM disk mesh. Unlike the SRF domain, the boundary conditions are not periodic. The main difference is the condition for the thin disk that models the effect of the rotating blades. The whole disk volume is prescribed as a fluid zone and the faces of this volume should have a full circle shape without any discontinuity on their area (full 360° span) with an interior boundary condition. Setting this boundary condition in the process of generating the mesh for the VBM domain is very important. Lack of having a full circle shape for faces of the disk or the interior condition will lead to an error, when the mesh is imported into ANSYS FLUENT or when the virtual blade model needs to be turned on.

3.2.2 Numerical Modeling Settings

The general settings for VBM are similar to settings for SRF model as stated in table 3.1. The main difference is the need for settings and inputs for the virtual blade model. In this section the most important settings for the VBM used to model the NREL Phase VI wind turbine is briefly described. Readers are referred to VBM sources [17] and the ANSYS FLUENT manual for more details about the definitions and physical description of each of the inputs.

Figure 3.4 shows the panel used for providing the general information of the blades such as blades count, radius, angular velocity and the origin of the rotor disk. Here,

a single NREL Phase VI wind turbine is modeled with the VBM. This device is a 2 bladed wind turbine with radius equal to 5.53 $[m]$. The angular velocity of the rotor during the test was is 72 $[rpm]$. In the VBM, local lift and drag forces are computed assuming 2D flow. However, approaching the tip of the blade, this assumption is violated by an increasingly strong secondary flow around the tip of the blade. The tip effect value is designed to take this phenomena into account. A value of 96% is selected meaning that lift and drag forces forces are calculated for 96% of the blade span, while the 4% nearest the tip produces drag but not lift. In this geometry, the center of the rotor disk is located at the origin of the coordinate axis and thus is set to be equal to (0,0,0).

For NREL Phase VI wind turbine, rotor disk bank angle and blade collective pitch angle are the only two angles that needs to be defined. The blades of this turbine are considered rigid and flapping motion is not analyzed during turbine operation. Rotor disk bank angle is the angle that describes the position of the rotor disk with respect to the incoming flow. Since this device is a horizontal axis turbine, the bank angle is set to 90°. For this turbine values of blade pitch and twist angle at the tip are 3 and 2.5° degrees respectively, therefore based on these values and angle sign convention used in VBM, value of collective pitch angle is set to -5.5°.

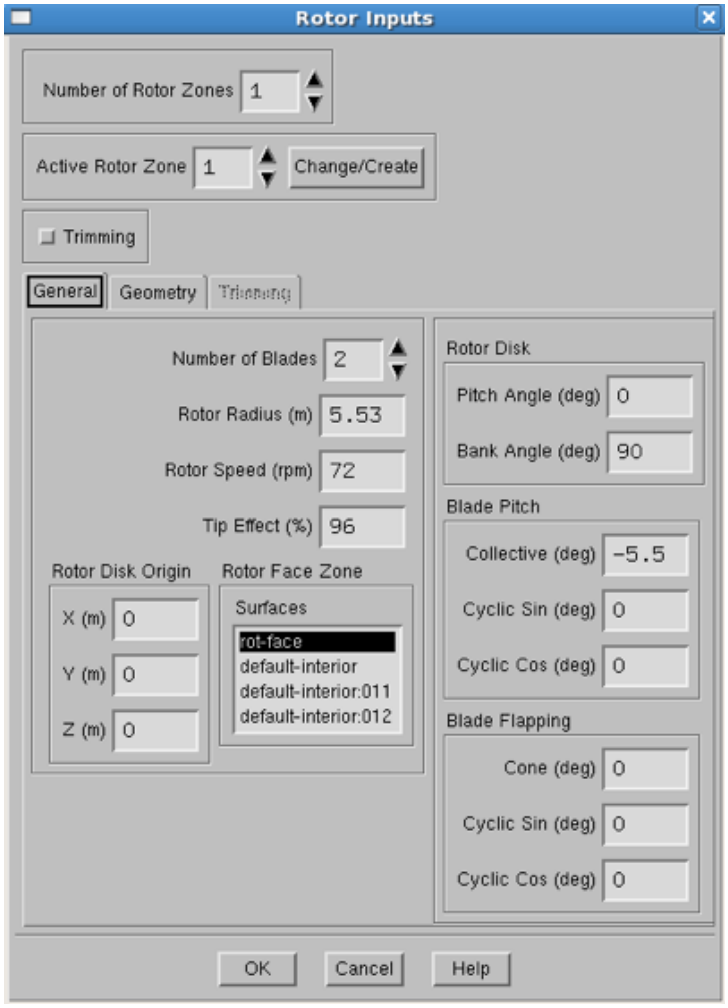

Figure 3.4: VBM panel for entering turbine geometry specifications.

Figure 3.5 shows the panel for geometry input of blade segments. VBM allows the blades to be divided into up to 20 segments. In this panel the details of each segment such as its radial position (r/R), chord length and twist angle is given to the model. The last box for each segment gets the file name for the lift and drag coefficient look-up table. This table has values of lift and drag coefficients as a function of angle of attack, Reynolds and Mach numbers. As explained earlier, at each iteration the lift

and drag coefficients will be read from the look-up table for calculation of lift and drag force on each cell and segment. After setting up the VBM inputs successfully, simulations of the flow around and in the wake of the turbine disk can be performed.

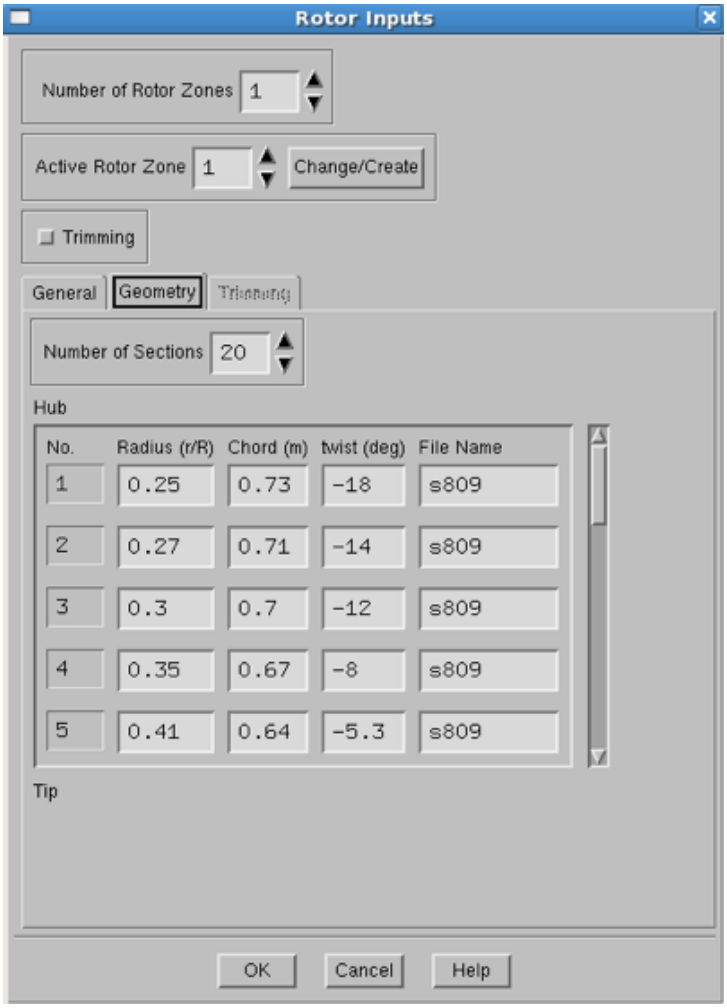

Figure 3.5: VBM panel for entering blade segments input.

3.3 Actuator Disk Model (ADM)

3.3.1 Computational Domain

The computational domain for the ADM simulations is exactly the same as the VBM domain (figure 3.3) with the same boundary conditions and dimensions. The only difference is the way that the actuator disk models the effect of the turbine blades. As it is discussed earlier in subsection 2.3.2, ADM models the effect of the turbine as a porous disk with area equal to the swept area of the turbine blades. The methodology and steps for finding the appropriate coefficients for the porous media to model the turbine were discussed in subsection 2.3.2. Here, the application of this methodology to study of the NREL Phase VI wind turbine is explained in the following subsection.

3.3.2 Numerical Model Settings

The general numerical settings for ADM is the same as the settings for SRF and VBM, as shown in table 3.1. Settings for modeling of the turbine blades effect with ADM is more straight forward in comparison to VBM, since modeling porous media is a built-in model within ANSYS FLUENT. The only necessary step is to find the right coefficients for modeling the actuator disk with a porous media.

Following subsection 2.3.2, in order to calculate the value of the porous coefficients for modeling the NREL Phase VI turbine as a porous media, the value of the inlet velocity is varied between $1 - 7\ [\frac{m}{s}]$, knowing that the free stream velocity in the NREL test was $6.8\ [\frac{m}{s}]$. Efficiency of the device based on SRF and VBM simulation was estimated to be about 29%. Based on these assumptions, the range of u_2, u_3 and ΔP using equations 2.25, 2.23 and 2.22 from ADM theory respectively, will be as follows:

Table 3.2: Developing range of velocity and pressure drop values to calculate porous media coefficients for modeling the NREL Phase VI wind turbine.

Turbine Efficiency	0.29
Axial Induction Factor (a)	0.087
Air Viscosity $[\frac{kg.m}{s}]$	0.0000198
Disk Thickness [m]	0.120

u_1	u_2	u_3	ΔP
1.00	0.913	0.826	0.194
1.50	1.370	1.240	0.437
2.00	1.826	1.653	0.777
2.50	2.283	2.066	1.213
3.00	2.740	2.479	1.747
3.50	3.196	2.893	2.378
4.00	3.653	3.306	3.106
4.50	4.110	3.719	3.931
5.00	4.566	4.132	4.854
5.50	5.023	4.546	5.873
6.00	5.479	4.959	6.989
6.50	5.936	5.372	8.202
7.00	6.393	5.785	9.513

With this set of data, a second order polynomial for pressure as a function of velocity at the the turbine plane (u_2) can be obtained as shown in figure 3.6.

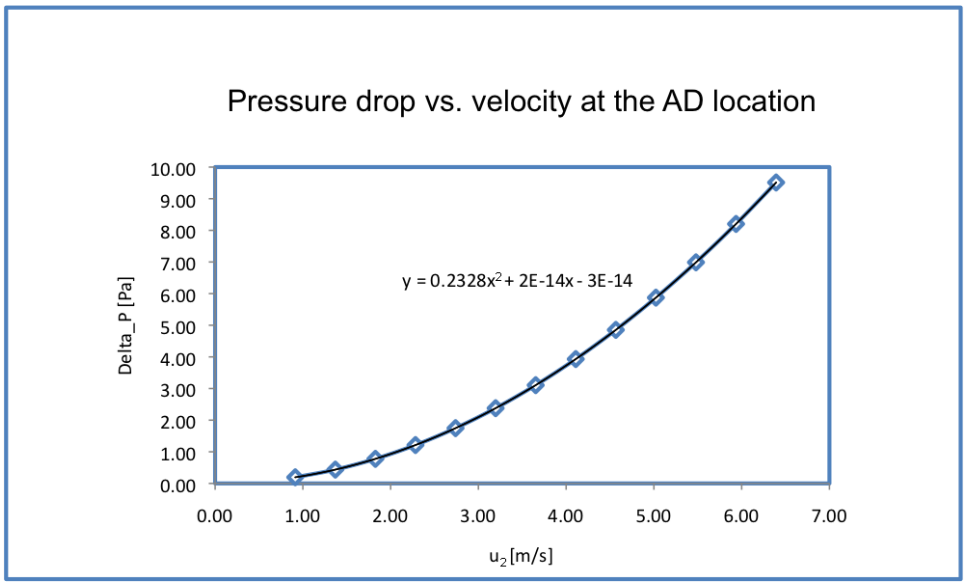

Figure 3.6: The second order polynomial obtained via curve fitting through the data developed from actuator disk theory.

Equating the coefficients of the second order polynomial showed in figure 3.6 with the coefficients of equation 2.29, the unknown porous coefficients α and C_2 can be calculated. With the above numerical values, viscous resistance $\frac{1}{\alpha} \simeq 8.40 \times 10^{-9}$ and inertial resistance factor $C_2 \simeq 3.17$.

Figures 3.8 and 3.7 show the panel were the above calculated variables should be provided for the ADM model. As it can be seen in this panel, the properties of the fluid zone, the actuator disk, are provided for the model. This zone is defined as a 3D porous zone in ADM and the calculated coefficients are set equal to each other for all three directions (x, y, z).

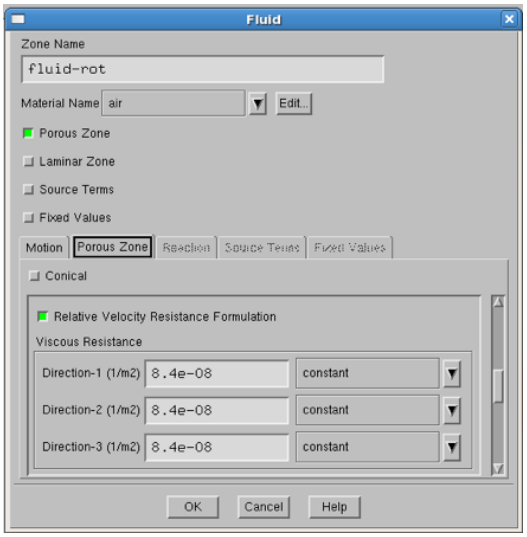

Figure 3.7: Panel for entering the value for inverse of viscous resistance ($\frac{1}{\alpha}$) for porous media modeling the NREL turbine in ANSYS FLUENT.

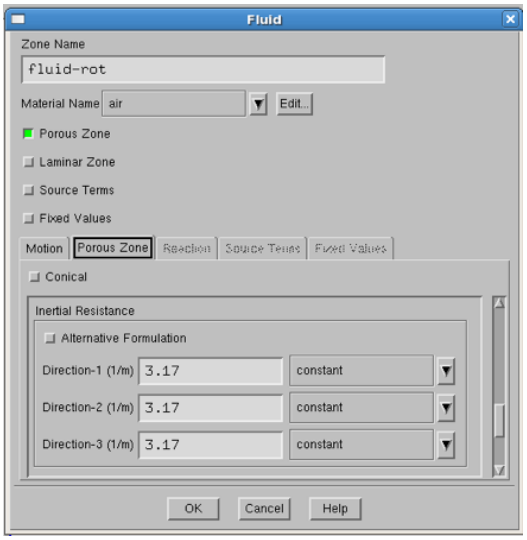

Figure 3.8: Panel for entering the value for inertial resistance (C_2).

3.4 Results

In this section, the validation procedure for the results from the three models, SRF, VBM and ADM, used to model the NREL Phase VI wind turbine is presented. Results, and the physics behind them, are explained for each model. Models are compared with each other to distinguish strengths and weaknesses of each model in capturing the fluid mechanics of the flow going through a turbine and their adequacy to be applied toward the study of a specific environmental problem in tidal energy turbines.

3.4.1 Validation of SRF results agains NREL experimental data

The validation procedure starts with the SRF model. As a first step, the calculated 2D pressure coefficients C_p for the S809 airfoil at different radial positions $\frac{r}{R}$ along the span of the blade were compared against experimental results, and also against previously published numerical data for the NREL Phase VI wind turbine [22]. Figure 3.4.1 and the following four figures, show the calculated pressure coefficients on both suction and pressure sides of the S809 airfoil at different radial positions along the blade span. In these figures, red squares represent calculated pressure coefficients using our 2D mesh with $k-\omega$ turbulent model. Blue squares show the values from modeling the flow around the airfoil using Spalart-Allmaras turbulence model. Black squares are the corresponding experimental values of pressure coefficients for NREL Phase VI wind turbine for a free stream velocity of 7 $\frac{m}{s}$ by Sorensen [22].

The computational results from both turbulent models (i.e. red and blue squares) show good agreement with each other except at the radial position of $\frac{r}{R} = 0.3$ near the trailing edge of the airfoil and also at the leading edge in radial positions near

to the blade tip. But, as it is observed, the computational values from Spallart-Allmaras model show better agreement with the NREL experimental results. Beside that, Spalat-Allmaras showed better numerical stability and converged easier.

These results show overall agreement between the computational results and the available experimental data. As it will be explained in section 4.2.2, the regions around the blade walls are the most important for 3D simulation of the flow around the turbine blade. It is important to discretize the flow domain with an adequate mesh and sufficient spatial resolution to ensure accurate representation of the flow by the numerical simulation. Following figures show the validation of calculated 2D pressure coefficients C_p along blade cross sections at different radial positions $\frac{r}{R}$ on the blade span, using two turbulence models against NREL experimental data [30].

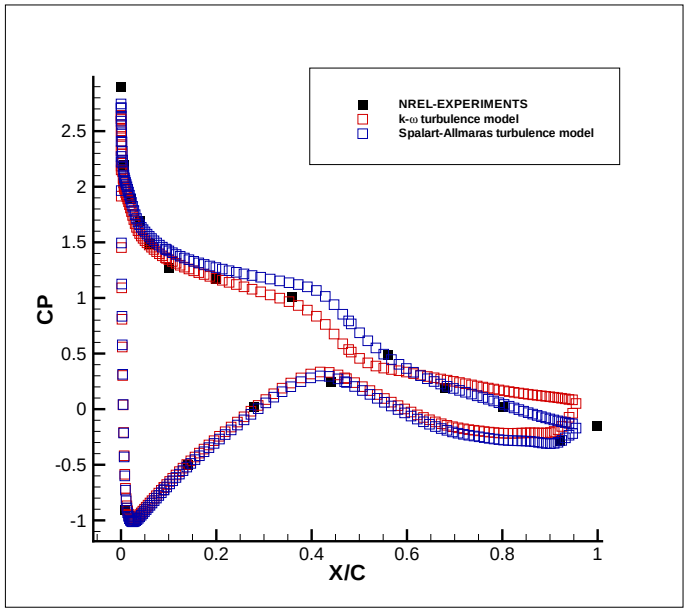

Figure 3.9: Calculated 2D C_p at $\frac{r}{R} = 0.3$

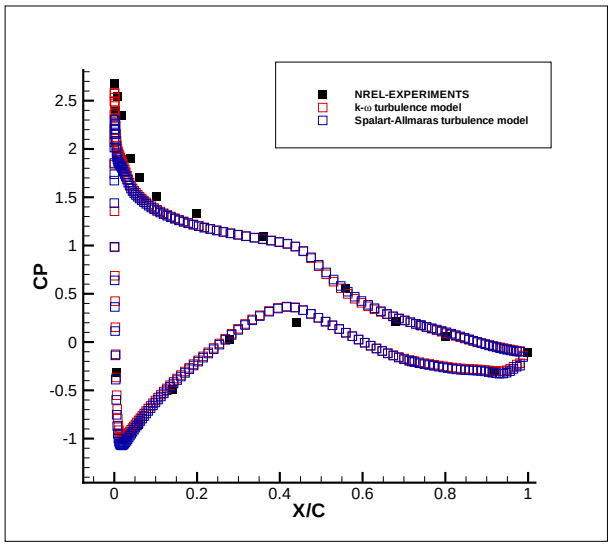

Figure 3.10: Calculated 2D C_p at $\frac{r}{R} = 0.47$

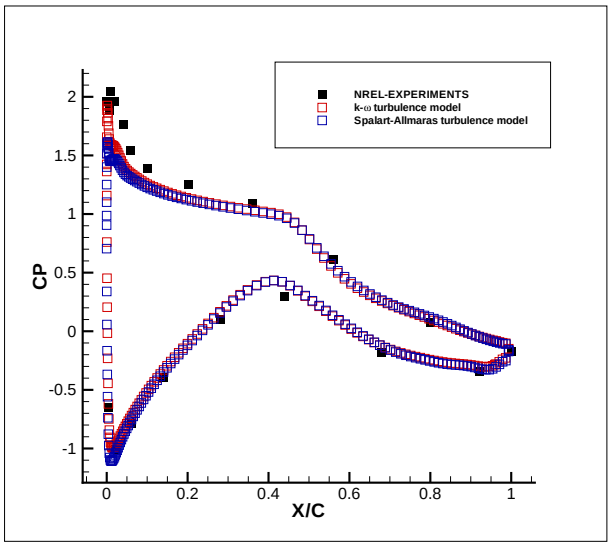

Figure 3.11: Calculated 2D C_p at $\frac{r}{R} = 0.63$

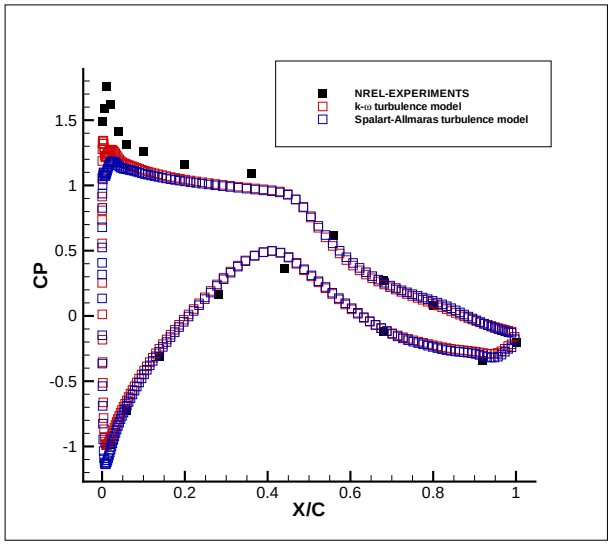

Figure 3.12: Calculated 2D C_p at $\frac{r}{R} = 0.8$

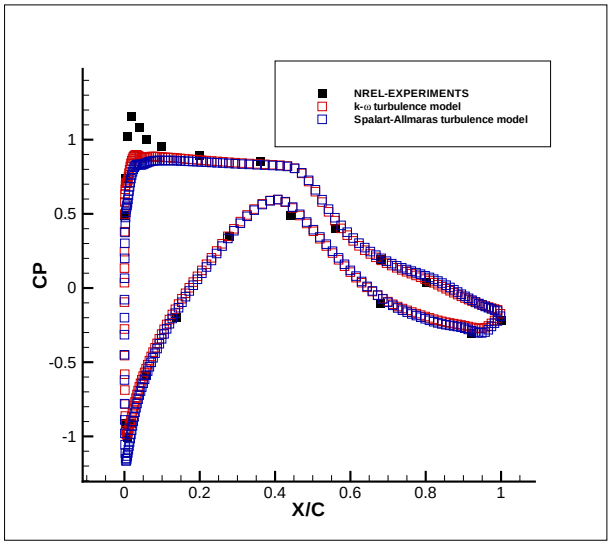

Figure 3.13: Calculated 2D C_p at $\frac{r}{R} = 0.95$

These validated results confirm the accuracy of the simulation technique used to reproduce the flow physics around the turbine blade. These results help build trust on the use of this mesh generation technique, the spatial resolution chosen and the turbulence models tested for the simulation of horizontal-axis wind and marine turbines under similar conditions of operation (limited flow separation). More validation steps against previous studies can be found in the report by Mr. Sylvain Antheaume[30].

3.4.2 SRF results

Figure 3.14 shows velocity contours normalized with the undisturbed free stream velocity on $y = constant$ planes along the computational domain. The sequence of planes starts upstream of the turbine, $\frac{Y}{R} = -0.25$ (left corner top) and move downstream, $\frac{Y}{R} = 2.5$ (right corner bottom). As it is shown in this figure, the flow starts to decelerate as it senses the presence of the turbine blade, which can be seen from the contours transitioning from green to light blue. At the location of the blade, $\frac{Y}{R} = 0$, acceleration of the flow on the suction side of the blade and deceleration on the pressure side are observed. Another phenomenon shown at $\frac{Y}{R} = 0$ is the vortex shedding from the blade tip. Since the tangential velocity at the tip of the blade reaches its maximum value, the vector summation of the axial and tangential velocity components will result in a region of high velocity and low pressure (thin, dark red continuous slice at the tip). Moving further downstream, the tip vortex diffuses in the flow, becomes weaker and disappears.

Moving further away from the turbine, the velocity contour in the wake become more homogeneous. At about 1.5 radii downstream of the blade, the turbulent wake become axisymmetric and further downstream it shows a more homogeneous velocity contour. Observation of this type of flow behavior led us to use less computational intensive models such as VBM and ADM which are capable of simulating the axisymmetric

wake with a good accuracy and low computational cost.

Based on the procedure above and the sample of results shown in figure 3.14 from the SRF simulations that describe the physics of the flow around a blade very well, the SRF model is considered validated. Now, the results from other two models, VBM and ADM, can be compared with SRF results.

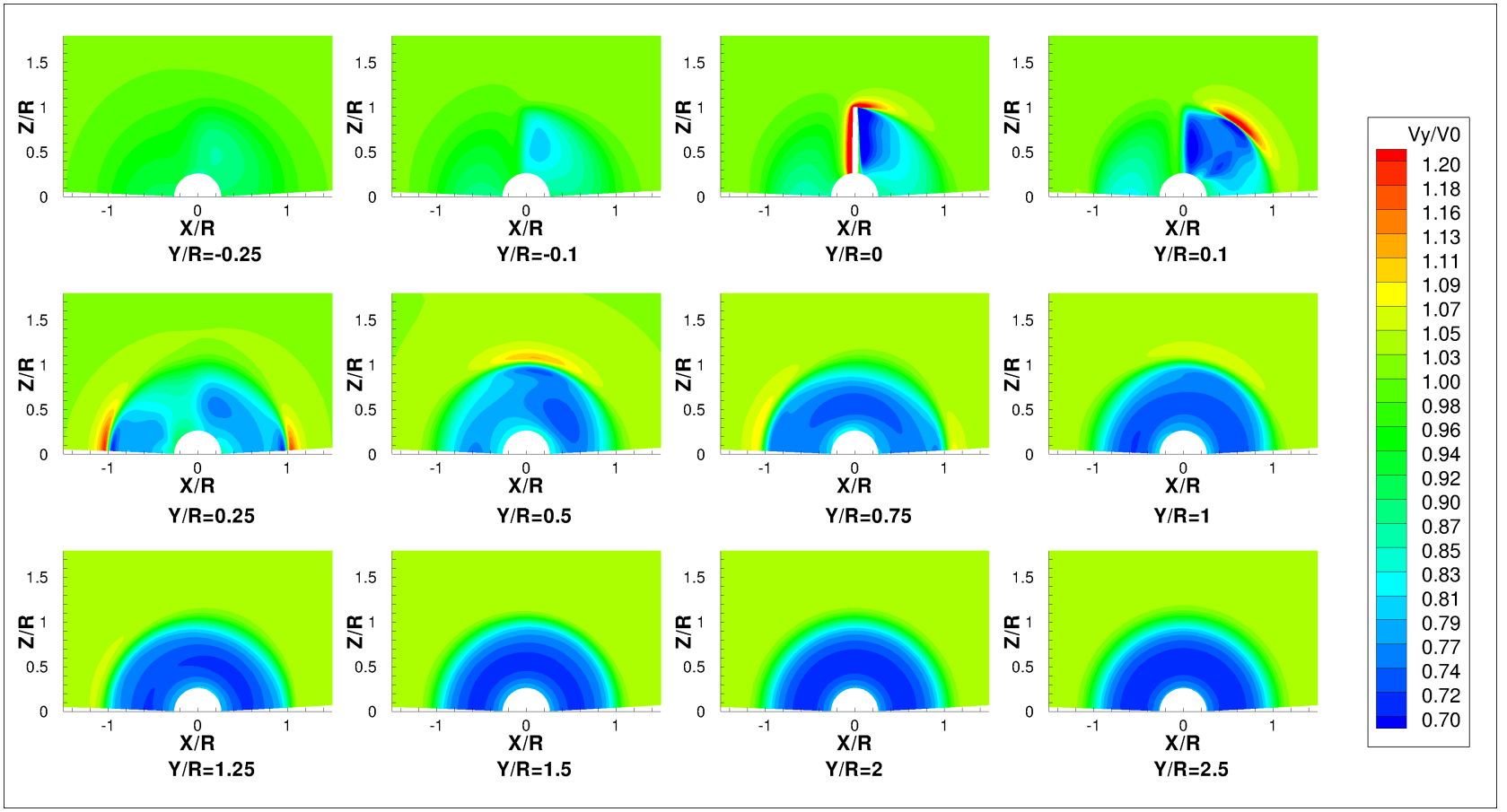

Figure 3.14: Normalized velocity contours on Y-cuts plane along channel.[30]

3.4.3 Comparisons between SRF, VBM and ADM results

Figure 3.15 shows the velocity contours normalized with the free stream velocity on a $y-z$ plane (parallel to the free stream direction) in the middle of channel for each model. Superimposed with the contours, velocity profiles along $y = constant$ lines (perpendicular to the flow direction) show the magnitude of the velocity deficit at different distances downstream of the blade.

The result at the top of the figure 3.15 corresponds to the simulated flow field with the SRF model, which is the most complex among the three studied. As shown, the flow starts to decelerate as it approaches the turbine blade. Right after the blade, in the near wake region, the flow becomes inhomogeneous. This type of detail in the physics of the wake can only be simulated by the SRF model. However, further downstream of the turbine the turbulent wake start to be more uniform and take an axisymmetric shape. An interesting observation in this figure is the vortex shedding, captured in form of small, discrete high speed circles near the tip of the blade. Vortices are stronger closer to the tip, but get weaker as they travel about one radius downstream of the blade, where the vorticity diffuses and eventually disappear in the flow. Velocity profiles, plotted in solid black lines, show the magnitude of the velocity deficit in the wake of the turbine. The maximum deficit occurs closer to the blade and in the near wake region.

The middle figure shows the flow field modeled via VBM. The general fluid mechanics of the flow, such as flow deceleration or shape and color coding of the turbulent wake simulated by this model are in a good agreement with results from the SRF model, but there are some differences between these results that are worth being consideration.

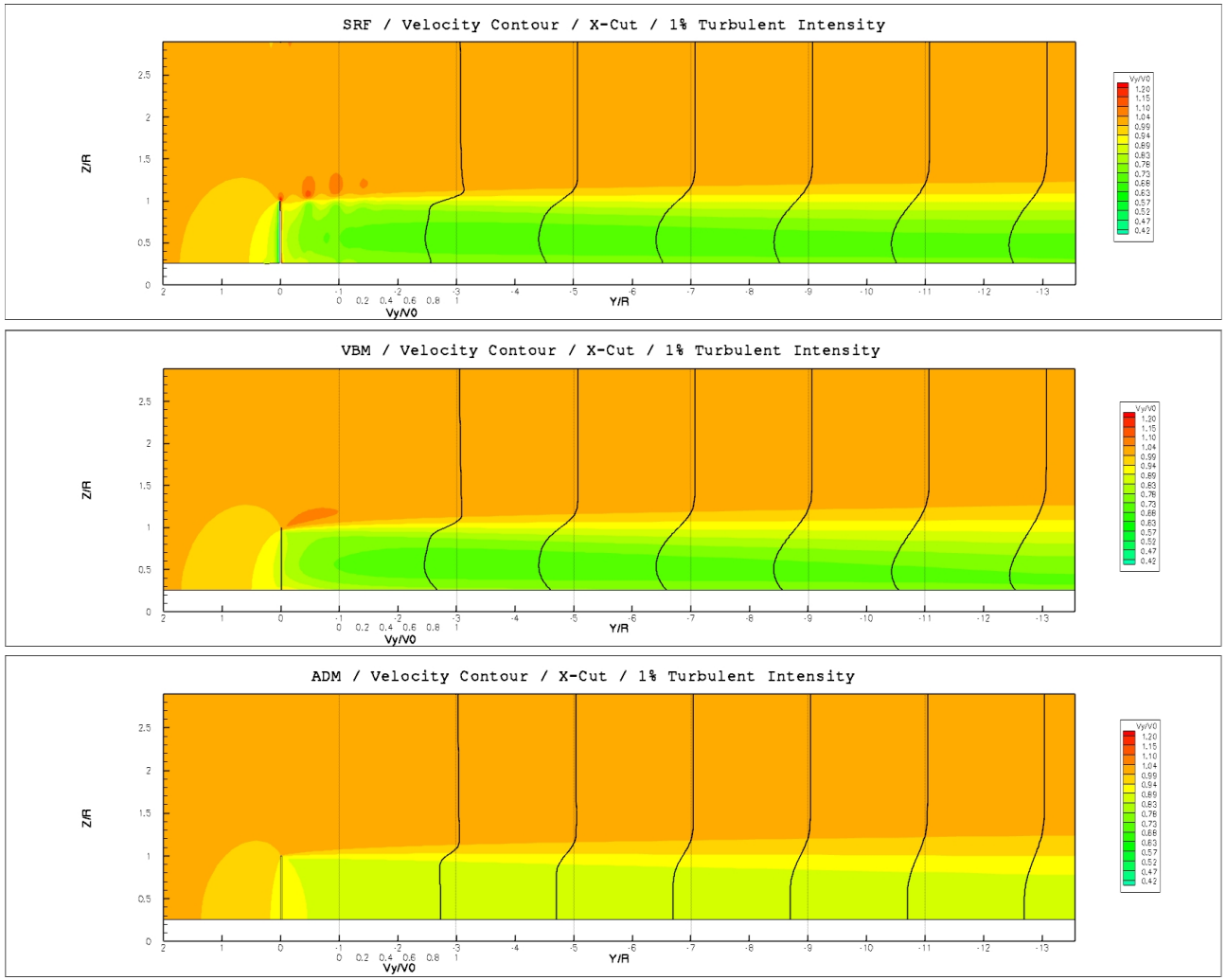

Figure 3.15: Results from modeling NREL Phase VI wind turbine with SRF, VBM and ADM.

The first difference is that the VBM can not capture the detail of the flow right after the blade, since it is averaging the aerodynamic effects of the blade over the whole area of the disk. Therefore the turbulent wake has an axisymmetric shape from the beginning after passing the blade. The second difference is in the modeling of the vortex shedding at the tip of the blade. VBM captures this phenomena in the form of a continuous crown, which again is a result of averaging the blade effect. Despite these two differences, the velocity profiles along the channel from the two models are very similar to each other, particularly after a small distance downstream of the blade. Only the first velocity profile shown, at $Y/R = 1$, have some noticeable differences. All the velocity profiles shown further downstream are in a good agreement with the SRF results. Figure 4.16 shows a more detailed comparison of the velocity profiles, from SRF in black and VBM in blue, superimposed on top of each other in order to visualize the mentioned agreement of the velocity profiles downstream of the turbine. This agreement confirmed our previous conclusion regarding having an axisymmetric wake a few radius downstream of the turbine and therefore the modeling of this type of flow can be done with help of a simpler numerical model such as the VBM. Beside the agreement of point-wise values of the velocity at different locations, we observe agreement between integral quantities such as calculated extracted power and maximum/minimum/average angle of attack [22]. This comparison confirms the hypothesis that VBM simulates the flow crossing a turbine in a good agreement with SRF, while decreasing the computational time and the effort for the geometry creation and meshing process dramatically. Table 3.3 summarize the comparison of integral quantities between SRF and VBM.

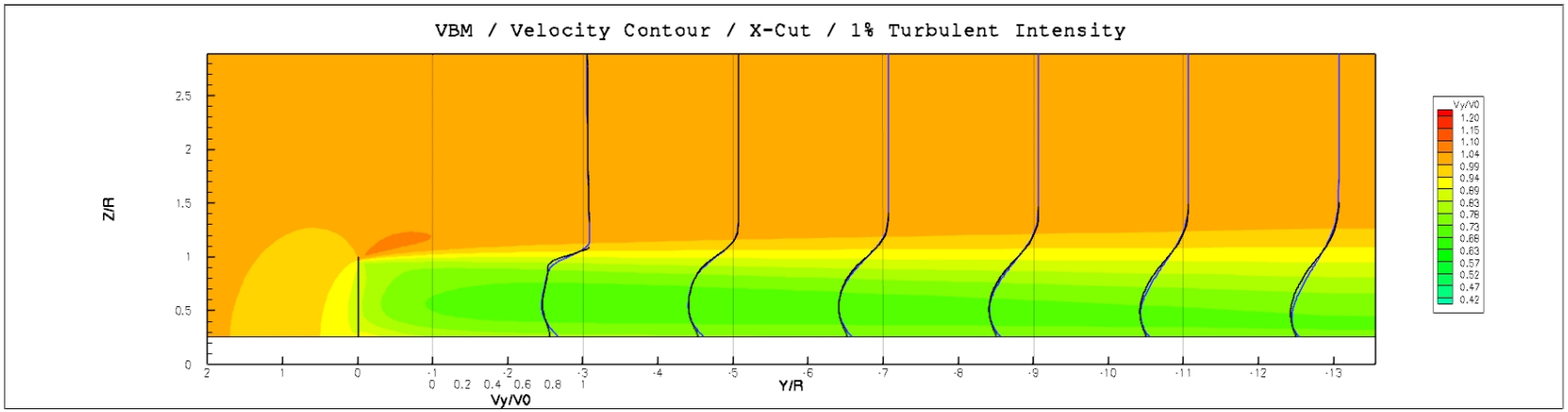

Figure 3.16: Superposition of velocity profiles from SRF model in black and VBM in blue on top of the velocity contour from VBM.

Table 3.3: Quantitative agreements and differences between SRF and VBM model.

Model	SRF	VBM
Number of Mesh Elemenst [mil.]	5.1	1.65
Number of Iterations	12000	2500
Calculation Time	3 days	3 hr
Calculated Power [Watt]	5200	5400
Min./Max. AOA [deg.]	5 - 7	5.11 - 7.54

The third result at the bottom of figure 3.15 shows the simulated flow using the ADM, the simplest model in this numerical methodology. As it can be inferred from the result, a gradual decrease in velocity occurs across the disk, but neither the details of the flow right after the blade nor the tip vortex shedding are being captured by this model. The modeled velocity deficit by the ADM in the near wake region is significantly different than the corresponding velocity deficits from SRF and VBM. Instead of a smooth, curved shape that is observed in the deficit modeled with SRF and VBM, it has a skewed shape. However, moving further downstream of the turbine the skewness becomes smaller and the shape of the velocity deficit get closer to the shape of the corresponding velocity profiles modeled with SRF and VBM. Despite this weak agreement of the initial results with the ADM, the main advantage of this model is its minimal computational time requirement, less than an hour, for simulating the flow with the same mesh size as the VBM.

As a conclusion, since the SRF model captures the details of the flow in the near wake region and tip vortex shedding, it can be applied to near wake studies, blade design, optimization and other types of studies where details of the flow field in the near wake region are required. It should be noted that this detailed modeling implies high

computational time. Beside that, the time required for creating the SRF geometry and mesh is significantly longer than that for the VBM and ADM simulations. For example, for the current geometry and mesh generation for NREL Phase VI wind turbine, it took several weeks, but the time required for VBM and ADM geometry and mesh creation was only a few days. This points to the complicated mesh structure required for the SRF and resolving the small scales at the blade wall as well as large scales away from the walls. As mentioned earlier, since the VBM averages the aerodynamic effects of the blades, it requires dramatically less computational time in comparison to the SRF (see table 3.3), but this also results in a less accurate simulation of the flow in the near wake region. On the other side of the spectrum, detailed comparisons of the results from SRF and VBM show a very good agreements in modeling the flow field in far wake regions of the turbine. Therefore, for the study of the far wake region and turbine interaction in array of turbines, the VBM is suggested. At this stage, ADM showed only qualitative agreement with the results from SRF and VBM. However, its computational time requirement, which is less than an hour, makes it applicable for quick and rough simulations to get a first take on the modeling of turbine arrays and the interaction of downstream turbines with the wake of upstream devices.

3.4.4 SRF, VBM and ADM results with more realistic boundary conditions

As it was stated at the beginning of this chapter, boundary conditions for the first set of runs to model the NREL Phase VI wind turbine were based on NREL experiment conditions. The value of turbulent intensity (see subsection 4.2.4) at the inlet of the channel was set to 1%. This value corresponds to a well-designed wind tunnel such as NASA AMES wind tunnel, where the NREL Phase VI turbine was tested. It is not representative, however, of realistic field conditions for either wind or tidal turbine applications. A simulation with 10% turbulent intensity at the inlet was performed to assess the influence of this variable on the results produced by the three models under comparison. This was estimated to be a conservative value, representative of a high energy fields of wind turbines.

Figure 3.17 shows results from NREL Phase VI turbine modeling, with 10% turbulent intensity. As it can be observed in the results, the turbulent wake behind the turbine decays faster and velocity profiles along the channel have different shapes when compared to the case with lower turbulent intensity. This goes back to the fact that the magnitude of the turbulent velocity fluctuations is larger and diffusion is enhanced in the flow. Results from SRF and VBM are similar to the case with 1% turbulent intensity, and are in very good agreement. The small differences in the velocity profiles for the near wake region are attenuated. The ADM simulation also shows more promising results and a better agreement with the velocity profiles from the SRF and VBM results downstream of the turbine.

Having more realistic results by using a more representative value of the background turbulent intensity, led us to include the Actuator Disk Model (ADM) to our validated numerical methodology in order to study flow behavior around Marine Hydrokinetic (MHK) turbine arrays and optimize their arrangement in a farm of devices.

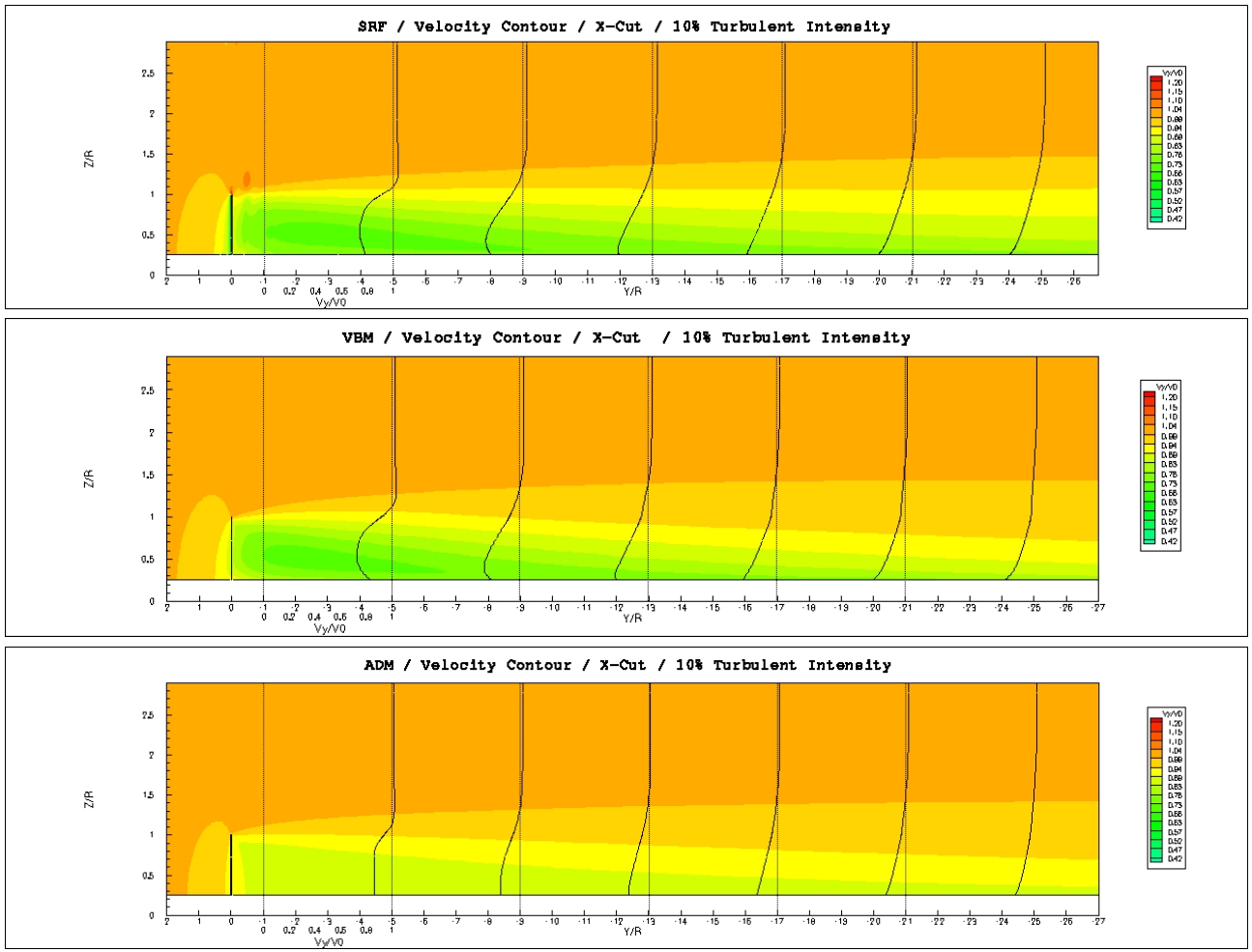

Figure 3.17: Results from modeling NREL Phase VI turbine with SRF, VBM and ADM with Increased value of turbulent intensity to 10% at the inlet.

Chapter 4

APPLICATION OF OUR VALIDATED NUMERICAL METHODOLOGY TO THE STUDY OF MARINE HYDROKINETIC (MHK) TURBINES

4.1 Introduction

As it was pointed out earlier in chapter 1, Marine Hydrokinetic (MHK) turbine technology is currently in the phase of research and development. Most of the companies and research institutes are therefore hesitant to announce the specifications of their development devices, such as geometry, blade design, materials for different parts of the structure and results of their preliminary tests. However, wind turbine technology can be considered a well-developed technology. Therefore, a wealth of information, in the form of papers and technical reports, are publicly available on this subject. Based on the similarities of this technology with MHK turbine technology, the available studies of wind turbines can be used as a starting point for the study of MHK technology. For example, the availability of numerical and experimental tests on the NREL Phase VI wind turbine [21][22] offered the opportunity to validate our methodology under relevant operating conditions before moving to the study of MHK turbines.

Now that we have validated our numerical models with publicly available results for the NREL Phase VI wind turbine, these models need to be modified to study a MHK turbine, which is the main research goal of this thesis. These modifications need to be done step by step in order to approach the desired conditions and geometry for a MHK turbine that operates in an estuary or a tidal channel. These modifications will lead us to a set of realistic modeling conditions and a framework for optimization of

blade design and study the potential environmental effects of MHK turbines.

4.2 Changing the Working Fluid from Air to Water in SRF model

4.2.1 Free stream and angular velocity modification

The first step in applying the validated numerical methodology to study of the MHK turbines is changing the working fluid from air to water inside the computational domain. However, this transition needs to be done with consideration of two fundamental changes. First one is variation of the boundary conditions, such as free stream velocity of the flow at the inlet of the domain and angular velocity of the MHK turbine rotating blades, which are related to each other by the definition of the tip speed ratio (TSR). Second one is the significant changes in fluid variables such as density and viscosity and therefore non-dimensional numbers such as the Reynolds number. These fundamental changes might lead to some variable value comparison with different thresholds and re-meshing the computational geometry, that will be discussed in detail in the following sections.

First we address and investigate the changes in boundary conditions and resulting phenomena from these changes such as cavitation that was not a concern in modeling wind turbines. During the modification of the TSR to the realistic values for modeling a MHK turbine, the effective angle of attack along the blade and the possibility of cavitation should be checked to avoid flow separation along the blade and cavitation happening near the blade surface.

Flow separation is an undesired phenomenon, because it reduces lift, results in a decrease of the efficiency of the device and produces complex flow near the blade surface. Cavitation is often a limiting design criterion for different devices handling liquids, such as hydrokinetic turbines, propellers, and pumps. It can affect device performance, decreasing power output and efficiency of hydrokinetic turbines or a

drop in efficiency and head produced by pumps. It can also cause vibration, noise and in the most extreme cases mechanical erosion and pitting of the surfaces near which cavitation occurs (see figures 4.1 and 4.2).

A design driver for MHK turbines is the potential cavitation on the MHK turbine blade surface. This type of cavitation occurs due to the low pressure found in the core of the blade tip vortex corresponding to the high velocity fluid shedding from the tip of the blade. A decrease in pressure below the vapor pressure of water at a specific temperature leads to nucleation, growth and a quick burst of vapor bubbles in the flow and near the blade surface. The process of bubbles bursting close to the surface of the turbine blade will result in a very strong microscale jet impingement on that area. Repetition of this process over a long period of time can lead to serious damage and failure of the blade [31]. Therefore maintaining a reasonable interval for rotor tip speed and having an adequate blade design to avoid cavitation and flow separation along the blade is an important criteria in the design of MHK turbines.

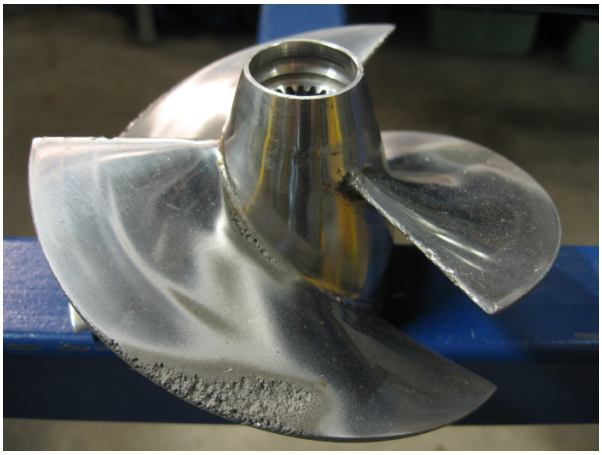

Figure 4.1: Small amount of pitting on a the propeller of a personal watercraft.

Figure 4.2: Catastrophic failure in the concrete wall of the 15.2 [m] diameter Arizona spillway at the Hoover Dam caused by cavitation.

In order to roughly estimate a threshold for blade tip speed to avoid cavitation at the tip of the blade, one can apply Bernoulli's equation along a streamline between a point at the inlet of the channel and a point at the tip of the blade, where the pressure value is important to predict cavitation (points 1 and 2 respectively, in figure 2.2). Assuming that free surface of water is the reference height and blade tip (point 2) is $10[m]$ below the free surface. Then point 1 at the inlet, which is along the centerline of the hub is $15.5[m]$ below the free surface. The velocity at the inlet is $2[\frac{m}{s}]$. Static pressure at point 1 is about $255[kPa]$ and the threshold value for the pressure at point 2 will be vapor pressure of water at 20 °C, which is about $2.3[kPa]$. With these assumptions the calculated critical velocity at the tip using Bernoulli equation will be about $23[\frac{m}{s}]$. Considering a value of Cp_{min}* for the blade equal to 2, a rotor tip speed between $10 - 13[\frac{m}{s}]$ would avoid potential cavitation. It should be noted that increasing the depth of the deployed device will increase this threshold, due to the

*For more details on cavitation scaling readers are referred to [31].

increase in hydrostatic pressure in water.[†]

Table 4.2 shows an estimate of the angle of attack and rotor tip speed for different turbine operating conditions used to select conditions that avoid cavitation and, to the degree possible, flow separation on the suction side of the blade.

As first test, a free stream velocity of 2 $[\frac{m}{s}]$ was considered [25] and the angular velocity was varied between $10 - 20$ $[rpm]$ [1]. As it is shown in table 4.2, a rotor angular velocity of 17 $[rpm]$ with free stream velocity of 2 $[\frac{m}{s}]$ is a suitable choice for this geometry. The resultant tip speed ratio (TSR) is also in the same order of magnitude in compare with other similar designs of tidal turbines, such as Marine Current Turbine (MCT) and Verdant Power turbine as shown in table 4.1. Later it will be shown that the calculated maximum and minimum angle of attacks for this TSR are in a range that extreme flow separation on the span of the blade is avoided. Furthermore, the calculated value of the rotor tip speed is below the stated criteria in a way that potential tip vortex cavitation will be avoided as well.

Tidal Turbine Design	Marine Current Turbine	Verdant	NREL Phase VI
Rotor diameter [m]	16.00	5.00	11.06
Max. angular velocity [rpm]	14.30	40.00	17.00
Tides velocity $[\frac{m}{s}]$	2.50	2.50	2.00
Tip Speed Ratio (TSR)	4.80	4.20	4.90

Table 4.1: Comparison of the matched TSR for NREL Phase VI with the TSR of similar tidal turbines [1].

[†]This estimation is in a good agreement with our information based on a personal communication with Peter Fraenkel at Marine Current Turbines. It indicates that for devices with approximately 3-5 meters overhead clearance at top of the rotor the critical blade tip speed would be between $10 - 12[\frac{m}{s}]$.

Table 4.2: Values of geometric specifications of NREL Phase VI turbine, rotor tip speed, maximum and minimum angle of attack with different rotor angular velocity for free stream velocity of 2 $[\frac{m}{s}]$.

Radii at tip [m]	5.53
Radii at root [m]	1.343
Pitch at tip [degrees]	3
Twist at tip [degrees]	-2.5
Twist at root [degrees]	18
$V_\infty[\frac{m}{s}]$	2

Angular velocity [rpm]	Angular velocity $[\frac{rad}{sec}]$	Tip Angle of Attack [degrees]	Root Angle of Attack [degrees]	Tip Speed Ratio (TSR)	Rotor Tip Speed[a] $[\frac{m}{s}]$
10.00	1.05	18.55	33.89	2.90	6.13
11.00	1.15	16.93	31.28	3.19	6.68
12.00	1.26	15.56	28.84	3.47	7.23
13.00	1.36	14.38	26.57	3.76	7.79
14.00	1.47	13.36	24.45	4.05	8.35
15.00	1.57	12.47	22.47	4.34	8.91
16.00	1.68	11.68	20.63	4.63	9.48
17.00	1.78	10.98	18.91	4.92	10.05
18.00	1.88	10.36	17.31	5.21	10.61
19.00	1.99	9.80	15.81	5.50	11.18
20.00	2.09	9.30	14.41	5.79	11.75

[a]Value of rotor tip speed should be below 10-12 $[\frac{m}{sec}]$ in order to avoid tip vortex cavitation.

4.2.2 Mesh modification

As it is discussed before, the significant changes in fluid variables such as density, viscosity and therefore non-dimensional numbers like Reynolds number is the second major change in transition of the working fluid from air to water. This significant change in the kinematic viscosity value, ν, for water in compare to air, beside the changes of free stream and angular velocity result in a higher value of Reynolds number. Therefore, the previous mesh of the SRF computational domain needs to be modified and re-created in some blocks of the domain in a way that the detail of the turbulent flow with higher Reynolds number is being captured and a successful flow field simulation can be obtained.

This mesh modification/re-creation is particularly important in the regions near the blade, where the dimensions of the boundary layer change due to the change in Reynolds number associated with the change in working fluid and velocity components. Generally, the presence of walls affect the turbulent flow in various ways. First of all, the mean velocity field is affected by the no-slip wall boundary condition that needs to be satisfied at the wall. Second, at distances very close to the wall, viscous damping reduces the tangential velocity fluctuations, while kinematic blocking reduces the normal fluctuations. Furthermore, moving further from the near wall region, the turbulence is rapidly augmented by the production of turbulence kinetic energy due to the large gradients in mean velocity. In this near-wall region the solution variables have large gradients and the momentum and scalar transport occur most vigorously. The size of this near wall region, where all these physical interactions happen, is in order of few millimeters, therefore very small in comparison to the other length scales in the domain, which are in order of meters. Hence, either a high resolution mesh or an accurate model for the near-wall behavior should be provided in order to capture the details of a turbulent flow in this region accurately. An accurate representation of

the flow in this region is necessary for a successful prediction of the overall behavior in turbulent flows.

As it is shown in figure 4.3, the near wall region can be divided into three distinct sublayers based on the type of the physical interactions happening inside that region of the flow (section 7.1.3 in [32]). The innermost layer, where viscosity plays the major role in momentum, heat and mass transfer, is called the viscous sublayer. The middle layer in which the effects of molecular viscosity and turbulence are equally important is referred to as the buffer layer. The outer layer where turbulence plays the major role is called the fully turbulent region. In this figure y^+ ($y^+ = \frac{u_\tau y}{\nu}$) is the non-dimensional wall distance defined in terms of the wall friction velocity and the fluid viscosity, and is the key value used in the turbulence wall models that will be discussed shortly.

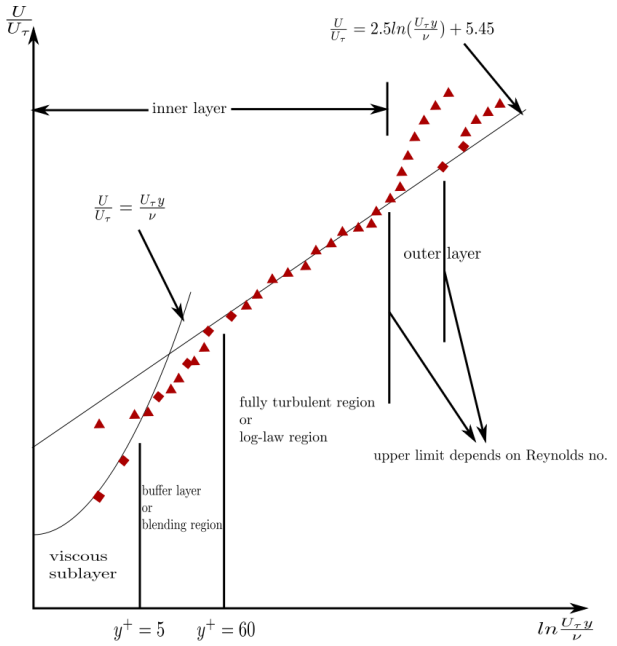

Figure 4.3: Three distinct divisions inside the near wall region. Taken from [24]

There are two different approaches for modeling the near wall region. The first one is called near wall capturing, in which the turbulence model applied to the interior of the domain is modified to enable the viscous-affected region to be resolved with a mesh all the way to the wall, including the viscous sublayer. The second approach is referred to as wall functions, in which the viscous-affected inner regions, viscous sublayer and buffer layer, are not resolved. Instead, a semi-empirical formula is used within the mesh to bridge the gap between the wall and the fully turbulent region, which is resolved in the mesh. The wall function accurately represents the effect of the unresolved region in the behavior of the flow in the resolved regions, allowing for the calculation of mean velocity profiles, flow detachment, dissipation, mean shear on the wall, etc. Figure 4.4 shows a schematic of these two different approaches.

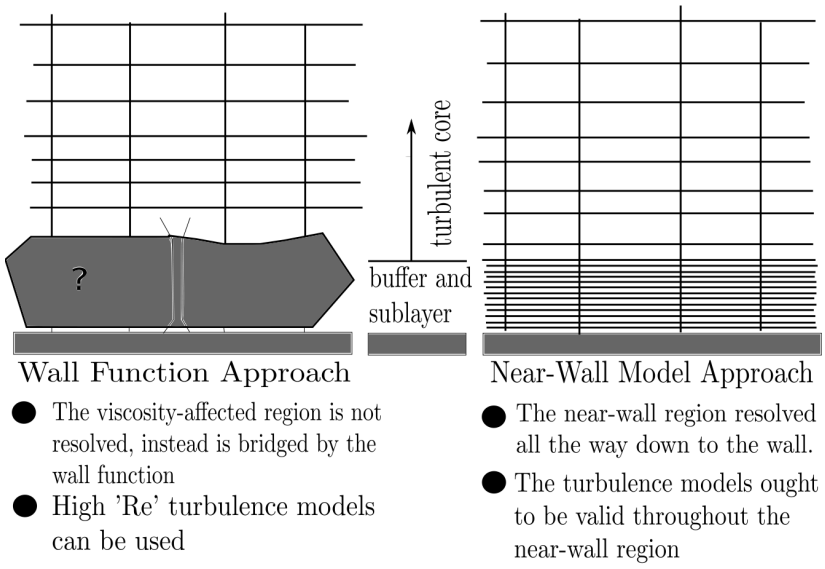

Figure 4.4: Schematic of wall function and near wall model approach. Redraw from[24]

The wall function approach substantially saves computational resources, since the two inner regions, viscous sublayer and buffer layer, in which the solution variables change most rapidly do not need to be resolved. This makes the wall function approach economical, robust, and reasonably accurate for near-wall treatment of industrial flow simulations, which is our case of study here. Hence, the wall function is preferred and used in our modeling.

To model the turbulent flow in the near wall regions using the wall function approach for a coarse mesh with standard or non-equilibrium wall functions, each wall-adjacent cell centroid should be located roughly within the log-law layer $30 < y^+ < 300$. A y^+ value of 30 close to the lower bound is more desirable. Since y^+ is a function of density, velocity and viscosity, and the values of these variables are modified when we apply the developed methodology to the simulation of MHK turbines. Therefore, mesh used for validation of the methodology for the NREL Phase VI wind turbine needs to be modified.

The exact expression for y^+ is

$$y^+ = \frac{u_\tau y}{\nu}, \tag{4.1}$$

where y and ν are the nearest distance to the wall and kinematic viscosity of the fluid, respectively. u_τ is called the friction velocity defined as

$$u_\tau = \sqrt{\frac{\tau_\omega}{\rho}}. \tag{4.2}$$

For the purpose of generating the mesh which satisfies that the first cell centroid from the wall is in the range of $30 < y^+ < 300$, we estimate the value of y^+, a priori, to be as

$$y^+ = \sqrt{\frac{\rho u y}{\mu}}. \tag{4.3}$$

In equation 4.3 fluid properties such as density and dynamic viscosity are known. Velocity component u is the relative velocity at the corresponding section of the

blade. It is equal to the vector summation of horizontal velocity, approximated as V_∞, and tangential velocity ($r\omega$) at that section of the blade. Therefore, by knowing the minimum value for y^+ from the above mentioned interval, the value of the nearest distance between the blade wall and centroid of the first cell on top of the blade wall, y, is calculated. With this information the mesh is generated for the cell near the blade wall, within the required range of y^+. This allows the wall function approach to accurately capture the effect of the turbulent flow near the blade walls. The nearest distance y can be calculated for both the tip and root of the blade, where the relative velocity component, u is different, and the mesh spacing evolves smoothly between those values, while keeping a reasonable cell count and satisfying the condition $30 < y^+ < 300$.

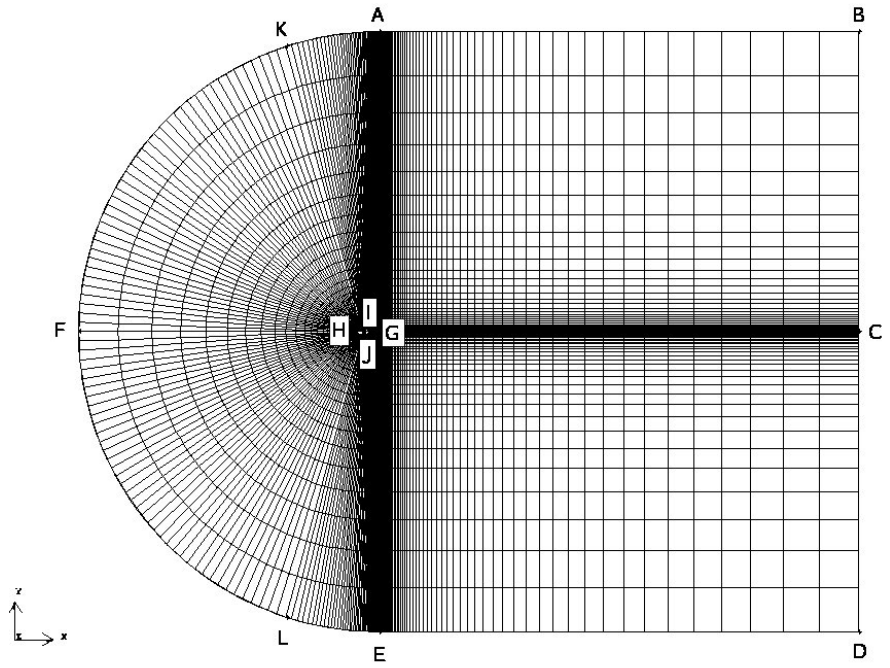

Figure 4.5: Zoom out view of the C-mesh around the blade cross section

Figures 4.5 shows the C-mesh around a two dimensional S809 airfoil and the auxiliary blocks around the blade section. In the validation runs described in chapter 3 with a free stream and rotor angular velocity of 6.8 $[\frac{m}{s}]$ and 72 $[rpm]$ respectively, the distance from the nearest cell centroid to the wall was 0.0021 $[m]$, but for the application to MHK turbine, with a free stream and rotor angular velocity of 2 $[\frac{m}{s}]$ and 17 $[rpm]$ respectively, it is about 0.0004 $[m]$. The new value is 5 times smaller than the old one. This results in a more complex mesh and requires much higher cell counts in the region near the blade walls. Figure 4.6 shows the difference in the mesh density near the blade section. As it is shown, the concentration of the cells around a MHK turbine blade section appears as a continuous blue strip and small cells can not be differentiated from each other in that region, but for the NREL Phase VI wind turbine the small cells near the wall of the blade cross section are differentiable without a need for zoom in.

Once the new mesh was generated and the new boundary conditions were determined, simulations were conducted for the SRF model. Following are some characteristic results for flow simulation around a MHK turbine blade using the SRF model.

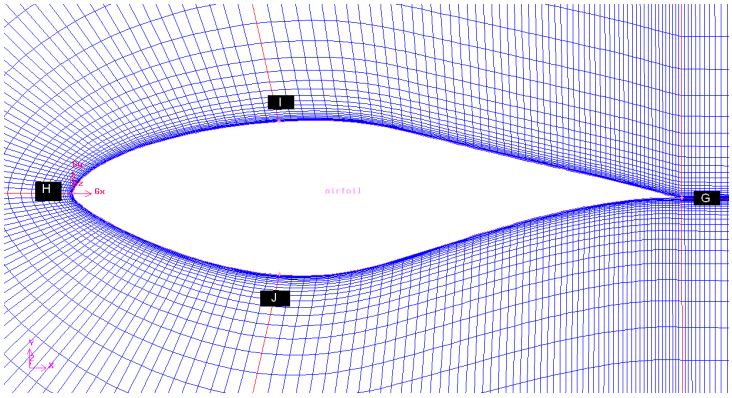

(a)

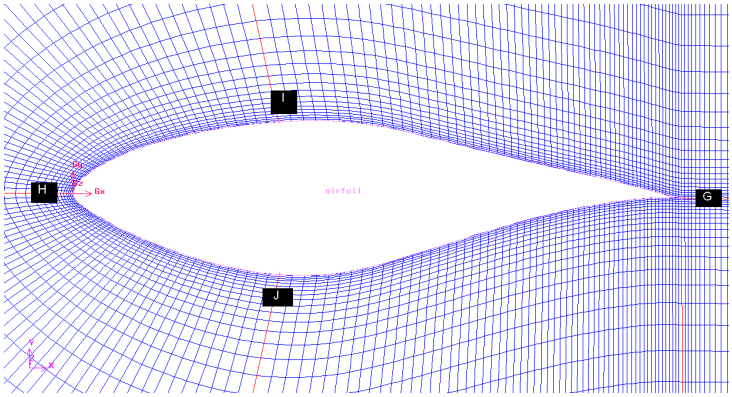

(b)

Figure 4.6: Zoom in of mesh around the blade walls. Airfoil of a MHK turbine blade (a) and mesh around the NREL Phase VI wind turbine airfoil (b)

Figure 4.7 shows the pressure contours on Y-cut planes along the tidal channel. The first plane is located at $\frac{Y}{R} = -0.25$ and is shown at the top left of figure 4.7. This plane is right before the turbine blade in the computational domain. The following planes are further downstream along the channel, to the bottom left of the figure, and show the pressure contours at the location of the blade and the other location till 2.5 radii downstream of the blade. As it can be observed in these results, right

before the turbine, when the flow sense the existence of the blade, its pressure starts to increase and is showed as orange and red regions in Y-planes at $\frac{Y}{R} = -0.25$ and $\frac{Y}{R} = -0.10$ respectively. At the location of the blade, $\frac{Y}{R} = 0$, pressure and suction sides of the blade are shown with dark red and dark blue contours respectively. At the tip of the blade there is a dark blue region, which shows the tip vortex formed in that region of the blade, where the pressure is at it's minimum value. On the next plane at $\frac{Y}{R} = 0.10$ pressure value decreases in front of the blade. Moving further downstream of the blade, pressure starts to go back to the pressure at the inlet and, at the location $\frac{Y}{R} = 1.00$, the effect of the blade can not be observed anymore.

Figure 4.8 shows the corresponding velocity contours on the same Y-planes, showed in figure 4.7. These results are similar to velocity contours presented for flow simulation around the NREL Phase VI wind turbine blade on the figure 3.14. Similar to the results for a wind turbine, the flow decelerates as it gets closer to the blade on the first two planes at $\frac{Y}{R} = -0.25$ and $\frac{Y}{R} = -0.10$. At the blade location $\frac{Y}{R} = 0$ velocity decreases significantly on the pressure side of the blade and on the suction side it gets to its maximum value. At the blade tip the high velocity region corresponding to the region of low pressure, where the blade tip vortex formed, is shown. As we move downstream of the blade along the tidal channel, the wake becomes more and more homogeneous and at location $\frac{Y}{R} = 2.00$ the flow gets an axisymmetric shape.

It should be noted that, this type of detailed results regarding fluid mechanics in the near vicinity of the blade can be produced only from simulation with the SRF model among the available models in our methodology. The similarity of these results to the ones in the step of validating numerical models against NREL experimental data confirm that the process of application of our methodology for studying a MHK turbine is on the right track, although more detailed comparisons is needed to confirm the success of this process, which will be presented in the following sections.

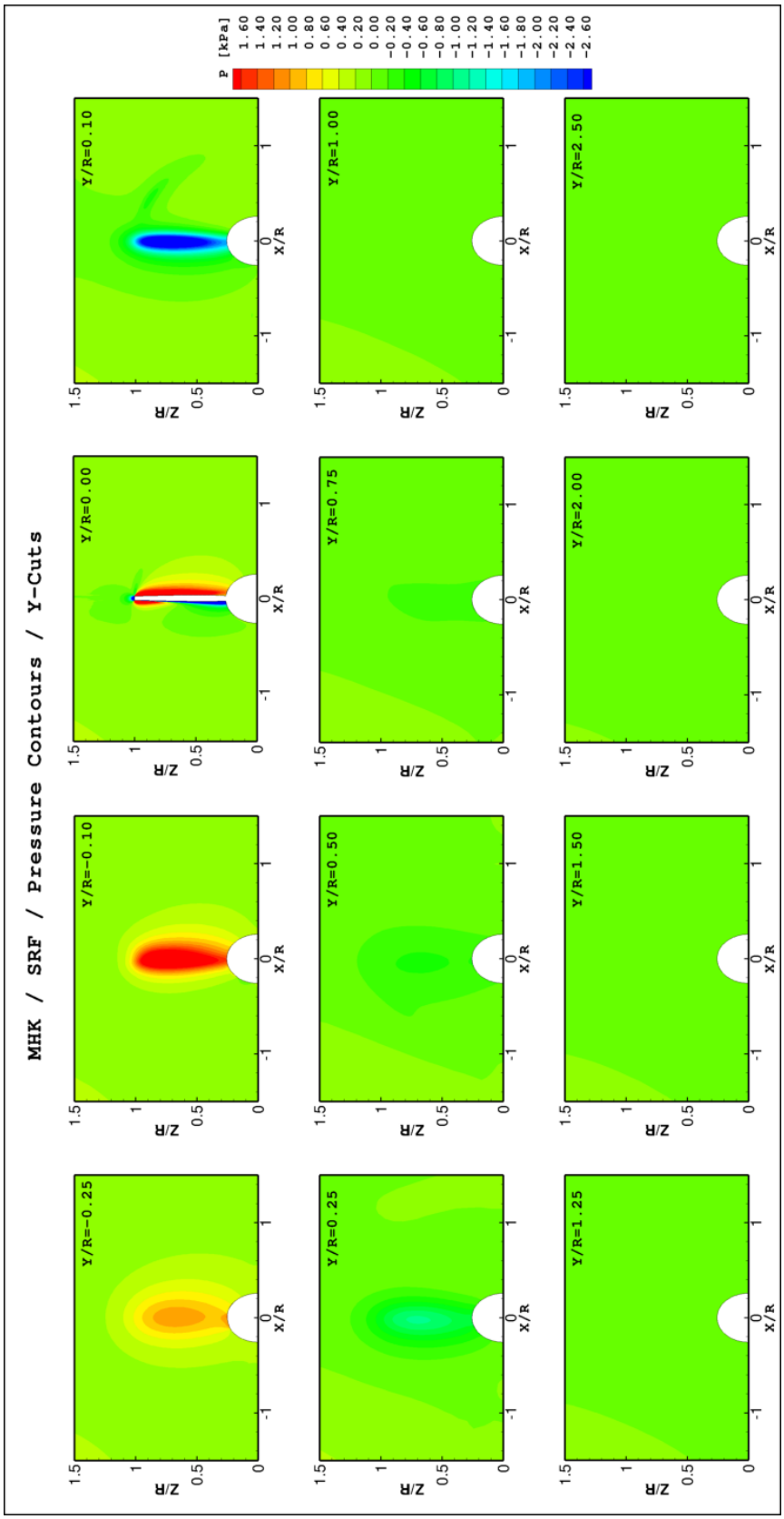

Figure 4.7: Pressure contours on Y-cuts plane along a tidal channel.

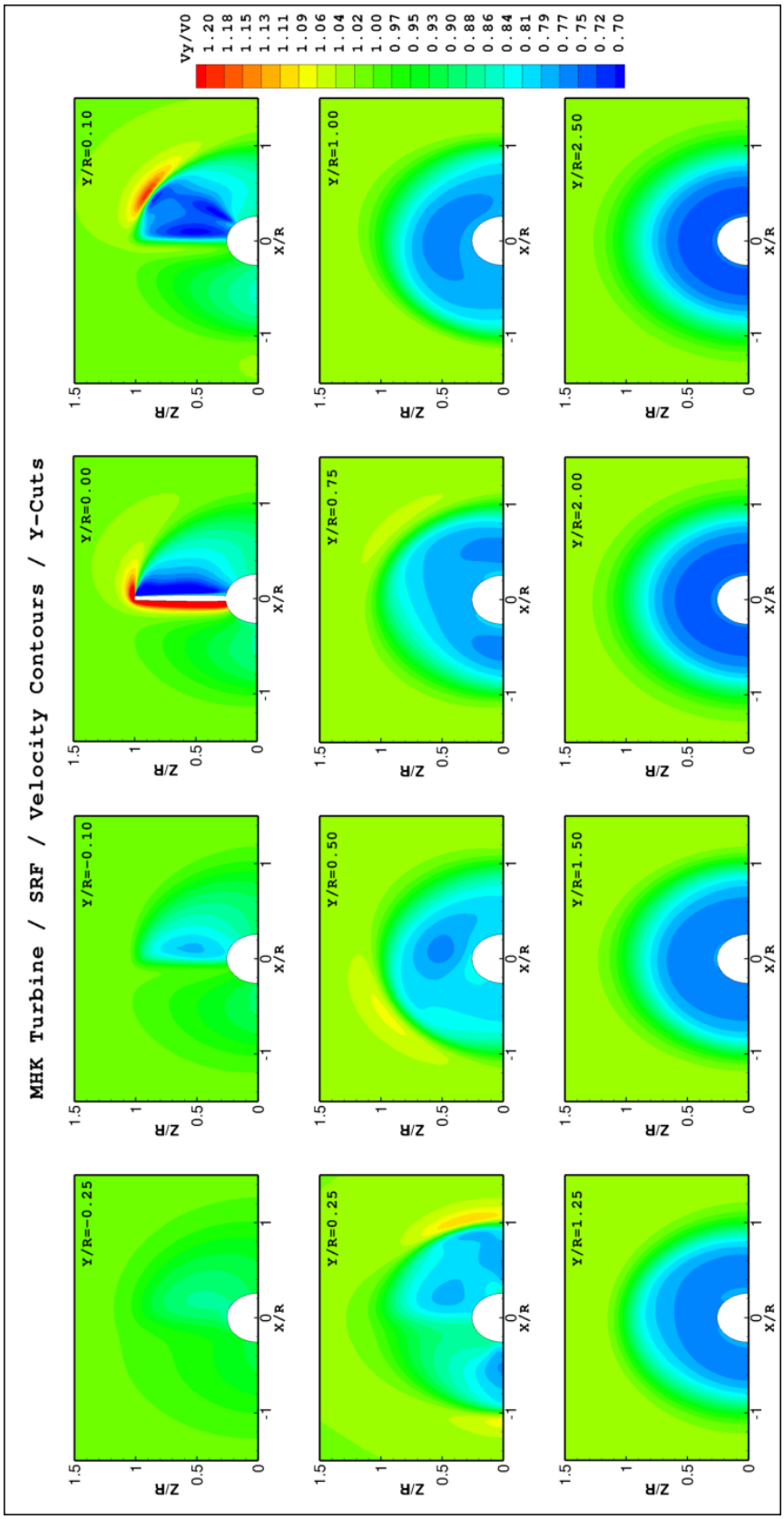

Figure 4.8: Normalized velocity contours on Y-cuts plane along a tidal channel.

4.2.3 Results

Figure 4.9 shows the results form the application of the SRF, VBM and ADM models to study the fluid mechanics of the flow around an MHK turbine in a tidal channel. We observe the same qualitative features found in the validation runs. The blade tip vortex signature in the SRF, the crown type signature at the edge of the rotor disk for the VBM, the smooth profile after $\frac{Y}{R} > 5$ in the results from SRF and VBM, the more realistic momentum deficit near the hub for SRF as compared to VBM and the lack of ability in ADM to accurately estimate the velocity deficit in the turbulent wake of the device with the idealized boundary conditions in comparison to the SRF model and VBM.

Comparison between the SRF results for a MHK turbine (figure 4.9) with the results from the validation runs for the NREL Phase VI wind turbine (figure 3.15), shows the vortices shed from tip of the MHK turbine blade travel longer distance (i.e. about 2 radii downstream) than the corresponding vortices shed from tip of the wind turbine blade (i.e. less than 1.5 radii downstream). The physics behind this difference is that in the case of MHK turbine the lower value of the kinematic viscosity of the fluid (i.e. water) results to a higher Reynolds number for the flow, which leads to slower vorticity diffusion. Therefore, the signature of the tip vortices for the case of MHK turbine is visible at a larger distance downstream. Another interesting point from comparisons of these two sets of results is the smoother velocity profile just behind the MHK turbine at $\frac{Y}{R} = 5$.

The difference between the vortex shedding signature at the blade tip is also valid in the results from VBM. Comparing results from VBM for MHK and NREL phase VI wind turbine, the crown type signature, showing the tip vortices, is longer and extends more than 1 radii downstream of the MHK turbine blade further than in the results from NREL Phase VI turbine according to the same physics of slower vorticity

diffusion due to higher Reynolds number (associated, among other variables, with the higher kinematic viscosity of water than air.)

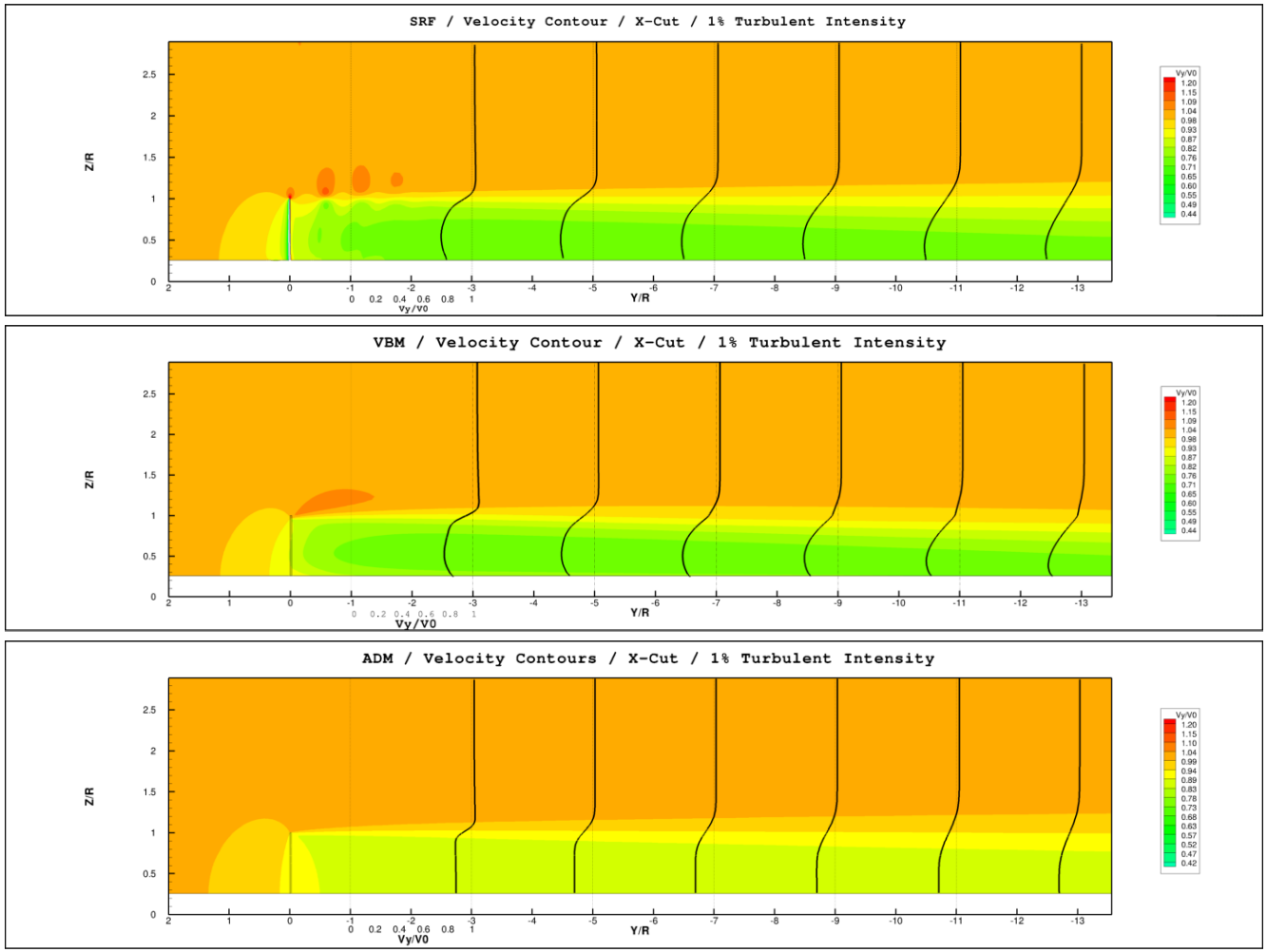

Figure 4.9: Velocity contour of simulated flow around a MHK turbine at $\frac{Y}{R} = 0$ with SRF, VBM and ADM .

In order to have better comparisons between the modeled velocity deficits by each of the three models (i.e. SRF, VBM and ADM), the corresponding simulated velocity profiles on each $y-z$ planes along the tidal channel are superimposed on top of each other, as shown in figure 4.10. Figure 4.10 shows that the ADM is underestimating the velocity deficit along the channel in comparison to the SRF model and VBM with current idealized boundary conditions. However, the simulated velocity deficit from SRF and VBM show very good agreement. For the velocity profiles at the first three cross sections downstream of the turbine, modeled with SRF and VBM, the main disagreement is close to the root of the blade where flow separation occurs. Since VBM is averaging the effect of the turbine blade on the flow, it is underestimating the deficit. Moving further downstream along the tidal channel, disagreement of the modeled velocity profiles from SRF and VBM happens at the region close to the blade tip. Again, since the fluid mechanics of the flow is not being accurately modeled at the blade tip using VBM, the simulated deficit is a little off and is in a good agreement with the simulated deficit with the ADM. Despite these small differences between the modeled velocity deficit from SRF and VBM, it can be stated that VBM is doing a good job modeling the turbine wake considering the degree of simplification and decrease of computational cost and time, which has been addressed earlier in chapters 2 and 3.

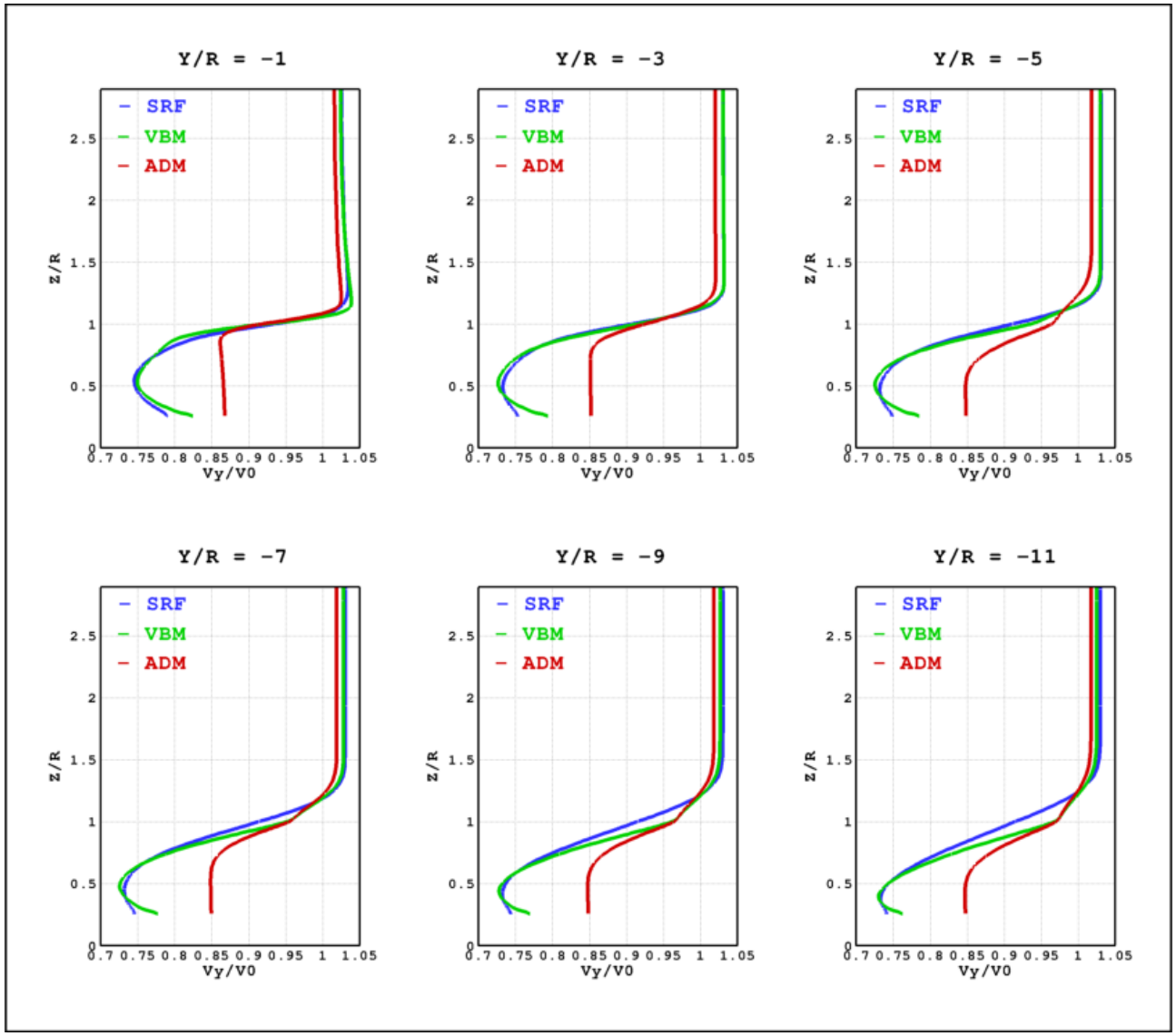

Figure 4.10: Superimposed simulated velocity deficits from SRF, VBM and ADM models on X-cut planes along a tidal channel.

In order to have another confirmation regarding a successful process of applying our developed numerical methodology for study of MHK turbines, we looked at the limited streamlines along the MHK turbine blade and compared it with results from validation runs for wind turbine blade span. As it was showed in table 4.2, and discussed in depth in subsection 4.2.1, the values for the rotor tip speed and angle of attack along the blade were being calculated in order to avoid cavitation at the tip and flow separation along the blade. Based on these calculations, we set the free stream and angular velocities of 2 $[\frac{m}{s}]$ and 17 $[rpm]$ respectively, so the magnitude of the rotor tip speed is below the critical value and therefore cavitation will be avoided. Figure 4.11 shows, the streamlines along the suction side of the turbine blade and contours of the pressure.

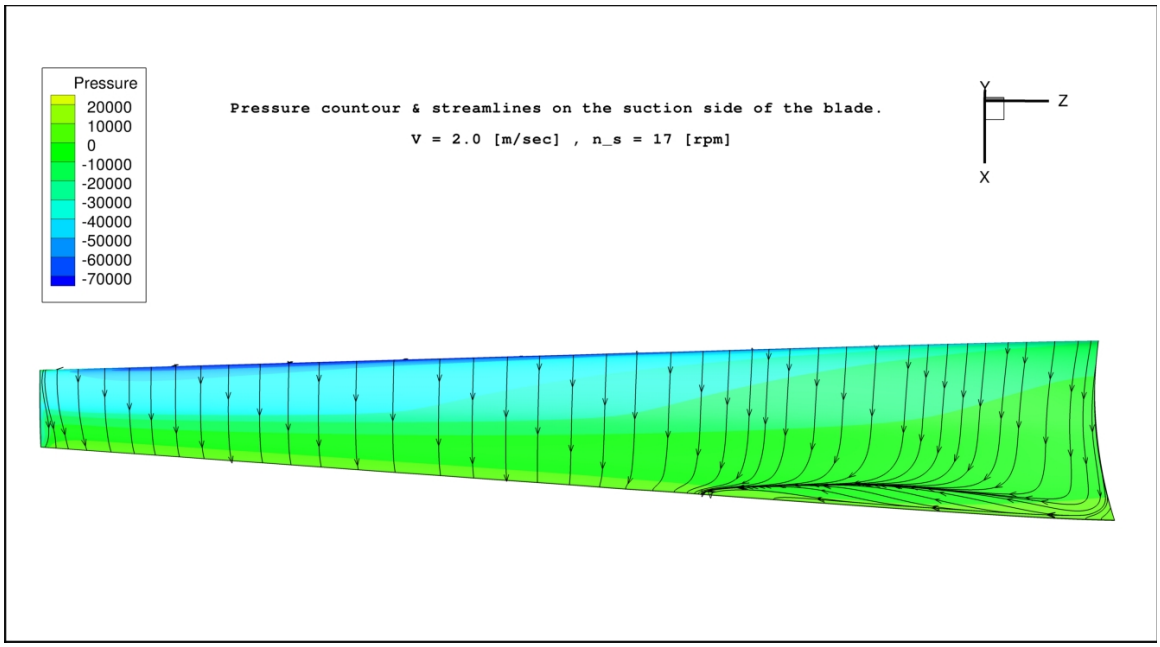

Figure 4.11: Limited streamlines on top of the pressure contours, along the suction side of a MHK turbine blade with Tip Speed Ratio (TSR) of 4.92 modeled with SRF.

This result confirms the low values of the relative negative pressure, with a maximum of 70$[kPa]$ (compared to 300$[kPa]$ hydrostatic pressure for a 20$[m]$ depth at the blade tip), except for a small separated region on the trailing edge at the root. It should be noted that the preliminary calculations predicted a maximum angle of attack of 18 °at this configuration which would lead to significant separation (see table 4.2.1). The actual angle of attack is approximately in the range of $6 < \alpha < 8.5$. This shows that the preliminary calculations significantly overpredicts the angle of attack based on the free stream and angular velocities. It is important to take this into account when choosing operating conditions to extract the maximum power possible while keeping separation and cavitation under control.

Figure 4.12 shows the limited streamlines along the blade of the NREL Phase VI wind turbine from the validation runs. As it can be seen the pressure contours are very similar to the one showed in figure 4.11, but the pressure magnitudes are very different. In the case of the NREL Phase VI wind turbine, flow separation happens near the root of the blade as well, but its location is in the middle section of the root, in comparison with the case of MHK turbine which is closer to the trailing edge of the blade at the root.

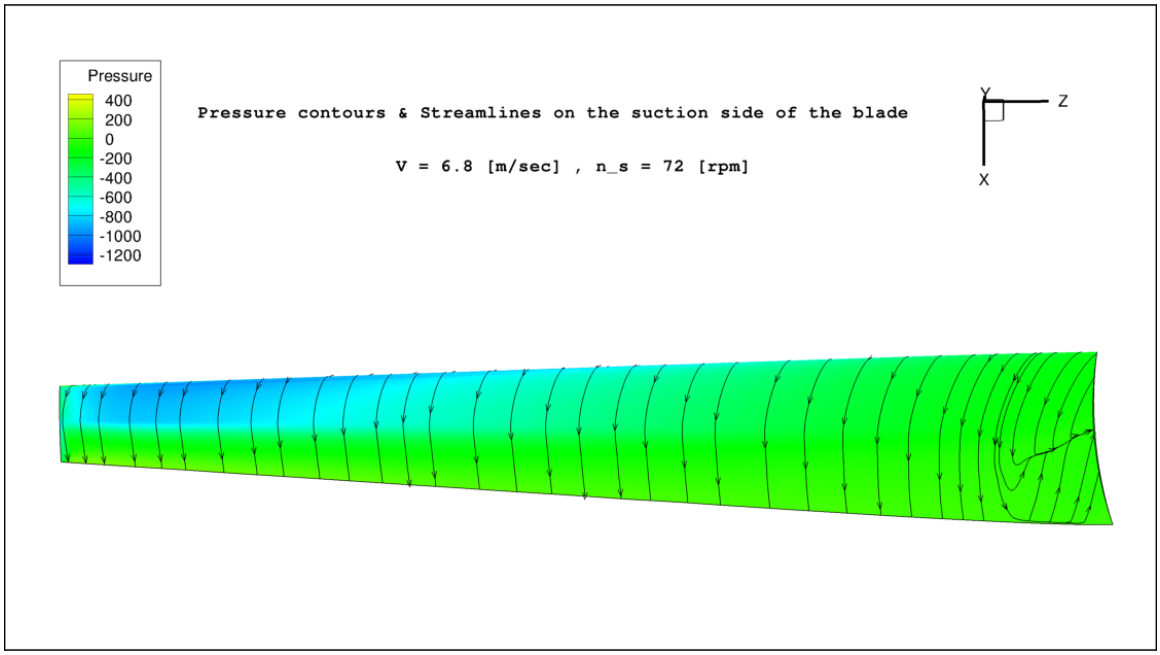

Figure 4.12: Limited streamlines on top of the pressure contours, along the suction side of the NREL Phase VI wind turbine blade with Tip Speed Ratio (TSR) of 6.13 modeled with SRF.

4.2.4 Results from MHK turbine modeling with more realistic boundary conditions

So far, most of the results for both the validation runs for modeling the wind turbine and application runs for simulating flow around a MHK turbine were based on the idealized boundary conditions of NREL experiments. However, now that we are trying to approach the most realistic boundary conditions for modeling a MHK turbine, the idealized boundary conditions need to be modified as well.

One of these boundary conditions need to be modified is the value of the turbulent intensity in the domain. Turbulence intensity is defined as the ratio of Root-Mean-Square (RMS) of turbulent velocity fluctuations to the mean velocity of the flow as

$$I = \frac{\sqrt{< u'^2 >}}{< u >}, \tag{4.4}$$

where the brackets indicate an ensemble averaged value of the variables.

For the previous runs (both validation runs and MHK application runs), the value of turbulent intensity at the inlet of the channel was set to be equal to 1%. This value corresponds to a well-designed wind tunnel, such as NASA Ames wind tunnel used in NREL experiment. However, based on field measurement, it has been shown that the value for turbulent intensity for tidal power applications is closer to 10% [33].

Figure 4.13 shows the velocity contours on a $x - z$ plane along the tidal channel with 10% turbulent intensity at the channel's inlet. Since the increment of turbulent intensity in the free stream leads to a higher turbulence level in the flow, the mixing and diffusion processes within the flow increase.

As it is showed in figure 4.13 for the cases with higher value of turbulent intensity, the turbulent wake of the MHK turbine decays faster downstream of the tidal channel in comparison to the results with 1% turbulent intensity (see figure 4.9). This goes back to the fact that the magnitude of the turbulent velocity fluctuations is larger and diffusion is enhanced in the flow. As a result, the simulated velocity deficit in the turbulent wake decays faster, such that about 10 radii downstream of the channel, the magnitude of the velocity deficit decreases significantly and the velocity profiles gets closed to a monotonically increasing profile shape in the far wake region with a very sharp slope. Another significant difference between the results with 10% turbulent intensity in comparison to the 1% is the faster diffusion of the vortices shed from the tip of the blade. In case of 1% turbulent intensity two helical vortices shed from tip of each blade, propagate about 2 radii downstream of the blades without loosing coherency. This is observed as 4 discrete dark red circles close to the tip of the blade (see figure 4.9). However, since increasing the value of the turbulent intensity to 10%

enhances the diffusion in the flow field, two mentioned helical vortices propagate only about 1 radii downstream, after which they loose coherency and dissipated in the flow. This is observed as only 2 discrete dark red circles, showing high speed regions, near to the tip of the blades (see figure 4.13).

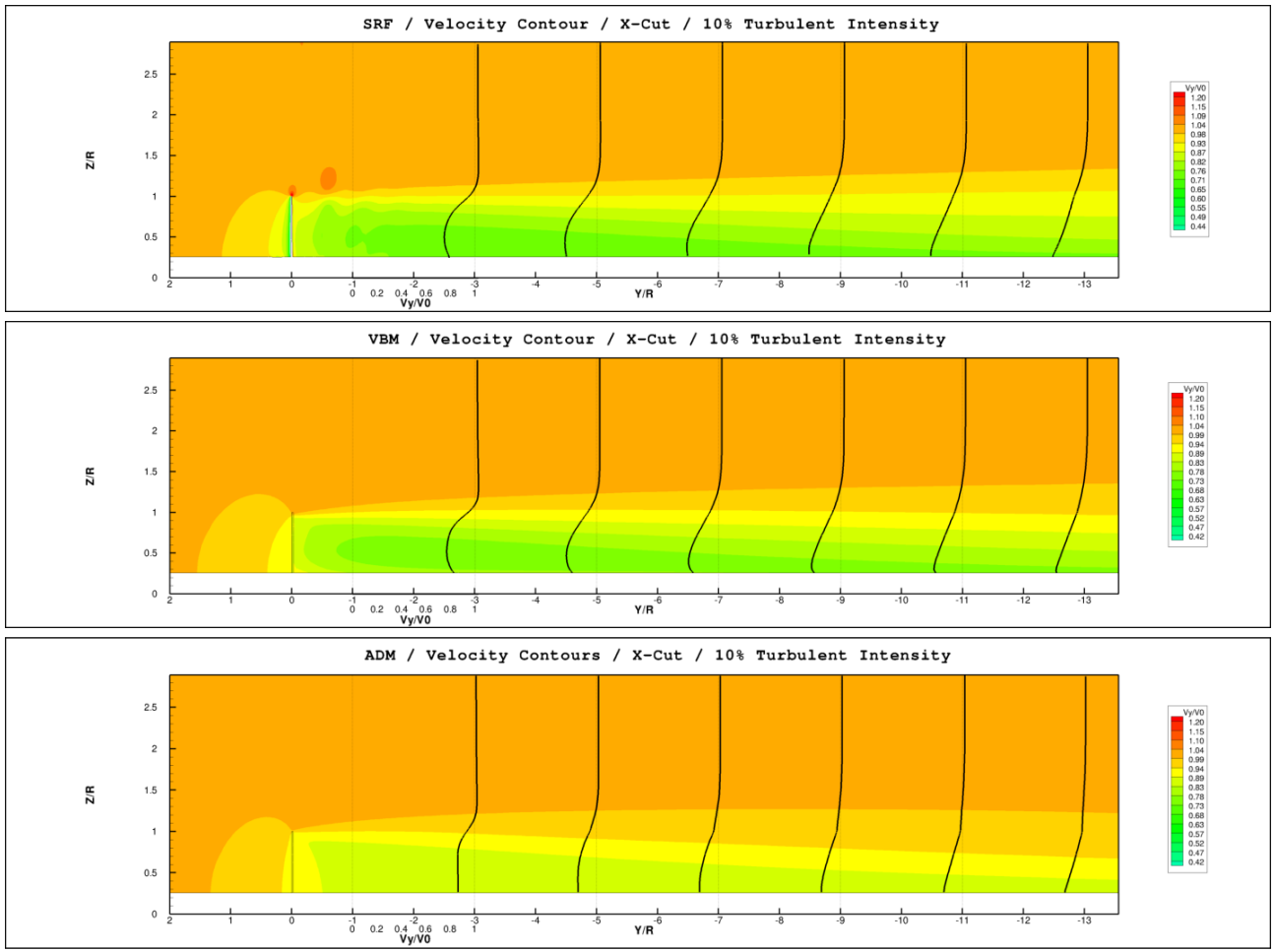

Figure 4.13: Velocity contour of simulated flow around a MHK turbine with turbulent intensity of 10% .

The increased value of the turbulent intensity at the inlet of the channel led to a better agreement in the modeled velocity deficit downstream of the channel via ADM in comparison to the corresponding velocity deficits modeled by SRF and VBM. This also led to a better agreement between the simulated velocity deficit from SRF and VBM close to the end of channel in comparison to the case of 1% turbulent intensity (see figure 4.10. In order to have a more detailed comparison between the modeled velocity profiles on each $y - z$ plane along the tidal channel from SRF, VBM and ADM, they are superimposed in one figure on the same coordinate as shown in figure 4.14 (similar to the comparison made for the case with 1% turbulent intensity).

This result shows that, after about 3 radii downstream of the device, the skewed shape of the simulated velocity profile from the ADM evolve to a more smooth shape, closer to a Gaussian profile. However, ADM still underestimates the value of the deficit in comparison with SRF and VBM. Moving further downstream, the shape of the velocity profile from ADM becomes closer to the one from SRF and VBM. This looks more promising compared to the skewed shape profile all along the channel with 1% turbulent intensity. Therefore, the ADM can be applied for simulating the flow field in an array of multiple turbines, taking advantage of its minimum computational time requirements.

Comparing figures 4.10 and 4.14 for 1% and 10% turbulent intensity, it can be seen that the difference between the modeled velocity deficits from SRF and VBM decreases by increasing the turbulent intensity magnitude. This is associated to the higher diffusivity in the flow. Thus, for more realistic conditions for tidal flows, SRF, VBM and ADM results are in better agreement with each other.

These results show that the process of applying the validated methodology against experimental data of the NREL Phase VI turbine was successful. For the same turbine blade geometry, results are very similar to the previous ones although some

minor differences have been observed. However, the current geometry and blade specifications of the NREL Phase VI turbine doesn't allow us to have higher free stream velocity at the inlet and higher angular velocity. Therefore, blade redesign needs to be implemented in order to explore a wide range of operating conditions representative of MHK applications (Reynolds numbers and Tip Speed Ratios). The flexibility of VBM for imposing different boundary conditions offers the opportunity to start the study of potential environmental effects of MHK turbines. In the next subsection, and more extensively on chapter 5, several potential environmental effects of the MHK turbines in tidal channels will be described.

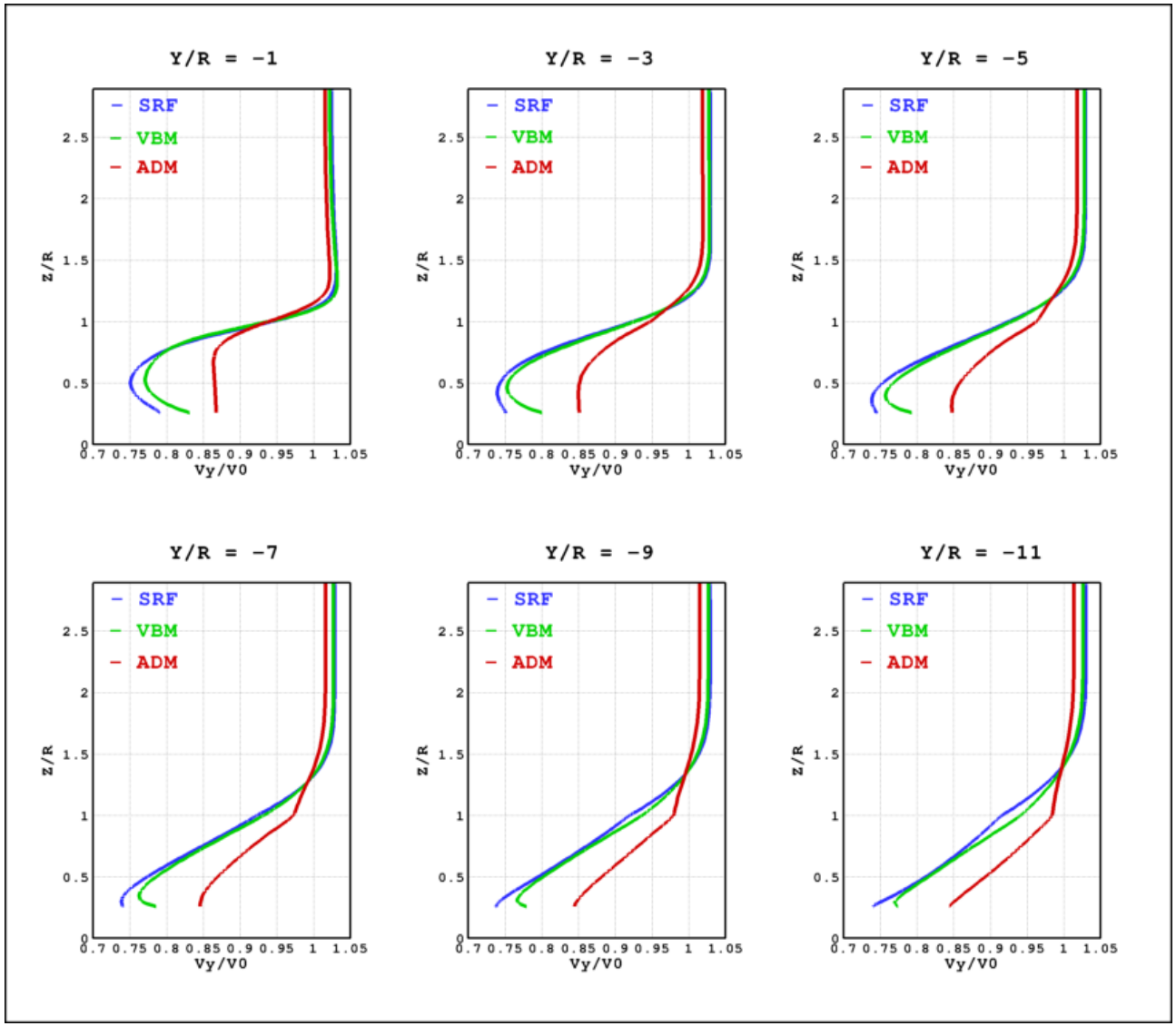

Figure 4.14: Superimposed simulated velocity deficits from SRF, VBM and ADM models on X-cut planes along a tidal channel with 10% turbulent intensity.

4.3 Application of the Virtual Blade Model (VBM) with Modified Computational Domain to Study the Potential Environmental Impacts of a MHK Turbine.

As explained above in subsection 2.2.2, the VBM simulates the effect of turbine blades on the flow via a circular disk with an area equivalent to the swept area of the turbine and some information about the performance of the blades as an input. The absence of the actual geometry of the blade in VBM and not having a rotating reference frame makes this model capable of using realistic boundary conditions in its computational domain. This is just the opposite to the SRF model, which is limited by rotationally symmetric boundary conditions in its domain (see subsection 2.1.2). Therefore, different boundary conditions can be applied on the VBM computational domain.

The secondary research goal of this thesis, after developing a methodology to model the Marin Hydrokinetic (MHK) turbines, is to study potential environmental effects of MHK turbines, such as the effect of the sudden pressure fluctuation across the turbine blades on small marine species or sedimentation of suspended particles in a tidal channel using the developed and validated numerical models. Modeling the bottom effect of the channel would give the opportunity of having realistic velocity profiles at the inlet of channel (i.e. turbulent boundary layer velocity profile instead of uniform profile) and also the possibility of studying the sedimentation of suspended particles, that interact with the turbulent wake of the turbine. Therefore, modeling the bottom effect becomes necessary for future studies and we started to work with VBM domain to model this effect, since this modeling is not possible with the SRF model limitations. However, since SRF captures the detail of the flow field right after and before the blade, it can be used for study the effect of pressure spike across the blade on small marine species. It should be noted that this type of study can not

be done via VBM, since it does not capture the details of the flow in the near wake region.

In order to be able to model the channel's bottom effect and imposing different boundary conditions on the channel walls, we use a more realistic channel geometry with a square cross section, unlike the cylindrical domain used for SRF. There are 4 distinct lateral surfaces to apply the appropriate boundary conditions. For example, we can apply a no-slip condition on bottom, impose a given mean velocity profile on the side walls and mimic the free surface on the top with a no stress condition. Figure 4.15 shows the computational domain for VBM. It should be noted that for future comparisons purposes with the SRF results area was kept the same so that the blockage effect of turbine, seen as a small increase in the free stream velocity around the turbine as compared to the inlet, is similarly represented.

Figure **??** shows results from a VBM simulation of a MHK turbine in a rectangular channel. Note that the hub section here is not a hollow cylinder along the channel as it was in the SRF. It has been set to be a fluid zone, hence flow acceleration is being observed at the hub section of the turbine, due to the reduction in cross section. Currently, we are working on a more realistic way of modeling the hub section, by either calculating the drag coefficients for that section of the blade via a higher fidelity numerical model or finding an accurate approximation for the hub using the Actuator Disk Model, so that a reasonable physical velocity deficit will occur in the near wake region behind the hub section.

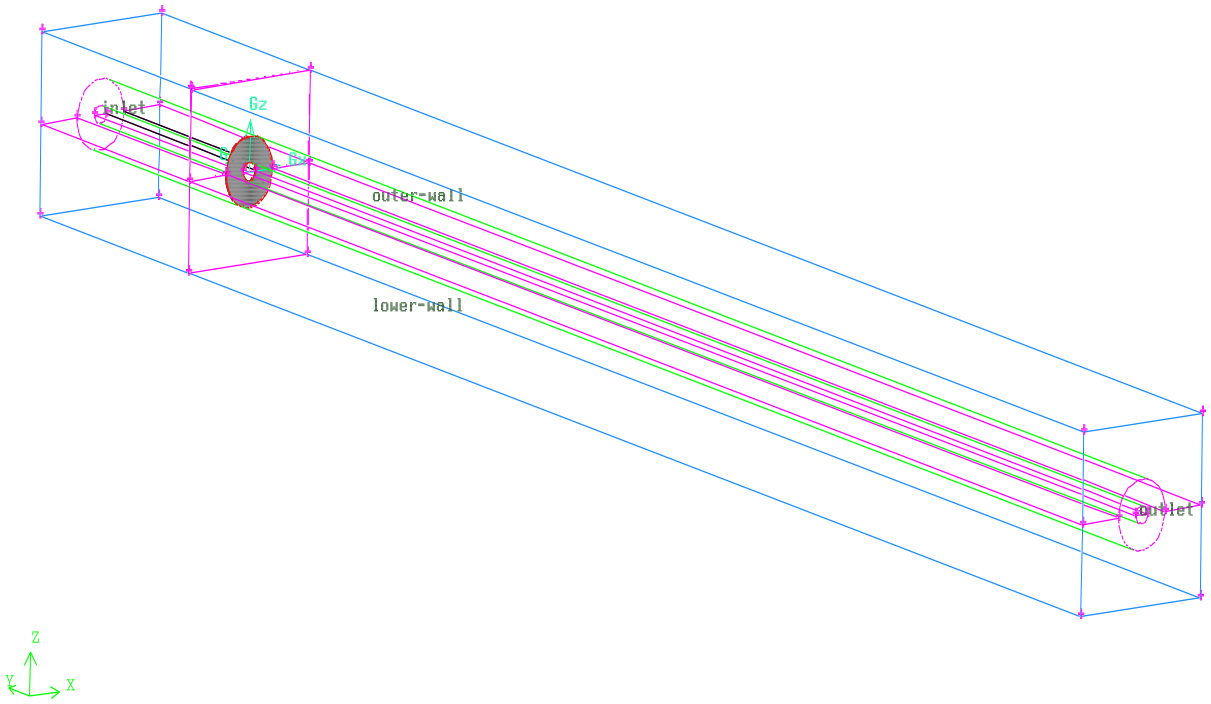

Figure 4.15: Flow domain in the application of the VBM model to the simulation of Marine Hydrokinetic (MHK) turbine in a tidal channel.

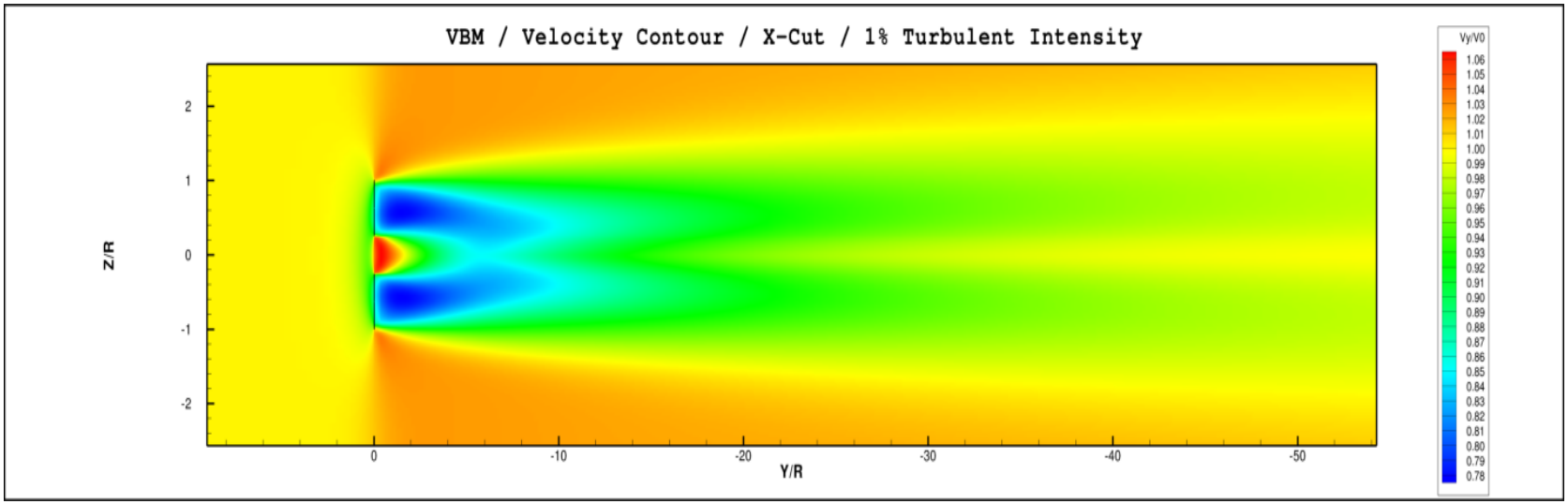

Figure 4.16: Superposition of velocity profiles from SRF model in black and VBM in blue on top of the velocity contour from VBM.

Chapter 5

NUMERICAL MODELING OF THE POTENTIAL ENVIRONMENTAL EFFECTS OF MARINE HYDROKINETIC (MHK) TURBINES

At this stage, a hierarchy of numerical models to simulate the flow field around and in the turbulent wake behind an MHK turbine has been developed. The converged flow field solution from these numerical models will provide the values of different physical variables (i.e. velocity components, pressure, turbulent properties and etc.) within the flow. This makes it possible to model the potential environmental effects of a MHK turbine, such as interaction of the device with small marine species in a tidal channel or settling process of suspended particles affected by the turbulent wake of the device in the flow. However, it should be noted that the availability of an accurate estimate for different variables in the flow field strongly depends on the fidelity of the numerical model. Thus, the capabilities of each model for simulating the potential environmental effects should be addressed and investigated.

The two potential environmental effects studied here are the influence of sudden pressure fluctuation across the turbine blade on small marine species and the influence of the momentum deficit in the turbulent wake on the sedimentation process of suspended particles in the flow. Pressure fluctuation across turbine blades and in blade tip vortices can damage internal organs of marine species as they swim through the device. In addition, the velocity deficit in the turbulent wake of the turbine might enhance the sedimentation process of suspended particles in a tidal channel and lead to deposition into artificial patterns that alter the benthic ecosystem just downstream

of the turbines. These are just two examples of potential environmental effects of MHK turbines that need to be addressed and investigated a priori before large scale deployment can be proposed and permitted.

In this chapter, results from small buoyant particles, representing juvenile fish, and small heavy particles sedimenting in the flow, are presented. For the slightly buoyant particles, the pressure history will be studied statistically with particular attention to the high magnitude of the pressure fluctuations occurring over short periods of time. These high impulse conditions are correlated with damage thresholds obtained from laboratory experiments from the literature. For the sedimentation of suspended particles, the settling velocity and terminal location of particles on the bottom of the tidal channel will be compared with the simulated flow in the channel without any turbines. This allow us to establish the potential for effects of MHK turbines wake on sedimentation of suspended particles in a tidal channel

5.1 Modeling interaction between flow and particles in a tidal channel

Suspended particles in the ocean and tidal channels are just one example of particle-laden turbulent flows. Given the wide range of application of this type of flow, understanding the underlying physics and how the carrier flow and the particles interact with each other has become a field of interest for scientists and engineers.

Study of particle-laden turbulent flows can be done either by an Eulerian-Eulerian or Eulerian-Lagrangian approach. In the first one, both the carrier flow and the particles will be modeled as two separate continuous phases, and conservation equations are solved for both of them. In the second approach, the carrier flow is the continuous phase, but the particles will be considered individually and simulated with the equation of motion for each discrete particle. The best way to study the particles used to model the fish and sediment in the flow is to consider them as Lagrangian tracers. The volume fraction of particles (both fish and sediment) in the flow is very low (less than 10^{-6}) and therefore the particle-fluid and particle-particle interactions are negligible. This application is therefore a perfect candidate for study with the Eulerian-Lagrangian formulation.

The physical description of the flow (i.e. size and volume fraction of particles in the flow) is the key point that sets the most important interactions between carrier flow and particles to study. For example, in a turbulent flow with small particle size and volume fraction, the most important interaction would be the one that the carrier flow has on particles (one-way coupling) and other interactions can be neglected. However, if the volume fraction increases, then the effect of particles on the flow and sometimes even on each other might become important too (two and four-way coupling).

Based on our assumptions and the geometry of the tidal channel, which will be discussed in detail later in this chapter, and using the diagram suggested by Elghobashi in 1991 [27], the most important interactions between the carrier flow and the particles

used to model the sediment and juvenile fish can be identified from figure 5.1.

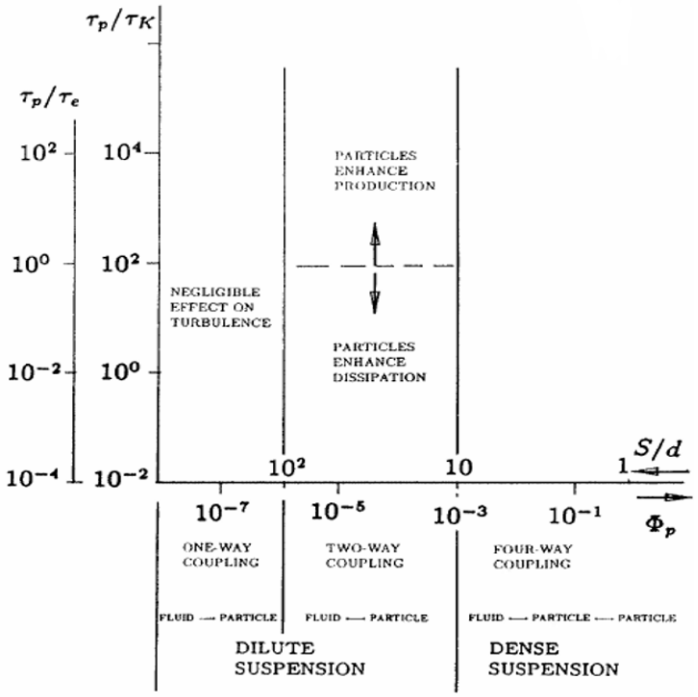

Figure 5.1: Map of regimes of interaction between particles and turbulence.

Φ_p : volume fraction of particles, $\Phi_p = MV_p/V$

M : number of particles

V_p : volume of a single particle

V : volume occupied by particles and fluid

d : diameter of particle

τ_p : particle response time $= \rho_p d^2/(18\rho_f \nu)$ for Stokes flow

τ_k : Kolmogorov time scale $= (\nu/\epsilon)^{1/2}$

τ_e : turnover time of large eddy $= l/u$

This diagram shows the non-dimensional response time of particles (Stokes number) versus their volume fraction in the flow. As it is shown in figure 5.1, for higher volume fraction, as the number of particles increases in the flow, their effect on the flow becomes more complex (2-way coupling). Increasing the volume fraction even further leads to an interparticle distance that results in the particles affecting the motion of the surrounding particles (4-way coupling). In the later sections of this chapter, figure 5.1 is used based on the specification of the geometry to characterize the most important interactions to study.

5.2 *Modeling the Effect of Sudden Pressure Fluctuation on Small Marine Species Across a MHK Turbine Blade*

The existence of a sudden pressure fluctuation across the turbine blades has been addressed in the theory section of the actuator disk model (ADM) in detail (section 2.3.2). Based on the magnitude and time duration of this sudden pressure fluctuation, internal organs of small marine species might be damaged or they even might be killed during the exposure to this sudden fluctuation (figure 5.2). It should be noted that we are addressing this physical phenomena as a potential environmental effect of MHK turbines, therefore more investigations need to be done, in order to make solid conclusions.

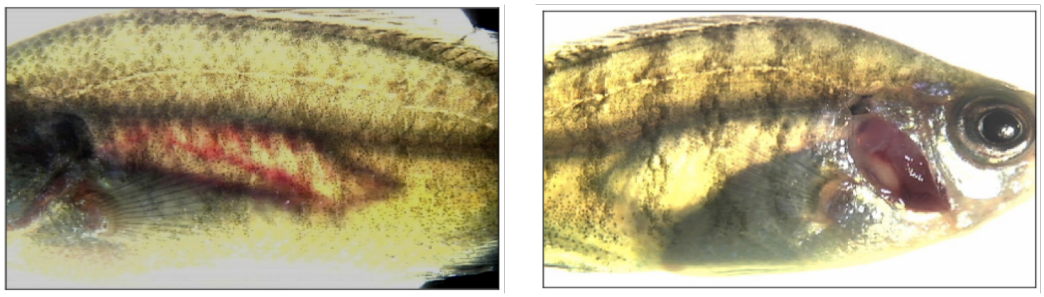

(a) (b)

Figure 5.2: External view of internal hemrrhages (a) and non-hemorrhaged (b) juvenile bluegill [34].

Among the available numerical models in our methodology, SRF captures the instantaneous details of the flow across the turbine blade. Therefore, the pressure history on particles can be accurately modeled with this model. Since VBM or ADM average the blade effects on the flow, they will not be suitable for this modeling purpose. Here, a number of buoyant particles, modeling juvenile fish, will be injected at the inlet of the SRF domain. The pressure history along their trajectories will be studied

statistically with particular attention to the high magnitude of pressure fluctuations occurring over short periods of time. These high impulse conditions are correlated with damage thresholds obtained from laboratory experiments in the literature to analyze the severity of the interaction between MHK turbines and small marine species.

5.2.1 Numerical Modeling Theory

Discrete Phase Model (DPM) is the numerical model used to simulate these multiphase flows in ANSYS FLUENT. This model is based on the Eulerian-Lagrangian approach. A fundamental assumption made in this model is that the dispersed second phase occupies a low volume fraction. The particle trajectories are predicted by integrating the force balance on the particle, which is written in a Lagrangian reference frame, following each particle. This force balance equates the particle inertia with the forces acting on the particle in x direction as

$$\frac{du_p}{dt} = F_D(u - u_p) + \frac{g_x(\rho_p - \rho)}{\rho_p} + F_x, \tag{5.1}$$

where the variables with the "p" subscript refer to the particle variables and those without subscript refer to the variables of the carrier flow. Here u is the velocity, ρ is the density and g_x is the gravitational constant in the specified direction.

In this equation, the first term on the right hand side of the equation is the drag force per unit particle mass, the second one is the gravitational force in the specified direction and the third term is an additional force term that can be defined based on additional physical forces in the flow (i.e. Saffman's lift force, Brownian force and etc.). In this model, the shape of the particles is assumed to be spherical, therefore the drag force F_D will be computed by

$$F_D = \frac{18\mu}{\rho_p {d_p}^2} \frac{C_d Re}{24}, \tag{5.2}$$

where d_p is the particle diameter, C_d and Re are the drag coefficient and relative Reynolds number respectively. These are defined as

$$Re \equiv \frac{\rho d_p |u_p - u|}{\mu}, \tag{5.3}$$

$$C_d = a_1 + \frac{a_2}{Re} + \frac{a_3}{Re^2}, \tag{5.4}$$

where a_1, a_2, and a_3 are constants that apply over several ranges of Reynolds number given by Morsi and Alexander, 1972 [35].

DPM models the particle path in the flow, using the mean velocities of the fluid and the particulate phase at each cell integrating the force balance equation. Since the flow inside the channel is already converged from the previous simulations, the pressure history of the particle along its path can be interpolated. In the next section, the details of the injection method for buoyant particles is explained and the results from this modeling presented.

5.2.2 Assumptions

Juvenile fish are modeled as slightly buoyant spherical particles. The density ratio of these particles with respect to water is considered to be 0.95 and their diameter is $5[mm]$. These values of density ratio and size of particles were chosen based on the literature to represent small marine species swimming in water. These particles are being injected at the inlet of the channel from a 5 by 10 grid at different points with respect to the MHK turbine blade as shown in figure 5.3. This injection grid provides various particles paths through turbine blade with various horizontal and vertical distances from the blade. Therefore, the covered area around the device is wide enough, so that the most critical places that pressure fluctuation can lead to serious damages for the small marine species are investigated.

Based on the above assumptions for the number and size of the particles, the volume fraction, Φ_p, is estimated to be very small (order of 10^{-11}). This value confirms the use of one-way coupling in the simulation and the neglect of any influence of the particle dynamics on the flow (2-way coupling) or on each other (4-way coupling), see figure 5.1.

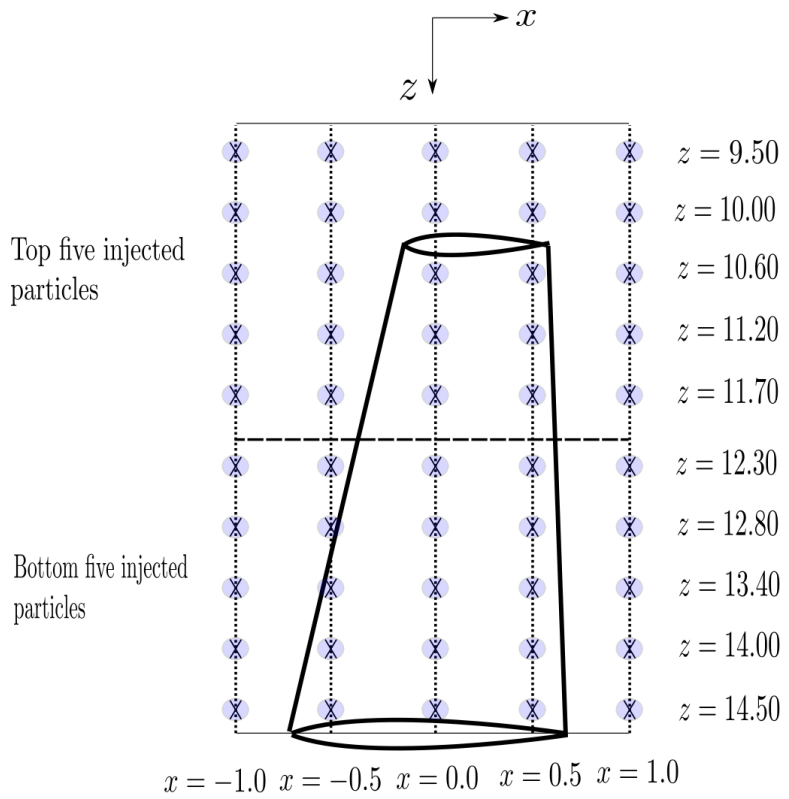

Figure 5.3: Injection plane at the inlet of SRF domain. 10 Particles are equally distributed along each injection rake. The reference height is assumed to be at the free surface of the tidal channel with 16[m] depth (all dimensions are in meters [m]).

5.2.3 Results

We analyze the effect of the the flow around the turbine on the pressure sensed by the particles, acting as fish surrogates, as they traverse the turbine disk. To analyze this phenomenon, we will decompose the pressure into three components that can be described separately. First, we identify the static pressure, which is associated with the state of the fluid. Second is the dynamic pressure that is a result of fluid motion. This quantity is defined based on the density and fluid velocity as

$$P_{dynamic} = \frac{1}{2}\rho V^2, \tag{5.5}$$

Usually the summation of these two pressure forms, static and dynamic, is called the total pressure. Therefore, the effect of these two forms is addressed as the effect of total pressure. The total pressure is defined as

$$P_{total} = P_{static} + P_{dynamic}. \tag{5.6}$$

The last component of pressure is the hydrostatic pressure. This component, which is part of the static pressure, is exerted by the weight of the fluid due to gravity and depend on the height of the fluid column above the particles. Considering that the reference height is the free surface of water, the hydrostatic pressure in the fluid will vary based on the following relation:

$$P_{hydrostatic} = \rho g z. \tag{5.7}$$

The effect of the sudden pressure fluctuation through the MHK turbine blade was only observed on the particles being injected from the centerline rake located at $x = 0.0$ and the first rake on its left with -0.5 [m] offset at the inlet of the channel (see figure 5.3). Particles that have been injected from rakes with 1.0 [m] offset on right and left hand side of the centerline rake at the inlet located at $x = 1.0$ and $x = -1.0$ respectively (see figure 5.3), pass the turbine blade with a fairly large horizontal offset. Therefore, the pressure fluctuation effect could not be observed in pressure history of those particles anymore. Three of the bottom particles that were injected from the rake at $x = 0.5$ on the right hand side of centerline rake (see figure 5.3), hit the blade wall and after that the path of those particles can not be modeled further. This is associated to the limitations of the Single Reference Frame model with absolute particle tracking. Use of this model to study blade strike is being further investigated based on this preliminary results.

Results of injected particles from the centerline rake located in $x = 0.0[m]$ *at the inlet of the channel.*

Figure 5.4 shows the static (including hydrostatic) pressure on the particles injected from the centerline rake located in $x = 0.0$ at the inlet, versus the normalized length of the tidal channel. The reference pressure here is 101.3 [kPa] at the reference height, $z = 0$, which is the top of our computational domain. Positive z-axis points downward to the bottom of the computational domain. The particles that are injected at lower levels experience higher hydrostatic pressure. Since the particles are slightly buoyant, right after being injected they start to rise up along in the tidal channel, thus their hydrostatic pressure will decrease linearly along their trajectories.

The most interesting point of the pressure history of particles is the sudden pressure fluctuation that the particles experience around the location of the blade at $\frac{Y}{R} = 0$.

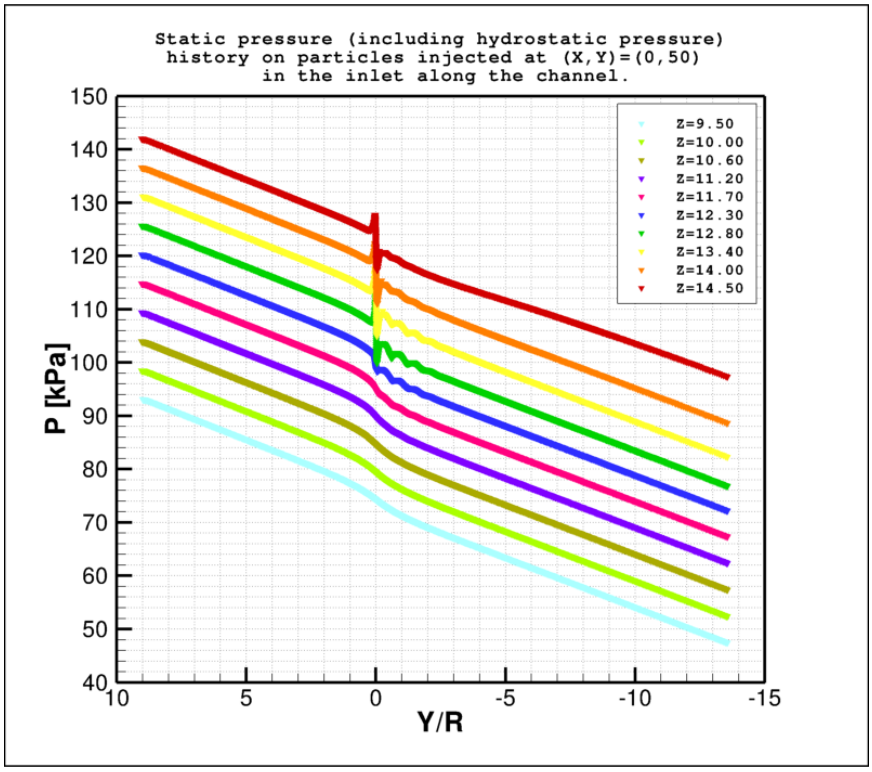

Figure 5.4: Pressure history on particles injected from centerline rake at $x = 0.0$ on the inlet versus the normalized length of the tidal channel.

Since the hydrostatic pressure decreases linearly and particles height does not change dramatically through the blade, the observed spike is a result of sudden changes in the static pressure due to the flow acceleration. Right before and after the MHK turbine blade, the state and velocity of the fluid changes rapidly and this lead to sudden fluctuations of the pressure.

Beside the value of the pressure at the peak and trough, the time duration as experienced by the fish moving through the turbine blade is important. Figure 5.5 shows the variation of the static pressure on each injection versus the particle residence time. The sudden pressure fluctuation starting from top of the spike to its bottom, happens

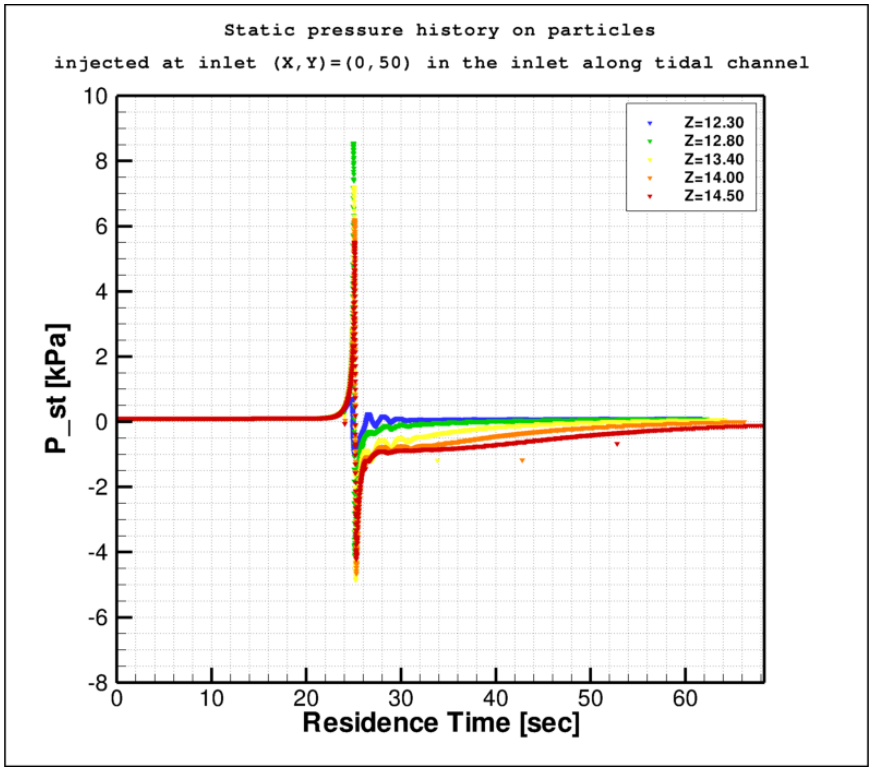

Figure 5.5: Pressure history on particles injected from rake at $x = 0$ at the inlet versus residence time.

in less than 0.2 seconds. Having the specific data, the ratio of pressure fluctuation to time ($\frac{\Delta P}{\Delta t}$) for each particle can be compared to the threshold values from PNNL experiments [34].

Figure 5.6 shows the particles injected from the rake to the left of the centerline, located in $x = -0.5\ [m]$ at the inlet of the channel. These results do not show the pressure spike at the location of the blade $\frac{Y}{R} = 0$ found in previous results. This is due to the larger horizontal distance to the particles from the tip of the turbine blade. The disappearance of the pressure spike was observed in injections from other rakes due to their larger horizontal and vertical distance from the span and the tip of the

blade respectively.

Figure 5.7 shows the total pressure history of five injections at bottom of the same rake versus channel length. Comparing this with figure 5.5, it is observed that the pressure difference experienced by particles decreased by about a factor of 4. Although the effect of tip vortices is still appreciable and a small spike exists at $\frac{Y}{R} = 0$, the magnitude of this fluctuation is small.

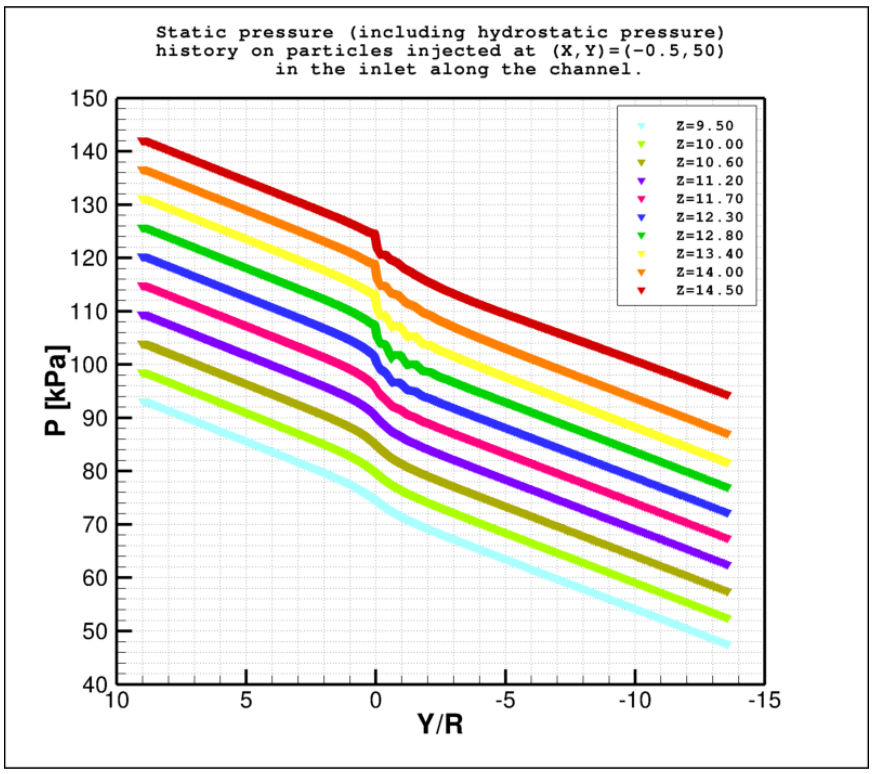

Figure 5.6: Pressure history on particles injected from rake at $x = -0.5$ at the inlet along the tidal channel.

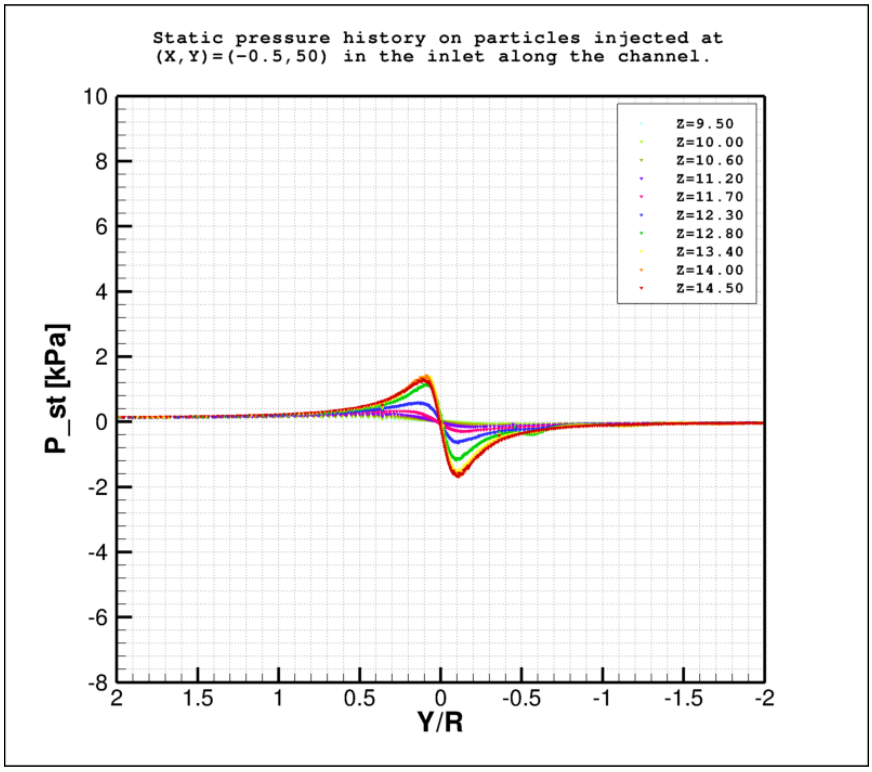

Figure 5.7: Pressure history on particles injected from rake at $x = -0.5$ at the inlet versus residence time.

Comparison between Pacific Northwest National Laboratory (PNNL) thresholds and results from these simulations

PNNL has investigated the response of fall chinook salmon and bluegill sunfish to a rapid pressure change in an experiment conducted in their laboratory facilities [34]. The PNNL experimental setup consists of a computer controlled cylinder and piston, that is capable of creating a variety of pressure regimes. Through a computer-controlled gas pressurization system attached to the pneumatic cylinders, the positions of the hydraulic cylinders were moved to either pressurize or depressurize the

chamber.

In the PNNL experiment, both fish species were acclimated for 16-22 hours at either 101[kPa] or 191[kPa] of pressure before exposure to a scenario of changing ambient pressure simulating passage through a hydropower dam turbine. The pressure is simulated via a gradual pressure increase to about 200[kPa] of pressure, followed by a sudden decrease in pressure to about 70[kPa] (test 1) or 100[kPa] (test 2) in about 0.4[sec], followed by gradual return to 101[kPa]. Following the exposure, fish were held at surface pressure for a 48-hours post exposure observation period.

Results of PNNL experiment showed that no fall chinook salmon died during or after exposure to the pressure fluctuation, and no injuries were observed during the 48 hour post-exposure observation period. For bluegill sunfish exposed to the pressure fluctuation, only one fish died and injuries were less severe and less common than for bluegills subjected to higher pressure differences in two other experiments [28], [29].

Table 5.1 shows a summary of the initial height of each injection, pressure difference, the time interval that each particle is being exposed to it and the ratio of pressure difference to the time interval from numerical simulation. Table 5.2 shows the same variables from the PNNL experiments. Providing a data summary similar to what is showed in table 5.1 from numerical simulation of particles pressure history would provide the opportunity of an accurate comparisons against experimental thresholds. For our study, comparing the numerical results showed in table 5.1 against the experimental PNNL data from table 5.2 shows that the values of $\frac{\Delta P}{\Delta t}$ experienced by the particles (highlighted in green) are of the same order of magnitude as the fish in the experiments. The exact value is smaller, but that is only representative of the specific conditions chosen for this test (turbine power, depth, TSR, blade design, ...). The value of ΔP simulated is also similar to the one measured for hydropower dam turbines. These preliminary results indicate that this issue, the pressure fluctu-

ations imparted by MHK turbines on small marine organisms as they flow through the turbines, could be considerable and therefore should be studied in future turbine development. This methodology can be applied to numerical simulations that are done as part of the performance analysis and wake interactions studies, with very little overhead. It promises to shed light into the potential effects and guide the environmental optimization and monitoring.

Table 5.1: Sudden pressure fluctuation value and its duration experienced by simulated particles.

$Z_{initial}$	$\Delta t[sec]$	$\Delta P[kPa]$	$\frac{\Delta P}{\Delta t}[\frac{kPa}{sec}]$
12.80	0.13	12.74	98.00
13.40	0.18	12.33	68.50
14.00	0.20	10.96	54.80
14.50	0.18	10.06	56.00

Table 5.2: Sudden pressure fluctuation value and its duration experienced from PPNL data.

Test #	$\Delta t[sec]$	$\Delta P[kPa]$	$\frac{\Delta P}{\Delta t}[\frac{kPa}{sec}]$
1	0.40	131.70	329.25
2	0.40	111.40	278.50

5.2.4 Conclusions

In conclusion, although the magnitude of the hydrostatic pressure fluctuations experienced by particles along the channel is larger than the change in static pressure due to the flow acceleration, it occurs over a large time interval and therefore will give fish enough time to adjust to the perturbation.

The region where the maximum pressure fluctuation happens is the leading edge of the blade tip. Tip vortices are formed there and the pressure in that region of the suction side is very low. Based on the results from our simulation and comparing them with experimental results from PNNL, it has been shown that the ratio of this pressure fluctuation over its time interval is comparable than the minimum thresholds set by PNNL. However, beside the magnitude of the sudden pressure fluctuations, other criteria such as gas supersaturation level and the depth from where the fish are being entrained from may play an important role in the study of the effect of pressure fluctuations on marine species. Considering these criteria in our modeling is beyond the scope of this work at this stage.

5.3 Modeling the Effect of MHK Turbine on Sedimentation of Suspended Particles in the Flow

The potential effects of the turbulent wake behind a hydrokinetic turbine resulting in enhancement or reduction of the sedimentation process of suspended particles in the flow and their effects on the environment has been briefly addressed before in this chapter. In this section, the procedure and assumptions for finding the best approach and model for simulating the particles motion in the flow, the details of the model's theory and the governing equations will be explained. Finally the results from these simulations will be presented and analyzed.

Numerical Modeling Theory

Based on the governing equations of DPM explained in subsection 5.2.1, the mean velocity component of fluid phase is being considered for modeling the trajectory of the particles. However, from our previous simulations, we have already modeled flow in the channel as highly turbulent. To be consistent, the effect of the fluctuating component of the velocity needs to be considered in modeling the effect of the turbulent wake on sedimentation of suspended particles in the flow. In order to take the effect of the fluctuating velocity into account, stochastic tracking, also referred to as Discrete Random Walk (DRW) model, should be used.

Discrete Random Walk model, predicts the turbulent dispersion of particles by integrating the trajectory equations for individual particles, using the instantaneous fluid velocity $\bar{u} + u'(t)$, along the particle path during the integration. In this formulation, the fluctuating velocity components are discrete piecewise constant functions of time. Their random value is kept constant over an interval of time given by the characteristic life time of the eddies. By computing the trajectory in this manner for a sufficient number of representative particles, the random effects of turbulence on

particle dispersion can be incorporated in the model.

Velocity fluctuation components that prevail during the lifetime of the turbulent eddy are defined as follows:

$$u' = \zeta\sqrt{\overline{u'^2}} \tag{5.8}$$

$$v' = \zeta\sqrt{\overline{v'^2}} \tag{5.9}$$

$$w' = \zeta\sqrt{\overline{w'^2}} \tag{5.10}$$

where it is assumed that the fluctuating velocity components obey a Gaussian probability distribution. ζ is a zero mean, unit variance, normally distributed, random number and the other terms on the right hand side of the above equations are the local RMS value of the velocity fluctuations. Assuming that the turbulence flow is isotropic and knowing the kinetic energy of turbulence at each point in the flow, RMS values can either evaluated directly when the Reynolds Stress turbulence model is used or can be defined as follows for $k-\omega$ turbulence model:

$$\sqrt{\overline{u'^2}} = \sqrt{\overline{v'^2}} = \sqrt{\overline{w'^2}} = \sqrt{2k/3} \tag{5.11}$$

in this formulation the characteristic life time of the eddy is defined as:

$$\tau_e = 2T_L \tag{5.12}$$

where T_L for small tracer particles is called the fluid Lagrangian integral time and is approximated as:

$$T_L \approx 0.15\frac{k}{\epsilon} \approx 0.15\frac{1}{\omega} \tag{5.13}$$

Another time scale in this model is the particle eddy crossing time defined as follow:

$$t_{cross} = -\tau ln[1 - (\frac{L_e}{\tau|u - u_p|})] \tag{5.14}$$

where τ is the particle relaxation time, L_e is the eddy length scale, and $|u - u_p|$ is the magnitude of the relative velocity. The particle is assumed to interact with the

fluid phase eddy over the minimum of the eddy life time and the eddy crossing time. Whenever this time is reached, a new value of the fluctuating velocity is calculated by applying a new value to ζ.

5.3.1 Assumptions

At this stage, the goal is to study the effect of the turbulent wake generated by an MHK turbine on the sedimentation process of suspended particles in a tidal channel. Since the sedimentation is not an instantaneous effect, but rather it depends on the average effect of the velocity deficit on the particle trajectories, VBM is a good candidate for this study. Furthermore, based on our previous results, VBM simulates the majority of the turbulent wake, excluding the closest area one to two radii away from the turbine, with a very good level of approximation. It is much less expensive than the SRF model from a computational point of view and can thus be used with much larger domains where the cumulative effect of multiple turbines can be studied. It does not have any restrictions on applying different boundary conditions (modeling the channel bottom effect) in the domain. Therefore, it is used to model the particles sedimentation process.

The suspended particles are considered to have spherical shape. They are being injected from a 20 by 20 injection grid located at the inlet of the channel. This injection plane dimensions are such that it covers a turbine area and a small lateral region in its surroundings. In order to capture the effect of the turbulent flow, DRW model is set to use a number of tries equal to 10, meaning that each initial position of a particle is tested 10 times, and in each test the fluctuating component of the velocity is evaluated based on random fluctuations, see equation 5.8 . This will provide the basis for statistical analysis of the results.

The material of the sediment particles is modeled as slightly denser than water, such

that they settle under the effect of gravity. Their density ratio with respect to water is set to 1.2 and 2.5. As for the size of particles, different diameters such as 100[μm], 1[mm], 5[mm], 1[cm] and 5[cm] are used in order to cover a wide range of particle sizes.

Injected particles travel along the channel and interact with the velocity deficit in the turbulent wake and the accelerated flow around the turbine. The decelerated and accelerated flow affect the particle paths and the sedimentation process. The location of sedimented particles at the bottom of channel and the number of particles that made it to the outlet of the channel are investigated and compared with particles in the same channel but without turbines in it. This comparison will reveal the potential impact of MHK turbines environmental effects.

5.3.2 Results

Figures in this sub-section show a top view of the bottom of the tidal channel. In these figures, x and y-axis show the length and width of the channel respectively and the center of the turbine disk is located at (0,0). Different color symbols show the sedimented particles on bands along the bottom of the channel. For comparison purposes, the region downstream of the device was divided into 50 [m] bands along the channel and particles sedimented on each band are shown with different color. Legend in the figures show the percentage of sedimented particles on each band. The title of the figure give the details of injection grid size and location, applied numerical scheme, number of tries, particle properties (i.e diameter and density ratio) and the percentage of the particles that reached the outlet of the channel.

5.3.3 Sedimentation process of particles with 5[cm] and 1[cm] diameter.

Preliminary results show that particles with 5[cm] diameter behave as very heavy particles, with their paths deviating minimally from ballistic trajectories. Their sedimentation process starts under effect of gravity right after being injected at the inlet of tidal channel and they mostly settle on the first band, without being affected by the turbulent wake of the MHK turbine. Therefore their sedimentation process does not show any significant influence from the turbines.

Reducing the particle size from 5[cm] to 1[cm] lowers the Stokes number by a factor of 25, and produced a set of different results. Although these particles are still large and sediment faster than particles with smaller sizes (i.e. 1[mm] and 100 [μm]), the velocity fluctuations in the turbulent wake of the device affect their motion significantly. Figure 5.8(a) shows the 1[cm] particles sedimented on the bottom of the tidal channel after interaction with the turbulent wake of the MHK turbine. Figure 5.8(b) shows the same phenomena in a tidal channel without turbine effect. Since these injected particles are large and heavy, all of them sediment on the bottom of the channel and don't make it to the outlet. Comparing percentages of the sedimented particles between these two figures, it can be seen that the sedimentation process was enhanced by 1.33% and 0.55% on first and second bands downstream of the MHK turbine (light blue and yellow) respectively compare to the corresponding bands in a channel without the turbine effect.

The U-shape on the last band in figure 5.8(a) shows the effect of the inhomogeneous flow in the turbine wake. Decelerated streamwise flow downstream slows down the particle motion. Besides that, the centrifuging of the particles due to the blade rotation exposes the particles to the flow in the periphery of the turbine, which is slightly accelerated by the reduction in cross sectional area induced by the turbine. Particles sediment faster in the core of the wake, which gets depleted as the distance from the

turbine increases. The particles in the periphery travel further and sediment along the edges of the wake, giving rise to the U-shape sediment pattern. The cumulative effect of multiple turbines may lead to changes in the benthic ecosystem associated to this process.

The reason behind the sedimentation enhancement is due to the velocity deficit in the turbulent wake. The introduced velocity deficit reduce the streamwise velocity of the particle and the terminal velocity component becomes dominant. This results in a faster sedimentation in compare to the case of a turbine without turbine effect where the streamwise velocity is constant along the channel. It should be noted that turbulent velocity fluctuations might either enhance or reduce the sedimentation process, especially in the case of small size particles, where the effect of gravity is not as strong as it is in case of large and heavier particles, which will be discussed in more details in the results for smaller size particles. The enhancement of sedimentation process due to turbulent wake of the device is in agreement with the previous studies about the effect of turbulent flows on heavy particles[36].

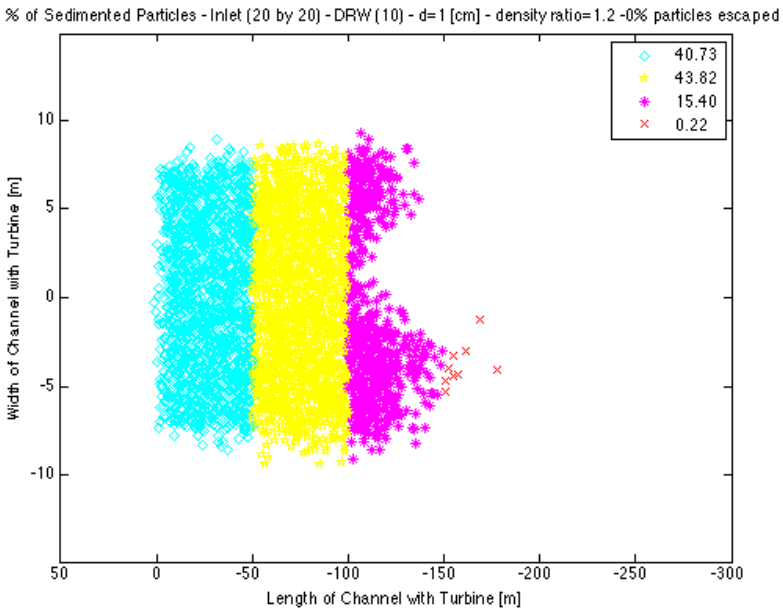

(a)

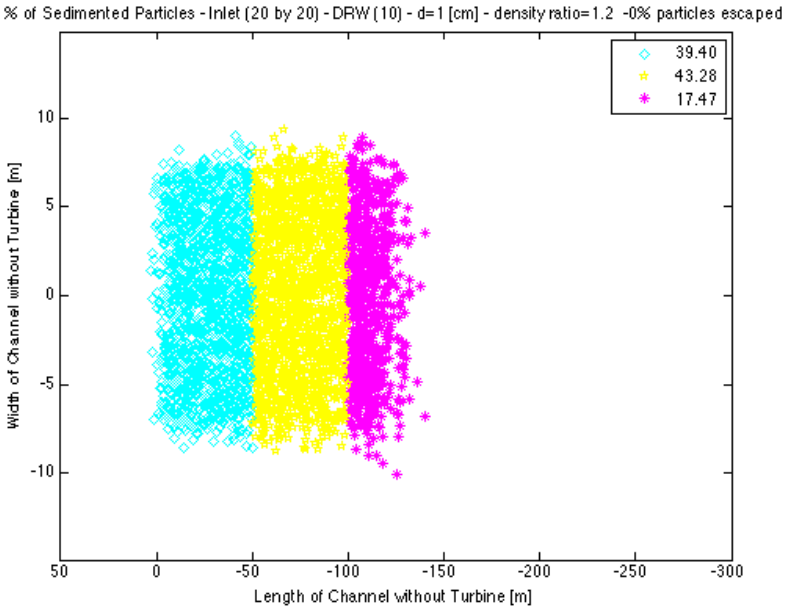

(b)

Figure 5.8: Top view of the tidal channel with turbine (a) and without turbine (b).

5.3.4 Sedimentation process of 5[mm] diameter particles.

Figures 5.9(a) and 5.9(b) show the sedimentation process of 5[mm] particles injected at the inlet on the bottom of tidal channels with and without turbines respectively. Comparison between these two results show that the sedimentation process is very similar on the first band, but is enhanced by 0.3% and 1.63% on the second and third bands downstream of the turbine respectively.

As it is seen for smaller particles (with smaller Stokes numbers), particles will travel longer distances along the channel with the streamwise flow. Therefore, the percentage of sedimented 5[mm] particles on the first band (i.e. 9.62%) is significantly less than the corresponding percentage for 1[cm] particles (i.e. 40.73%). Since, the 5[mm] particles will be dragged by the streamwise flow further along the channel, the sedimentation enhancement becomes noticeable on the third band instead of on the first band just right after the turbine. As long as the particle sedimentation was enhanced near the turbine, the percentage of sedimented particles further downstream is diminished with about 5%, but again enhanced with about 1% on the sixth band due to the centrifugal effect. The U-shape pattern of sedimentation due to the MHK turbine is observed nearly at the end of the channel (i.e. 5th and 6th bands) for this case.

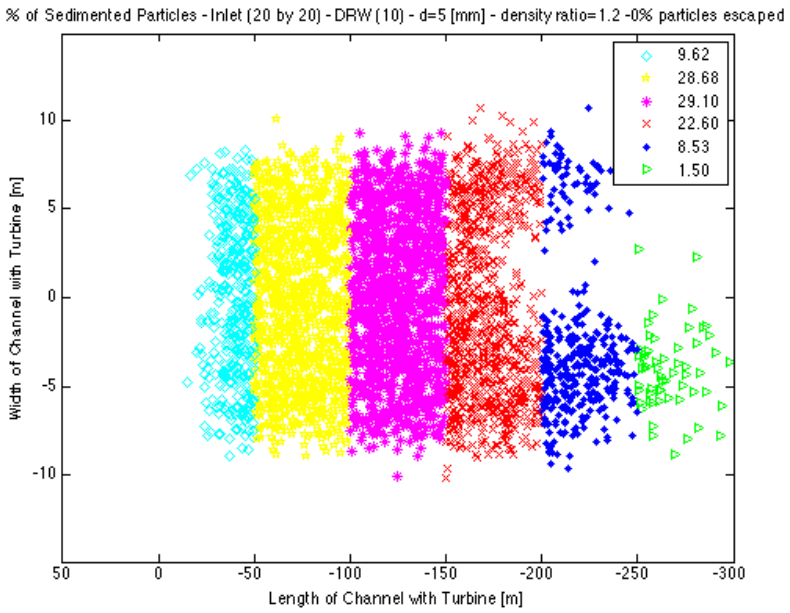

(a)

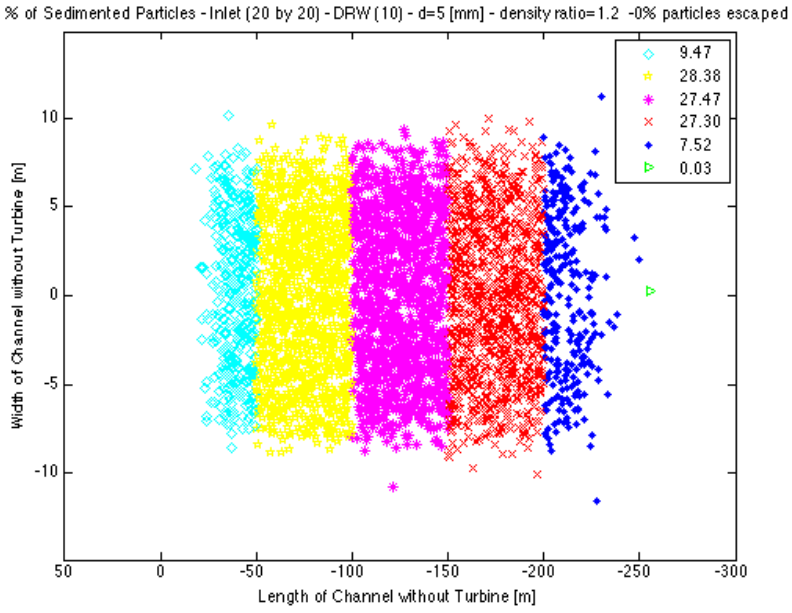

(b)

Figure 5.9: Top view of the tidal channel with turbine (a) and without turbine (b) with 1% turbulent intensity at the inlet.

As it was mentioned earlier, decreasing the size and therefore mass of the particles, makes them more sensitive to the effect of turbulent fluctuations. Since the first set of simulations was done with 1% turbulent intensity at the inlet of the channel, in order to have more realistic boundary conditions for a tidal channel as discussed in chapter 3 (subsection 3.4.4) and also being able to study the effect of turbulent fluctuation on particle sedimentation, the value of turbulent intensity was increased to 10% at the inlet.

Figures 5.10(a) and 5.10(b) show the sedimentation process of 5[mm] particles on the bottom of the tidal channels with and without turbine for the increased value of turbulent intensity. As it is observed in the results, increasing the turbulent intensity value enhances the mixing process in the turbulent wake. Particle sedimentation spreads along the width of the channel and the centrifugal effect due to the blade rotation is not observable anymore. The settling process in this case was enhanced on the first three bands downstream of the MHK turbine by 0.47%, 0.72% and 0.18% respectively (light blue, yellow and pink). Furthermore comparing the channel with values of 1% and 10% turbulent intensities at the inlet, the sedimentation process in a channel with higher turbulent intensity is increased by more than 4% in the first 50[m] downstream of the turbine where the maximum turbulent fluctuations occur. Observation of this phenomena again confirm the sedimentation enhancement due to the strong turbulent fluctuation.

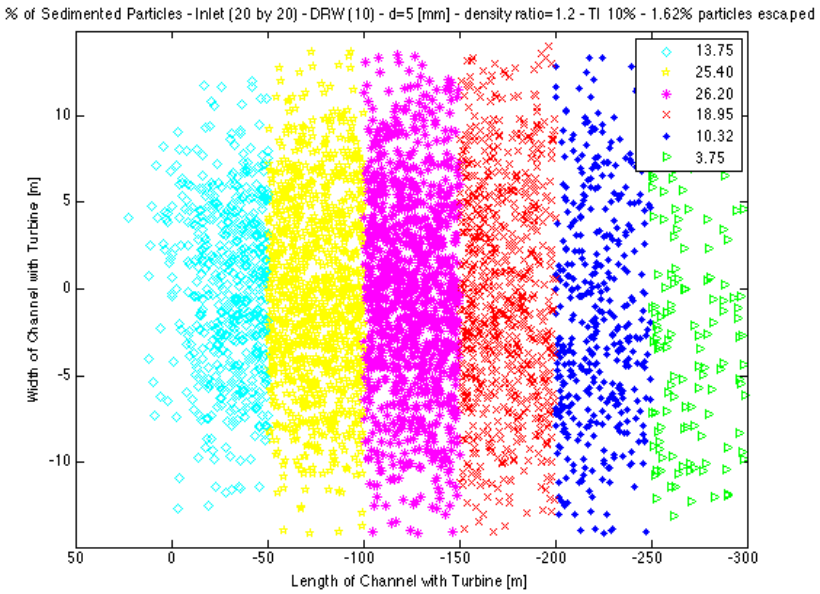

(a)

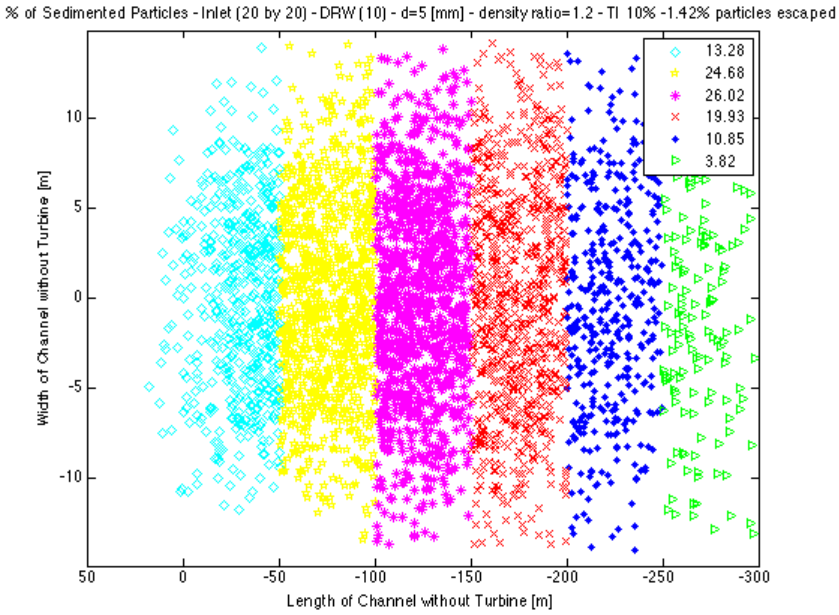

(b)

Figure 5.10: Top view of the tidal channel with turbine (a) and without turbine (b) with 10% turbulent intensity.

5.3.5 Sedimentation process of particles with 1[mm] diameter.

Results from numerical simulations show that for 1[mm] particles the sedimentation process is slow and the particles have tend to follow the flow in the wake of the turbine. Therefore, the effect of turbulent fluctuations become the dominant effect in their sedimentation process. Due to lower Stokes number, particles are carried with the streamwise flow and cross the fluid trajectories less than larger particles. Therefore, just a few number of the injected particles settle on the channel's bottom. Since the effective sedimentation of 1[mm], as well as 100 [μm], particles on the bottom of tidal channel is not significant for the length simulated, the particles spatial distribution at the outlet of the channel with and without turbine effect is studied in order to study the effect of turbulent wake of the MHK turbine on sedimentation process of these particles.

Figure 5.11(b) shows the percentage of 1[mm] particle distribution on the outlet of the channel without turbine. As it can be seen, 96% of the particles injected from a 7[m] by 7[m] grid at the inlet were dragged by the streamwise flow to the outlet while they moved vertically towards the bottom of the channel under the effect of gravity. Figure 5.11(a) shows the same result for the channel with a turbine in it. Comparison between these two results show that the rotation of the turbine and its turbulent wake enhanced in some cases, and reduced in others, the sedimentation process of the 1[mm] particles. In figure 5.11(a) it can be seen that the percentage of resuspended particle on the first two top bands (pink and yellow) were increased by 5.52% in the channel with turbine effect. Similarly an increase of 5.42% of the particles is observed on the bottom band at the outlet (green). As a result of the upward and downward push of the particles under the effect of rotation and turbulent fluctuations, the percentage of particles in the intermediate (red and blue) bands decreases on the channel with a turbine.

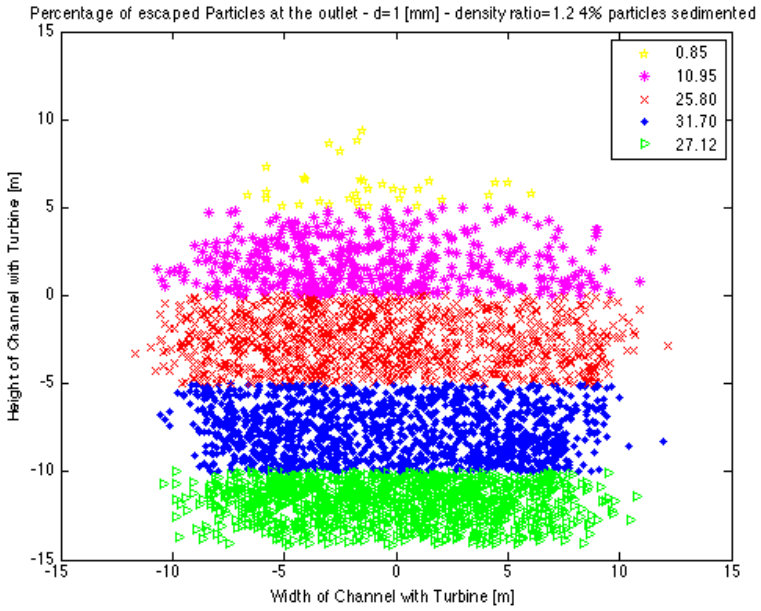

(a)

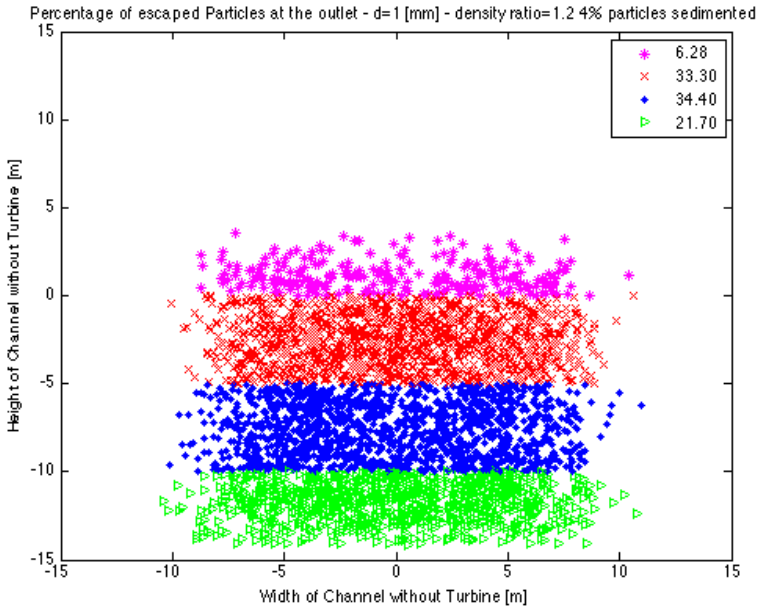

(b)

Figure 5.11: 1 [mm] particle distribution at the outlet of tidal channel with turbine (a) and without turbine (b).

Increasing the turbulent intensity at the inlet of the channel resulted in more homogeneous particle diffusion in the flow. However, the effect of the turbine wake on the particles by the turbulent fluctuations was observed. Figures 5.12(a) and 5.12(b) show the 1[mm] particle distribution at the outlet of the channel with and without turbine respectively. 1.5% of the injected particles were resuspended to the top two bands (yellow and light blue) but the percentage of the particles at the two bottom bands (blue and green) were decreased by about 2% in the channel with a turbine. This is explained by the percentage of the sedimented particles on the bottom of the channel. As it is stated at the top of the figures 5.12(a) and 5.12(b), the percentage of sedimented particles in channel with turbine effect were increased by 2%. This shows that the resultant turbulent effect in this case was strong enough that it enhanced the sedimentation on the bottom of the channel.

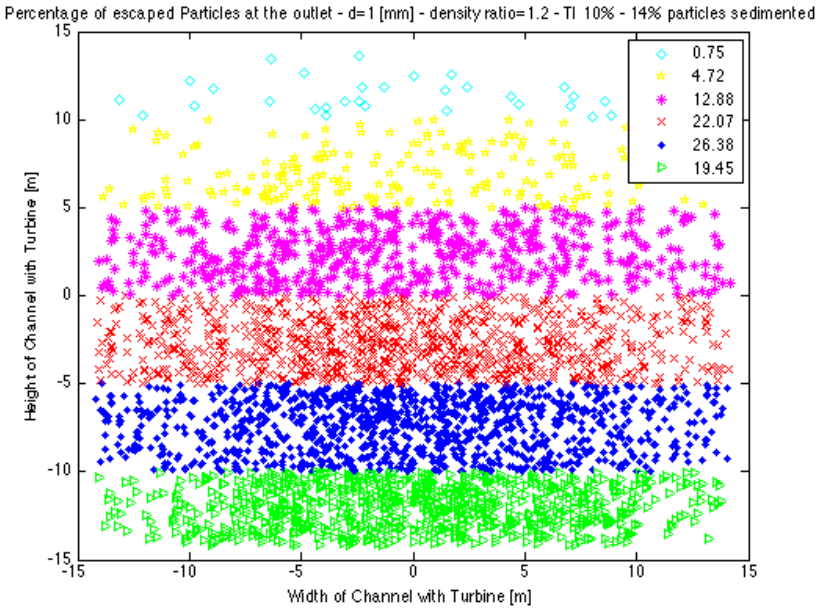

(a)

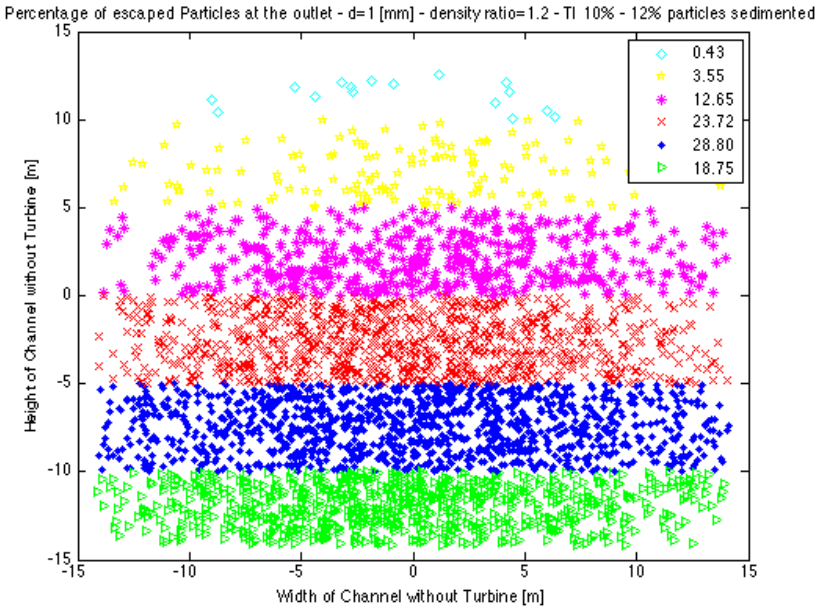

(b)

Figure 5.12: 1 [mm] particle distribution at the outlet of tidal channel with turbine (a) and without turbine (b) with increased turbulent intensity at the inlet.

5.3.6 Sedimentation process of particles with 100[μm] *diameter.*

The calculated Stokes number for 100 [μm] particles in the tidal channel flow is in order of 0.01, and the crossing trajectories effect due to gravity is negligible. Therefore, similarly to 1[mm] particles they will be dragged by the streamwise flow along the channel and the effect of gravity on them will be difficult to assess. Figure 5.13(b) shows the distribution of 100[μm] at the outlet of tidal channel without turbine effect. As it is shown in this figure, particles were minimally affected by gravity while traveling along the channel from the inlet to the outlet. They are still in a grid very similar to the 7[m] by 7[m] injection grid at the inlet and their percentage distribution is the same. Now comparing figure 5.13(b) with figure 5.13(a), which shows particle distribution on the outlet of a channel with a turbine, it is observed that 5.69% of the particle were pushed up due to the turbulence fluctuations from turbine rotating blades (yellow band on top) and 4.6% of them were being pushed downward (blue band on bottom).

Increasing the turbulent intensity at the channel inlet to 10% resulted in a wider particle distribution at the outlet. Figure 5.14(a) and 5.14(b) compares particles distribution on outlet of channel with and without turbine respectively. Figure 5.14(a) shows a 2.85% particle increase at the two top bands (yellow and light blue) and also 1.51% increase in two lower bands (blue and green). This captures the effect of rotating turbine blades. However, increasing the turbulent intensity to 10% at the inlet made this distribution smoother.

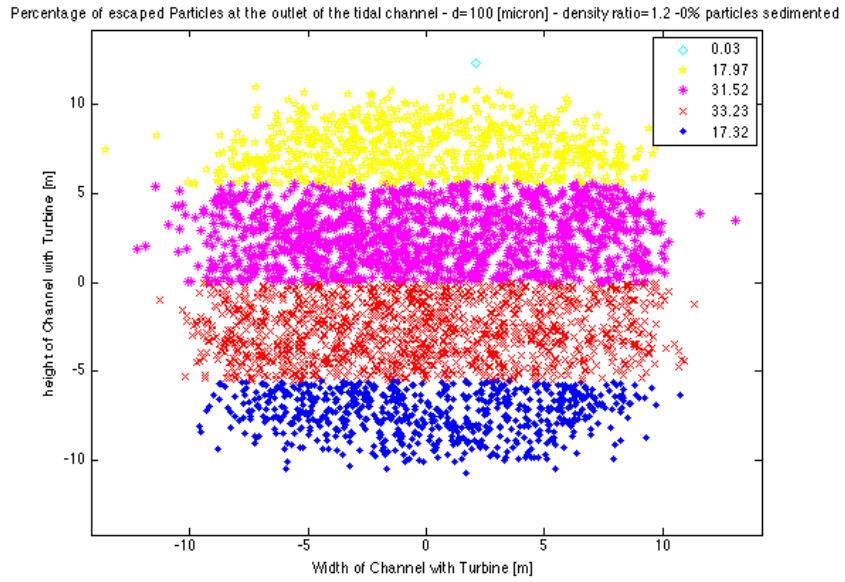

(a)

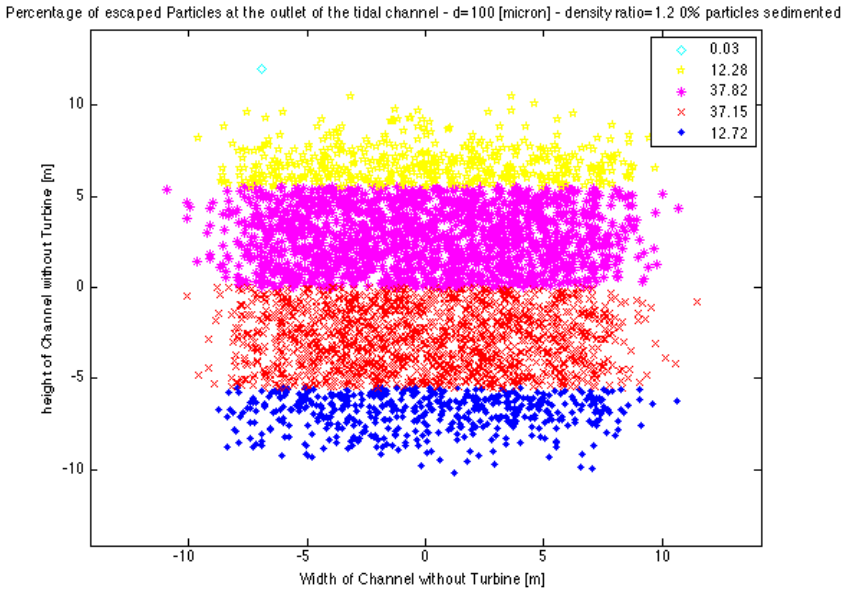

(b)

Figure 5.13: 100 [μm] particle distribution at the outlet of tidal channel with turbine (a) and without turbine (b).

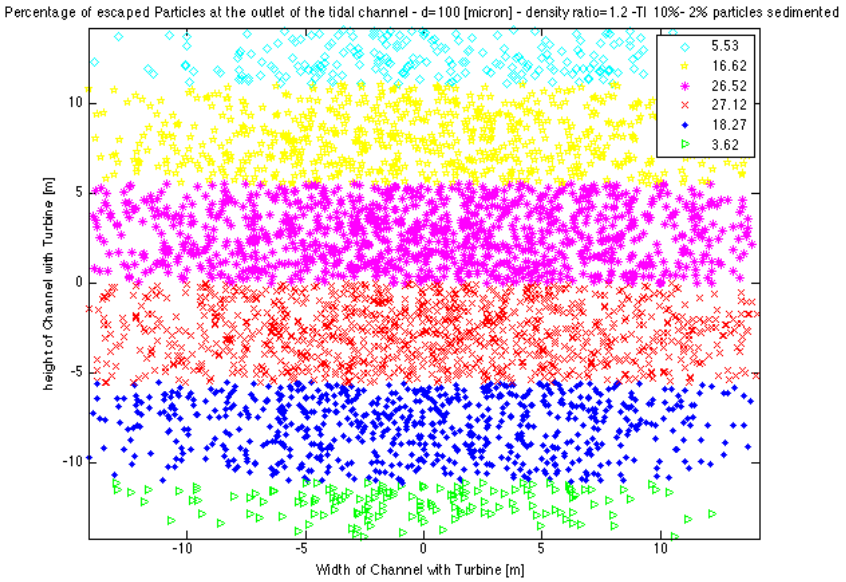

(a)

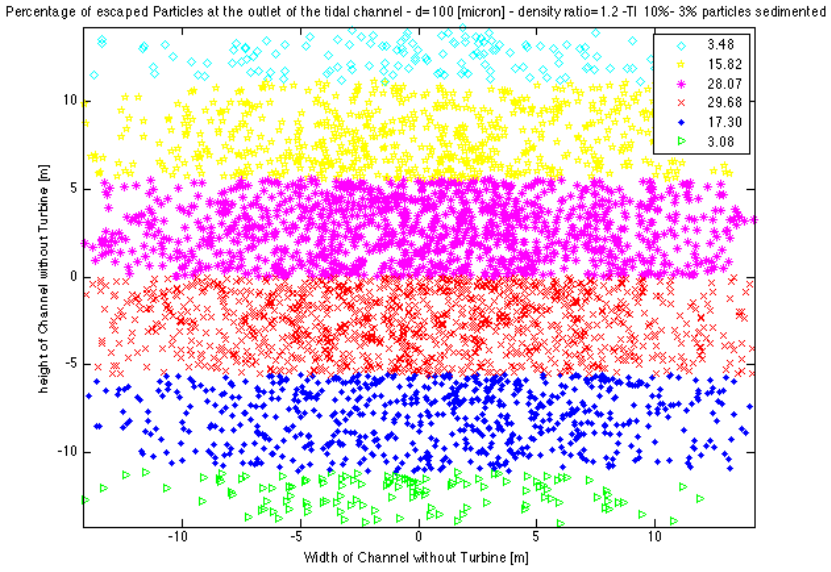

(b)

Figure 5.14: 100 [μm] particle distribution at the outlet of tidal channel with turbine (a) and without turbine (b) with increased turbulent intensity to 10% at the inlet.

5.3.7 Conclusions

For the larger size particles (i.e. 1 [cm] and 5 [mm]), the sedimentation process follows almost ballistic trajectories. However, it has been observed that the velocity fluctuation in the turbulent wake of the MHK turbine and also the increased value of turbulent intensity at the inlet of the channel enhances the sedimentation process of these particles. As shown in figure 5.15(a), which visualizes the percentage of sedimented particles on each of the six 50[m] bands along the channel, a slight sedimentation enhancement was observed at the first band right after the turbine blade for 1 [cm] particles and more significantly on the third band for 5 [mm] particles, as the effect of turbulence and the momentum deficit in the wake increases as the size of the particles decrease. Particles were dragged further along with the streamwise flow along the channel as their terminal velocity decreased. For these two particle sizes, the effect of rotation was seen in the results (in the form of a U-shape sedimentation pattern) with idealized boundary conditions, when the turbulent intensity at the inlet of the channel was set to 1% (figures 5.8(a) and 5.9(a)). Increasing the value of the turbulent intensity at the inlet of the channel resulted in a more homogeneous and broader sedimentation process along the the tidal channel. As figure 5.15(b) shows, this modification minimizes the differences between the tidal channel with and without turbine, since the particles are fairly large and therefore the gravitational effect plays a dominant role compared to the turbulent fluctuations.

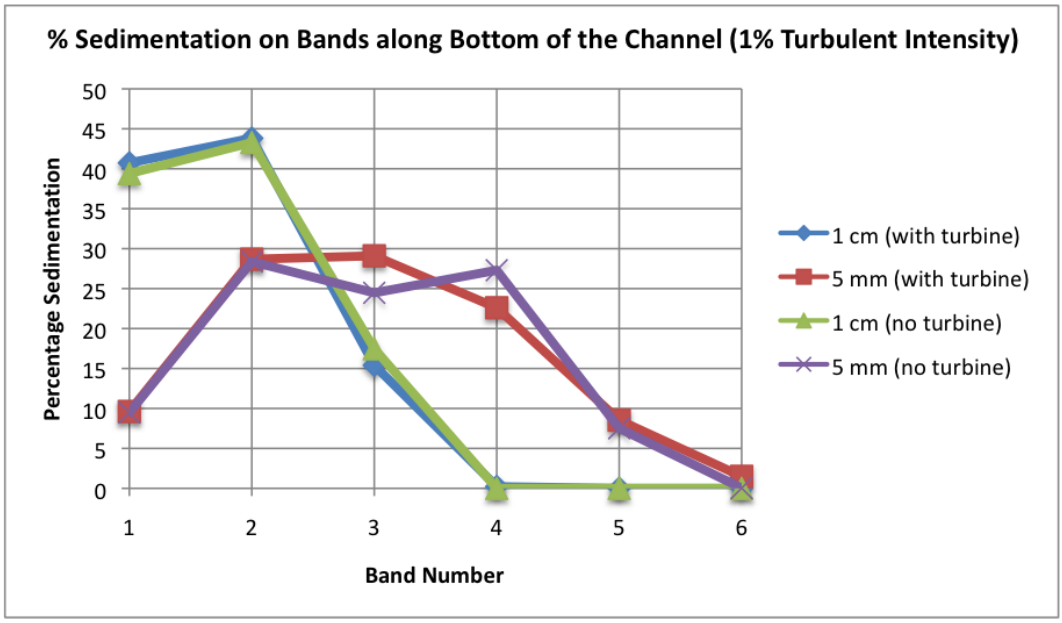

(a)

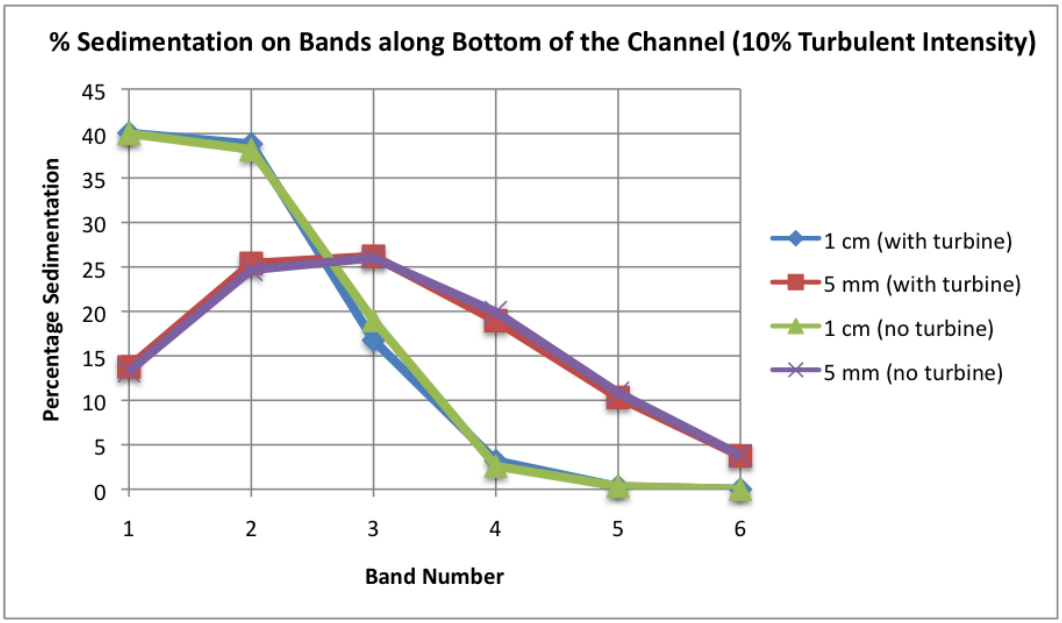

(b)

Figure 5.15: Sedimentation percentage of 1 [cm] and 5[mm] particles on the tidal channel bottom with turbulent intensity of 1% (a) and 10% (b) at the inlet.

For smaller particles (i.e. 1 [mm] and 100 [μm]) the gravitational effect decreased with the size of particles and therefore the turbulence fluctuation became the dominant term for the study of the sedimentation process. Figure 5.16(a) shows the percentage of particles distributed on the six 5 [m] bands along the height of the outlet. As it is shown in this figure, 1[mm] particles end up on the 2nd and 3rd bands, where the balance of terminal velocity and turbulent fluctuations drive most of the trajectories. The rotation of the flow induced by the blade motion pushed some particles up and down and therefore a higher percentage of particles on 1st and 4th bands are observed in comparison with the channel without turbine. Similar phenomena can be seen in the results for the 100 [μm] particles. For this particle size, the balance of gravity and turbulent fluctuations led most particles to the 3rd and 4th bands, and the centrifuging due to the rotation of the blades, pushed particles to the 2nd and 5th bands on the outlet.

Increasing the value of the turbulent intensity at the inlet of the channel to 10% had an effect similar to that for the larger particles. The area covered by the small particles became wider and more homogeneous at the outlet of the channel. As it is shown in figure 5.16(b), the particles were more uniformly distributed across the outlet section of the channel, and the differences observed above for the different particle sizes on different bands are erased by the increased turbulent diffusion associated with the higher turbulent kinetic energy in the free stream flow. The effect of the turbine wake on small size particles presented a symmetric behavior, with the rotation of the blade inducing an upward motion for about half the particles and a downward motion in the other half.

Previous studies of sedimentation of small particles (i.e. in the order of mm and [μm] sizes) in a turbulent flow, show that the Discrete Random Walk (DRW) model (and its use of equation 5.13 to calculate the interaction between the particles and the

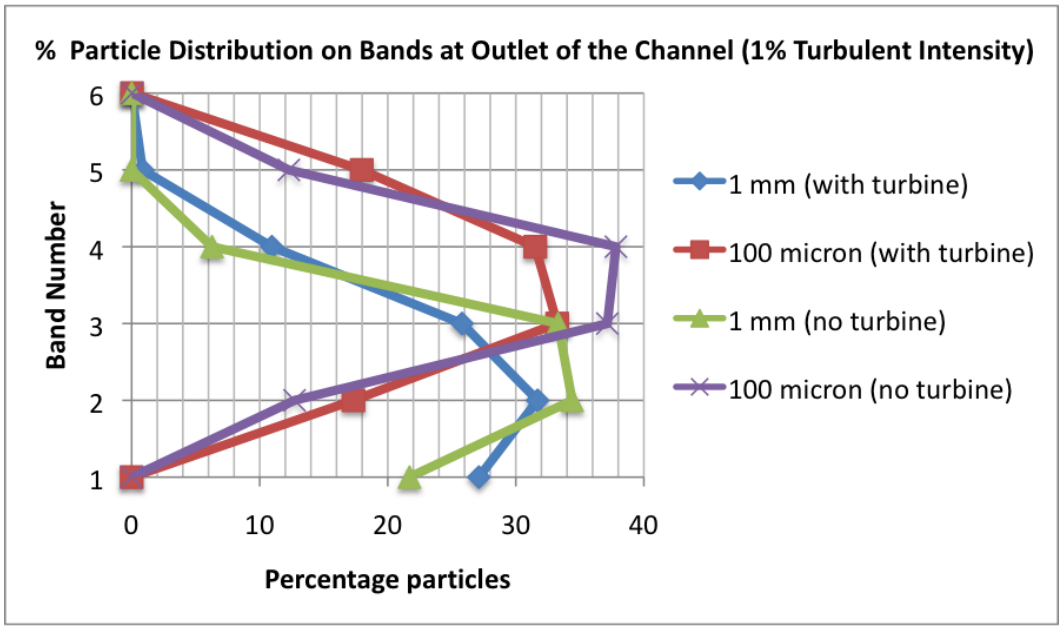

(a)

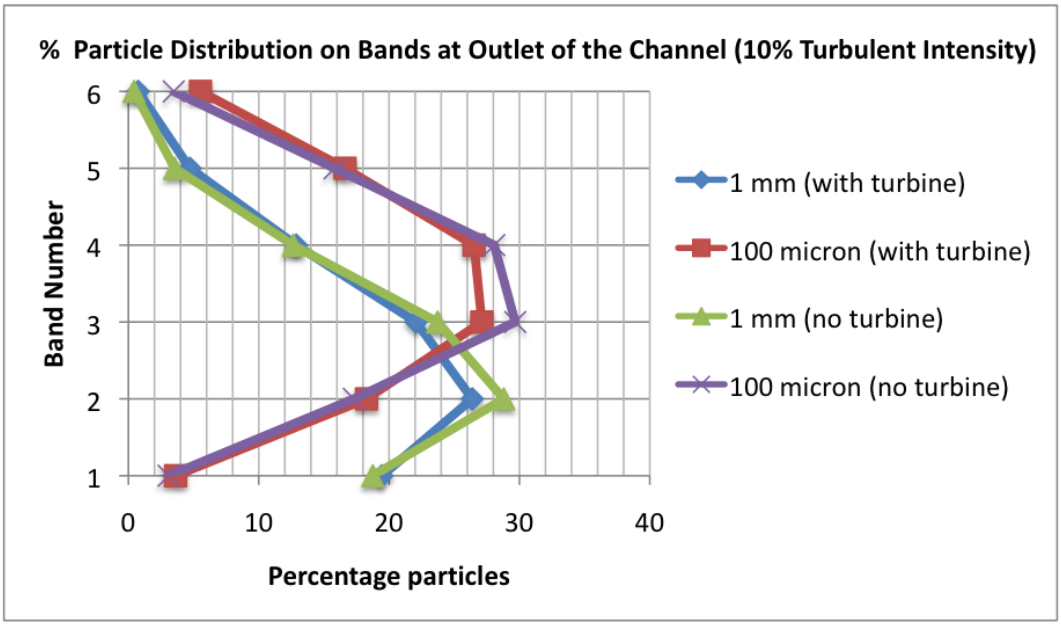

(b)

Figure 5.16: Distribution percentage of 1 [mm] and 100[μm] particles on the tidal channel outlet with turbulent intensity of 1% (a) and 10% (b) at the inlet.

eddies) leads to an overestimation of the fluctuations in the particle velocity in highly turbulent regions such as the wake of an MHK turbine [37][38]. Therefore, in order to have a more accurate calculation of the effect of turbulent fluctuations on the particle trajectories, we need to use a more detailed turbulent model such as Reynolds Stress Model (RSM). A fine mesh resolution near the bottom wall of the channel would allow us to capture the effect of the boundary layer and the potential particle resuspension, which would result in more realistic conditions and a more accurate prediction of the turbulent wake interaction with the suspended particles in a channel.

Chapter 6

SUMMARY, CONCLUSIONS AND FUTURE WORK

This section of the thesis includes a summary and conclusions for each of the previous chapters. First a summary of the work and studies that was done in the corresponding chapter is presented. Then the most important conclusions of the chapter will be highlighted and potential future work will be addressed.

6.1 Summary for the Numerical Methodology Development

In chapter 2 the theory for three different numerical models used to simulate the dynamics of flow around a horizontal axis tidal turbines (HATT): Single Rotating Reference Frame (SRF), Virtual Blade Model (VBM) and Actuator Disk Model (ADM) were explained.

Single Reference Frame (SRF) model introduced to be an accurate numerical scheme for flow simulation in a moving reference frame, such as the flow field around and in the wake of a wind or tidal turbine. In this model the actual geometry of the turbine blades should be created and meshed and rotation of the blades would be modeled via prescribed periodic boundary conditions in the computational domain. The main idea behind this model was to render the unsteady problem in a stationary frame, steady with respect to the moving reference frame. However, this change of reference frames required the addition of two extra acceleration terms, Coriolis and Centripetal acceleration, in the momentum equations, that has been derived and discussed in details in section 2.1.2.

Virtual Blade Model (VBM) was the second model in our methodology. This model was an implementation of the Blade Element Method (BEM) within ANSYS FLUENT. VBM models the time-averaged aerodynamic effects of the rotating blades, without the need for creating and meshing their actual geometry. VBM simulated the blade aerodynamic effects using momentum source terms placed inside a rotor disk fluid zone that depends on the chord length, angle of attack, and lift and drag coefficients for different sections along the turbine blade. Detail of the governing equations and iteration process of VBM discussed in details in section 2.2.2

Actuator Disk Model (ADM) was the ANSYS FLUENT implementation of Actuator Disk Theory. In this model we matched the coefficients of the governing equations from the actuator disk theory with the governing equations for modeling a porous media in ANSYS FLUENT. In ADM the aerodynamic effect of rotating blades was represented by a pressure discontinuity over an infinitely thin disk with an area equal to the swept area of the rotor. The details of this representation and governing equations can be found in section 2.3.2

In conclusion, based on the theory and physics behind each of these three models, SRF was known as the most accurate and computational intensive model for flow field simulation around and in the near wake region of the rotating blades. VBM was known as an intermediate computational cost model, that models the wake as an axisymmetric one right after the blade. ADM is one step simpler than VBM, since it modeled the effect of the blades as a thin porous disk. In order to confirm these conclusions and also have a better understanding about the capability of each model, the developed methodology was applied to model a well characterized, two bladed, horizontal axis wind turbine, NREL Phase VI, that was presented in chapter 3.

6.2 Summary for the Validation of the Developed Numerical Methodology with Modeling NREL Phase VI wind turbine

The validation process for the developed numerical methodology started by validating 2D simulation results for the airfoil section of NREL Phase VI wind turbine. The calculated 2D pressure and lift coefficients were compared against experimental and previous numerical data. After finding the best mesh structure around the blade section and be confident that the fine resolution mesh is capable of capturing the complex turbulent flow around the blade and therefore model the rest of the flow accurately, the full 3D domain was created for the SRF model. Then, we validated our results against experimental data and previous results from numerical modeling of NREL Phase VI turbine.

Observation of an axisymmetric turbulent wake a few radii downstream of the blade in SRF results, directed us toward modeling NREL Phase VI turbine using simpler numerical schemes (i.e. VBM and ADM). Therefore we created the computational domain for VBM based on NREL experiment dimensions and boundary conditions and compared the results against the SRF results. Despite the predictable differences between results from VBM versus SRF, specifically right after and around the blade, the modeled flow field and velocity deficit in the far wake region were in a very good agreement with each other. The calculated extracted power by the turbine, maximum and minimum angle of attack along the blade by VBM were also compared against SRF results and previous numerical studies and all of them were in a very good agreement with each other.

Finally, ADM has been implemented within ANSYS FLUENT, using the same computational domain as VBM and its results were compared with SRF and VBM. ADM did not show a very good agreement with SRF and VBM results after first set of simulations with low turbulent intensity in the free stream, however after increasing

the value of the turbulent intensity at the inlet of the channel from 1% to 10%), the modeled velocity deficit and flow field in the far wake from the ADM simulations were in good agreement with the corresponding results from SRF and VBM. This showed potential future usages of ADM for tidal turbine array optimization, since it requires minimum computational time in comparison to SRF and VBM.

In conclusion, in this methodology, SRF was showed to be the unique model that could capture the details of the turbulent flow at the tip of the blade (modeling the shed vortices at the tip) and in the near wake region (capturing the detail of the inhomogeneous flow right after the blade passage). VBM showed to be capable of modeling the velocity deficit in far wake region accurately, such that they were in a very good agreement with corresponding modeled velocity deficit with SRF. Because of its accuracy and less computational time required for VBM in comparison with SRF, VBM showed promising future in the study of the wake interaction between multiple turbines in a farm of devices. ADM showed to be able to model the flow field in the far wake with high turbulent intensity at the inlet, which is a more realistic condition than the wind tunnel value of 1%, and due to its minimum computational requirement and simplicity it showed potential usages for modeling huge farm of turbines. It should be noted that due to the lack of available data and studies on turbulent wake of the NREL Phase VI turbine, further validation studies on the simulated turbulent wake by each model against existing theories on characteristics of the axisymmetric wakes are in progress and is part of our future work. This further validation studies will improve the level of certainty for this numerical methodology to be applied toward modeling of wind and tidal turbines in future.

6.3 Summary for the Application of our Validated Numerical Methodology to the Study of Marine Hydrokinetic (MHK) Turbines

In chapter 4 the process of applying this methodology to an MHK turbine from the wind turbine model, within the computational domain of the validated model was explained in detail. As it was mentioned earlier, the transition of the working fluid could not be done without modification of mesh in the computational domain, since this transition resulted in change of the fundamental variables of the working fluid (i.e. density and viscosity) and therefore Reynolds number. With these fundamental changes, the physics of the boundary layer and the turbulent flow in the wake were changed too, therefore the mesh of the middle block in SRF computational domain had to be re-generated. Beside the mesh modification, the tip speed ratio (TSR) of the rotating blade was modified to avoid any potential harmful physical phenomena, such as cavitation and flow separation along the blade span.

In conclusion, the validated numerical models was successfully applied to the study of MHK turbines. The new boundary condition of MHK turbine simulations was modified to approach more realistic boundary condition. In results from MHK turbine simulations, despite some small changes that discussed in section 4.2.3 the overall results were similar to the previous one. It was also observed that the flow separation along the span of the blade and shed vortices at the blade tip were similar to the corresponding validated results from simulation of the NREL Phase VI wind turbine.

6.4 Summary for the Numerical Modeling of the Potential Environmental Effects of Marine Hydrokinetic (MHK) Turbines

In chapter 5 two potential environmental effects of MHK turbine were addressed and investigated. This study was done via a combination of the previously simulated flow field in a channel with MHK turbine and the available numerical schemes for multiphase flows simulation.

The first environmental effect studied was the sudden pressure changes on particles as they flow along the blade wall, associated with power extraction across MHK turbines. These change, when experienced by small marine species, such as juvenile fish, can lead to internal organ damage and death. This modeling was done with SRF model, that showed to be capable of capturing details of the flow field on the blades. Slightly buoyant particles were injected at the inlet of the channel and their pressure history was calculated as they swim through the rotating blades. Then, numerical results were compared against the experimental data from study of the pressure fluctuation on fish by PNNL and it was shown that for the specific conditions of this simulation (NREL Phase VI geometry, 2 $[\frac{m}{s}]$ streamwise velocity and 17 rpm angular velocity, 100 kW power extracted), the magnitude of pressure fluctuation and the time interval that particles experience this pressure spike were in the same order of magnitude as the experiments carried out to study passage through traditional hydropower turbines.

The second environmental effect was the influence of the turbulent wake and generated momentum deficit in it on sedimentation process of suspended particles in channel. For this study, VBM was used, since it offered the opportunity of modeling the bottom effect and showed capability of accurately modeling the momentum deficit in the far wake region with moderate computational time requirements. Heavy particles were injected at the inlet and their sedimentation process on the bottom of the channel was investigated. It was observed that the turbulent wake can affect the sedimentation

process of particles with different sizes in different ways.

In conclusion, it was shown that the maximum value of the pressure fluctuation occurs near the tip of the blade close to the leading edge. Therefore, that region is a potentially dangerous region for fish, since the strong pressure fluctuation over a small period of time is strong enough can it could potentially damage their internal organs. For the effect of the turbulent wake on the particle sedimentation process, it was shown that the sedimentation of large particles (d=1 [cm]) is dominated by gravity effect and they settle like heavy rocks after being injected at the inlet of the channel, without being affected significantly by the turbulent fluctuations in the wake. However, intermediate size particle (d=5 [mm]) were affected by the turbulent fluctuations in the wake and their sedimentation process was enhanced due to the momentum deficit at the turbulent wake. In this case, the effect of the turbine hub and rotation of the blade on particle settling at the end of the channel were observed too. Although small size particles (d=0.1-1 [mm]) did not settle on the first 300[m] of the channel, looking at their distribution at the outlet of the channel showed that they were significantly affected by the turbine rotation and the turbulent fluctuations in the wake. The velocity due to rotation of blades pushed half of particles to the top and the other half to the bottom of the channel from the core bands of injection. Based on previous turbulent-sedimentation interaction studies and further investigation, it was observed that the current numerical model for study of particles motion in the flow (DRW) overestimates the effect of turbulent fluctuations as it is combined with $k - \epsilon$ turbulent model. Therefore one of the future tasks would be modeling the sedimentation of particles with another turbulence model, such as Reynolds-Stress model in which the fluctuating component of the flow field will be calculated directly and is not estimated by the value of the turbulent kinetic energy and turbulent frequency.

6.5 Conclusions and Future Work

In this thesis a numerical methodology consisting of three different numerical schemes with different level of fidelity and adequacy was introduced. This methodology was used to model a well characterized two bladed wind turbine, NREL Phase VI, and it was validated against previous experimental as well as numerical studies. Details of the modeling steps for each numerical scheme were presented, so that any new proposed horizontal axis tidal turbine with different geometry specification can be modeled and studied. After a validation process, we applied the methodology to the study of a horizontal axis MHK turbine, addressing and investigating the required mesh and boundary conditions modifications. It was concluded that computationally intensive models can be used to simulate the detailed physics of the flow field in the near wake regions of a single MHK turbine with long term goal of blade design optimization for maximum power extraction from tidal currents. Simpler models that are based on well established theories (i.e. Blade Element Method and Actuator Disk Model) and average the effect of the rotating blades can be used to model and optimize device arrangements in large farms of tidal turbines.

We also addressed and investigated two potential environmental effects of MHK turbine. It was shown that the strong sudden pressure fluctuation occurring over very short periods of time as particles flow over the suction side of the blade, might reach values associated with damage to the internal organs of small marine species for certain designs and operating conditions (blade shape and diameter, tip speed ratio, free stream velocity and power extraction). The preliminary studies showed that the turbulent wake can enhance the sedimentation process of intermediate and small size suspended particles in a tidal channel and result in significant changes to benthic ecosystems during long term operation.

Development of numerical tools for the study of horizontal axis MHK turbines repre-

sents a necessary step in the engineering of these devices. From blade design and array optimization to understanding their environmental effects, it requires a cost-effective, time-sensitive method to develop this technology. Through further understanding of its efficiency and environmental effects, it is hoped that this thesis and its continuation will speed up the implementation of this renewable energy source and will open the doors on future deployment and commercialization of tidal turbines to produce electricity and decrease the use of fossil fuels.

BIBLIOGRAPHY

[1] Polagye B. and et al. Environmental effects of tidal energy development: A scientific workshop.

[2] URL http://europa.eu/rapid/pressReleasesAction.do?reference=MEMO/08/33.

[3] URL www.secstate.wa.gov/elections/initiatives/text/i937.pdf.

[4] J. Boon. *Secrets of the Tide: Tide and Tidal Current Analysis and Predictions, Storm Surges and Sea Level Trends.* Horwood, 2004.

[5] Couch S. and Bryden I. Jeffrey H. Tidal current energy: Development of a device performance protocol. In *International Conference on Clean Electrical Power (ICCEP)*, 2007.

[6] Couch S. and Bryden I. Large-scale physical response of the tidal system to energy extraction and its significance for informing environmental and ecological impact assessment. In *Oceans 2007 - Europe*, 2007.

[7] Bahaj A. and Batten W. Molland A., Chaplin J. Power and thrust measurments of marine current turbines under various hydrodynamic flow conditions in a cavitation tunnel and a towing tank. *Renewable Energy*, 32:407, 2007.

[8] Batten W. and Chaplin J. Bahaj A., Molland A. Experimentally validated numerical method for the hydrodynamic design of horizontal axis tidal turbines. *Ocean Engineering*, 34:1013, 2007.

[9] Barnsley M. and Wellicome J. Final report on the 2nd phase of developement and testing of a horizontal axis wind turbine test rig for the investigation of stall regulation aerodynamics. Technical report, 1990.

[10] Jenkins N. Burton T., Sharpe D. and Bossanyi E. *Wind Energy Handbook*. Wiley, 2000.

[11] Batten W. and Chaplin J. Bahaj A., Molland A. The prediction of the hydrodynamic performance of marine current turbines. *Renewable Energy*, 33:1085, 2008.

[12] Hirsch C. *Numerical computation of internal and external flows (Volume 1: Fundamentals of numerical discretization).* John Wiley & Sons, 1997.

[13] Z.U.A. Warsi. *Fluid Dynamics, Theoretical and Computational Approaches.* CRC Press, 1993.

[14] *ANSYS FLUENT 12.0 theory guide, Chapter 2, Flows with Rotating Reference Frames.* URL http://www.fluentusers.com/fluent/doc/ori/v121/fluent/fluent12.1/help/html/th/node27.htm.

[15] Laith Z. and Rajagopalan R. Navier-stokes calculations of rotor-airframe interaction in forward flight. *Journal of the American Helicopter Society*, 40(2):57, 1995.

[16] Voutsinas S. Sorensen N. Hansen M., Sorensen J. and Madsen H. State of the art in wind turbine aerodynamics and aeroelasticity. *Aerospace sciences*, 42(4): 285, 2006.

[17] Ruith M. Unstructured, multiplex rotor source model with thrust and moment

trimming - fluent's vbm model. In *AIAA Applied Aerodynamics Conference*, 2005.

[18] Wirogo S. and Ruith M. Virtual blade model, ugm. Presentation at 2004 summit training.

[19] Corten G. P. Heat generation by a wind turbine. In *14th IEA symposion, NREL*, 2000.

[20] *ANSYS FLUENT 12.0, User's Guide, Chapter 7, Section 7.2.3, Porous Media Condition.* URL http://www.fluentusers.com/fluent/doc/ori/v121/fluent/fluent12.1/help/html/ug/node256.htm.

[21] Hand M. and Jager D. Cotrell J. Schreck S. Larwood S. Simms D., Fingersh L. Unsteady aerodynamics experiment phase 6: Wind tunnel test configurations and available data campaigns. Technical report, National Renewable Energy Laboratory (NREL), 2001.

[22] Sorensen N. and Schreck S. Michelsen J. Navier stokes predictions of the nrel phase vi rotor in the nasa ames 80 ft * 120 ft wind tunnel. *Wind Energy*, 5:151, 2002.

[23] Sorensen N. Bertagnolio F. and Johansen J. Profile catalogue for airfoil sections based on 3d computations. Technical report, Riso National Laboratory, 2006.

[24] *ANSYS FLUENT 12.0 theory guide, Chapter 4, Section 4.12, Near-Wall Treatments for Wall-Bounded Turbulent Flows.* URL http://www.fluentusers.com/fluent/doc/ori/v121/fluent/fluent12.1/help/html/th/node98.htm.

[25] Gooch S. Siting methodologies for tidal in-stream energy conversion (tisec) systems. Master's thesis, University of Washington, 2009.

[26] Polagye B. unpublished data from field measurments by National Northwest Marine Renewable Energy Center (NNMREC) at University of Washington.

[27] Elghobashi S. Particle-laden turbulent flows: direct simulation abd closure model. *Applied Scientific Research*, 48:301–314, 1991.

[28] Abernethy, Amidan B. G., and Cada G. F. Laboratory studies of the effects of pressure and dissolved gas supersaturation on turbine-passed fish. Technical report, Pacific Northwest National Laboratory, 2001.

[29] Abernethy, Amidan B. G., and Cada G. F. Simulated passage through a modified kaplan pressure regime: A supplement to "laboratory studies of the effects of pressure and dissolved gas supersaturation on turbine-passed fish". Technical report, Pacific Northwest National Laboratory, 2002.

[30] Sylvain Antheaume. Modeling a wind turbine comparisons of the srf and vbm models.

[31] R.E. Arndt. Cavitation in vortical flows. *Annu. Rev. Fluid Mech.*, 34-143:74, 2002.

[32] Stephen B. Pope. *Turbulent Flows, Chapter 7, section 7.1.3.* Cambridge University Press, 2006.

[33] Thomson J. and Durgesh V. Polagye B., Richmond M. Quantifying turbulence for tidal power applications. *MTS/IEEE Oceans 2010 conference, Seattle WA*, 2010.

[34] Abernethy C. S., Amidan B. G., and G. F. Cada. Fish passage through a simulated horizontal bulb turbine pressure regime: A supplement to "laboratory

studies of the effect of pressure and dissolved gas supersaturation on turbine-passed fish". Technical report, Pacific Northwest National Laboratory, 2003.

[35] Morsi S. and Alexander A. An investigation of particle trajectories in two-phase flow system. *Journal of Fluid Mechanics*, 55(2):193–208, 1972.

[36] Aliseda A. and Lasheras J. Cartellier A., Hainaux F. Effect of preferential concentration on the settling velocity of heavy particles in homogeneous isotropic turbulence. *Journal of Fluid Mechanics*, 468:77–105, 2002.

[37] Tian L. and Ahmadi G. Particle deposition in turbulent duct flows-comparisons of different model predictions. *Aerosol Science*, 38:377, 2006.

[38] Smith D. Shams M., Ahmadi G. Computational modeling of flow and sediment transport and deposition in meandering rivers. *Advances in Water Resources*, 25:689, 2002.